

THE QUADRATIC CORRELATION BETWEEN IN-LINE AND CROSS-FLOW,  
VORTEX-INDUCED VIBRATION OF LONG FLEXIBLE CYLINDERS

by

Jen-Yi Jong

B.S., National Cheng-Kung University  
(1978)

M.S., National Taiwan University  
(1980)

Submitted in Partial Fulfillment  
of the Requirements for the Degree of

Doctor of Philosophy

in

Ocean Engineering

at the

Massachusetts Institute of Technology  
August 1984

C Massachusetts Institute of Technology 1984

Signature of Author

Jong Jen-Yi

Department of Ocean Engineering  
August 17, 1984

Certified by

J Kim Vandiver

J. Kim Vandiver  
Thesis Supervisor

Accepted by

Chairman, Department Committee



#### ACKNOWLEDGEMENTS

I would like to express my sincere appreciation to Professor J. Kim Vandiver for his guidance and supervision during the course of my study at M.I.T., and for having been the inspiration for this investigation through his outstanding experimental skill.

I would like to thank Professors S. Ellis and M. S. Triantafyllou for their guidance and also for serving as thesis readers.

A sincere debt of gratitude is also owed to the eight member team, led by Professor J. Kim Vandiver, who participated in the field experiments. Prof. Vandiver was assisted during these experiments by Charles Mazel, Jen-Yi Jong, Ed Moas, Peter Stein, Mark Whitney, Pam Vandiver, and Jim McGlothlin. Cheng-Yuan Liou, Douglas Dummermuth, Yang-Hann Kim and Kamyab Samii, as colleagues on our research team, have each provided valuable assistance. I would also like to thank Anna Markowitz for her help during the past three years.

Thanks are extended to the American Bureau of Shipping, Amoco Production Co., Brown and Root, Inc., Chevron Oil Field Research, Conoco, Inc., Exxon Production Research, Gulf Oil Co., Mobil Research and Development Corp., Shell

Development Company, Union Oil Research, the Naval Research Laboratory, the Office of Naval Research, the Naval Civil Engineering Laboratory, and the Minerals Management Service for their sponsorship of this work.

Special thanks go to my parents for their encouragement and support through the years of my academic pursuits.

Finally, I want to thank my wife, Fuu-Chyun, for her understanding and encouragement throughout these years in school.

TABLE OF CONTENTS

|                                                                       | Page |
|-----------------------------------------------------------------------|------|
| Abstract                                                              | 2    |
| Acknowledgement                                                       | 3    |
| Table of Contents                                                     | 5    |
| List of Figures                                                       | 7    |
| Chapter 1 INTRODUCTION                                                | 10   |
| Chapter 2 THE EXPERIMENT                                              | 15   |
| 2.1 Test Site                                                         | 15   |
| 2.2 Test Cylinders                                                    | 18   |
| 2.3 Measurment System                                                 | 21   |
| Chapter 3 ANALYSIS OF EXPERIMENTAL DATA                               | 24   |
| 3.1 Vector Rotation of Acceleration<br>Time Series                    | 24   |
| 3.2 Integrator                                                        | 26   |
| 3.3 Low-Frequency Noise Expansion                                     | 33   |
| 3.4 High-Pass Filter                                                  | 35   |
| 3.5 Double Integration Procedures                                     | 41   |
| 3.6 Cylinder Motion at Lock-in and<br>Non-lock-in                     | 43   |
| 3.7 Current, Drag Coefficient and RMS<br>Displacement                 | 57   |
| Chapter 4 MODAL ANALYSIS                                              | 64   |
| 4.1 Modal Analysis of A Uniform String                                | 64   |
| 4.2 Estimation of Natural Coordinate                                  | 66   |
| 4.3 Vibration Energy                                                  | 69   |
| 4.4 Response Mode of In-line Motion                                   | 81   |
| Chapter 5 BISPECTRAL ANALYSIS OF QUADRATIC CORRELATION                | 88   |
| 5.1 Introduction to The Cumulant Spectrum                             | 88   |
| 5.2 Cross-Bicoherence Spectrum Test<br>Examples                       | 93   |
| 5.3 Quadratic Correlation Between In-Line<br>and Cross-Flow Responses | 106  |

|                                                          | page |
|----------------------------------------------------------|------|
| Chapter 6 QUADRATIC SYSTEM IDENTIFICATION AT LOCK-IN     | 121  |
| 6.1 Applications of Multiple Regression Analysis         | 122  |
| 6.2 Linear and Quadratic Response                        | 126  |
| Chapter 7 QUADRATIC SYSTEM IDENTIFICATION AT NON-LOCK-IN | 139  |
| 7.1 Least Squares Quadratic System Identification        | 139  |
| 7.2 Quadratic System Involving Square-Law Operations     | 146  |
| Chapter 8 CONCLUSIONS                                    | 160  |
| REFERENCES                                               | 163  |

# LIST OF FIGURES

| FIGURE |                                                                                                                                                                                                     | Page |
|--------|-----------------------------------------------------------------------------------------------------------------------------------------------------------------------------------------------------|------|
| 2-1    | The Experiment Site                                                                                                                                                                                 | 16   |
| 2-2    | Schematic Diagram of the Experiment Test Section                                                                                                                                                    | 17   |
| 3-1    | Relation Between Rotated Angle and DC Offset                                                                                                                                                        | 25   |
| 3-2    | Recorded Acceleration Before Rotation                                                                                                                                                               | 27   |
| 3-3    | Real Vertical Acceleration After Rotation                                                                                                                                                           | 28   |
| 3-4    | Attenuation for Different Integrators                                                                                                                                                               | 31   |
| 3-5    | Real Horizontal Acceleration After Rotation                                                                                                                                                         | 36   |
| 3-6    | FFT of Acceleration in Figure 3-5                                                                                                                                                                   | 37   |
| 3-7    | Velocity After One Integration with<br>Low Frequency Noise Expansion                                                                                                                                | 38   |
| 3-8    | Vertical Displacement of the Pipe at Lock-in<br>at $L/4$                                                                                                                                            | 44   |
| 3-9    | FFT of the Displacement in Figure 3-8                                                                                                                                                               | 45   |
| 3-10   | Horizontal Displacement of the Pipe at Lock-in<br>at $L/4$                                                                                                                                          | 47   |
| 3-11   | FFT of the Displacement in Figure 3-10                                                                                                                                                              | 48   |
| 3-12   | Two-Dimensional Motion Time History at Lock-in<br>at $L/4$ (Figure 3-8 vs. 3-10)                                                                                                                    | 49   |
| 3-13   | In-Line Displacement of the Pipe at Non-lock-in<br>at $L/8$                                                                                                                                         | 51   |
| 3-14   | FFT of the Displacement in Figure 3-13                                                                                                                                                              | 52   |
| 3-15   | Cross-Flow Displacement of the Pipe at<br>Non-lock-in at $L/8$                                                                                                                                      | 53   |
| 3-16   | FFT of the Displacement in Figure 3-15                                                                                                                                                              | 54   |
| 3-17   | Two-Dimensional Motion Time History at<br>Non-lock-in at $L/8$ (Figure 3-15 vs. 3-13)                                                                                                               | 55   |
| 3-18   | Linear Cross-Coherence Between In-Line and<br>Cross-Flow Responses at Non-lock-in                                                                                                                   | 56   |
| 3-19   | Cross-Flow Response Histogram at Non-lock-in                                                                                                                                                        | 58   |
| 3-20   | 2 1/2-Hour Record of the Displacement, Current,<br>and Drag Coefficient for the Pipe at $L/8$                                                                                                       | 60   |
| 3-21   | 2 1/2-Hour Record of the Displacement, Current,<br>and Drag Coefficient for the Bare Cable at $L/6$                                                                                                 | 61   |
| 3-22   | 2 1/2-Hour Record of the Displacement, Current,<br>and Drag Coefficient for the Cable With 2 Light<br>( $L/6$ , $L/2$ ) and 4 Heavy ( $L/3$ , $5L/8$ , $3L/4$ , $7L/8$ )<br>Lumped Masses at $3/4L$ | 62   |
| 3-23   | 2 1/2-Hour Record of the Displacement, Current,<br>and Drag Coefficient for the Faired Cable at $2L/5$                                                                                              | 63   |
| 4-1    | In-Line Displacement at Non-lock-in at $L/8$<br>With 4th, 5th, 6th, and 7th Modes Responding                                                                                                        | 70   |
| 4-2    | FFT of the Displacement in Figure 4-1                                                                                                                                                               | 71   |
| 4-3    | Natural Coordinate Time Histories for the 4th,<br>5th, 6th and 7th Modes of the Pipe                                                                                                                | 72   |

|      | Page                                                                                                      |
|------|-----------------------------------------------------------------------------------------------------------|
| 4-4  | FFT of the 4th Natural Coordinate Time History 73                                                         |
| 4-5  | FFT of the 5th Natural Coordinate Time History 74                                                         |
| 4-6  | RMS of the Natural Coordinates for the 2nd, 3rd, 4th and 5th Cross-Flow Modes of the Pipe 75              |
| 4-7  | RMS of the Natural Coordinates for the 3rd, 4th, 5th, 6th and 7th In-Line Modes of the Pipe 76            |
| 4-8  | Drag Coefficient and Current Corresponding to Figure 4-6 and 4-7 77                                       |
| 4-9  | Drag Coefficient, Current, Total In-Line and Cross-Flow Vibration Energy, and Total Energy of the Pipe 79 |
| 4-10 | Scatter Diagram of Drag Coefficient vs. Total In-Line Vibration Energy in Figure 4-9 80                   |
| 4-11 | Cross-Flow Displacement of the Cable at L/8 83                                                            |
| 4-12 | FFT of the Cross-Flow Displacement in Figure 4-11 84                                                      |
| 4-13 | In-Line Displacement of the Cable at L/8 85                                                               |
| 4-14 | FFT of the In-Line Displacement in Figure 4-13 86                                                         |
| 4-15 | In-Line Natural Coordinate Time Histories for 2nd, 3rd and 4th Modes of the Cable 87                      |
| 5-1  | Power Spectrum of the Test Data $x(t)$ 95                                                                 |
| 5-2  | Power Spectrum of the Test Data $y_1(t)$ 96                                                               |
| 5-3  | Power Spectrum of the Test Data $y_2(t)$ 97                                                               |
| 5-4  | Power Spectrum of the Test Data $y_3(t)$ 98                                                               |
| 5-5  | Power Spectrum of the Test Data $y_4(t)$ 99                                                               |
| 5-6  | Power Spectrum of the Test Data $y_5(t)$ 100                                                              |
| 5-7  | Cross-Bicoherence Between $x(t)$ and $y_1(t)$ 101                                                         |
| 5-8  | Cross-Bicoherence Between $x(t)$ and $y_2(t)$ 102                                                         |
| 5-9  | Cross-Bicoherence Between $x(t)$ and $y_3(t)$ 103                                                         |
| 5-10 | Cross-Bicoherence Between $x(t)$ and $y_4(t)$ 104                                                         |
| 5-11 | Cross-Bicoherence Between $x(t)$ and $y_5(t)$ 105                                                         |
| 5-12 | Power Spectrum of In-line Response at Non-lock-in 107                                                     |
| 5-13 | Power Spectrum of Cross-Flow Response at Non-lock-In 108                                                  |
| 5-14 | Power Spectrum of In-Line Response at Lock-in 109                                                         |
| 5-15 | Power Spectrum of Cross-Flow Response at Lock-in 110                                                      |
| 5-16 | Cross-Bicoherence Between Cross-Flow and In-Line Responses in Figure 5-12 and 5-13 at Non-lock-in 112     |
| 5-17 | Power Spectrum of Cross-Flow Response at Near-lock-in 113                                                 |
| 5-18 | Power Spectrum of In-Line Response at Near-lock-in 114                                                    |
| 5-19 | Cross-Bicoherence between Cross-Flow and In-Line Responses in Figures 5-17 and 5-18 at Near-lock-in 115   |
| 5-20 | Cross-Bicoherence Between Cross-Flow and In-Line Responses in Figures 5-14 and 5-15 at Lock-in 116        |
| 5-21 | Power Spectrum of the Measured Response of Arctic Experiment 119                                          |
| 5-22 | Auto-Bicoherence of the Response in Figure 5-21 120                                                       |
| 6-1  | Cross-Flow Acceleration at Lock-in 128                                                                    |



|                                                                                                                                | Page |
|--------------------------------------------------------------------------------------------------------------------------------|------|
| 6-2 In-Line Acceleration at Lock-in                                                                                            | 129  |
| 6-3 Two-Dimensional Motion Time History of Cross-Flow<br>vs. In-Line Acceleration in Figures 6-1 and 6-2<br>at Lock-in         | 130  |
| 6-4 Residual Time History                                                                                                      | 131  |
| 6-5 Power Spectrum of the Residual in Figure 6-4                                                                               | 132  |
| 6-6 Simulated In-Line Acceleration<br>(Comparing to Figure 6-2)                                                                | 133  |
| 6-7 Two-Dimensional Motion Time History of Cross-Flow<br>vs. Simulated In-Line Acceleration.<br>(Comparing to Figure 6-3)      | 134  |
| 6-8 In-Line Acceleration Component Due to Linear<br>Correlation                                                                | 135  |
| 6-9 In-line Acceleration Component Due to Quadratic<br>Correlation                                                             | 136  |
| 6-10 Two-Dimensional Motion Time History of Cross-Flow<br>vs. Linear In-Line Acceleration<br>( Fig. 6-1 vs. 6-8 )              | 137  |
| 6-11 Two-Dimensional Motion Time History of Cross-Flow<br>vs. Quadratic In-Line Acceleration<br>( Fig. 6-1 vs. 6-9 )           | 138  |
| 7-1 Auto-Bicoherence of Cross-Flow Acceleration<br>in Figure 5-13 at Non-lock-in                                               | 144  |
| 7-2 Quadratic Transfer Function between Cross-Flow<br>and In-Line Acceleration in Figures 5-13 and<br>5-12 at Non-lock-in      | 145  |
| 7-3 Quadratic Systems With Square-Law Operator                                                                                 | 147  |
| 7-4 Linear Transfer Function $H_0(f)$ in Case 1<br>at Non-lock-in                                                              | 153  |
| 7-5 Linear Transfer Function $H_1(f)$ in Case 1<br>at Non-lock-in                                                              | 154  |
| 7-6 Power Spectrum of Residual                                                                                                 | 155  |
| 7-7 Simulated In-Line Acceleration Spectrum<br>at Non-lock-in (Comparing to Figure 5-12)                                       | 156  |
| 7-8 Power Spectrum of the Square of Cross-Flow<br>Acceleration at Non-lock-in (Comparing to<br>Figure 5-12)                    | 157  |
| 7-9 Power Spectrum of the Square of Cross-Flow<br>Acceleration at Near-lock-in (Comparing to<br>Figurw 5-18)                   | 158  |
| 7-10 Linear Cross-Coherence Between In-Line and<br>Square of Cross-Flow Acceleration in Figures<br>5-12 and 7-8 at Non-lock-in | 159  |

## CHAPTER 1

### INTRODUCTION

Many types of ocean-based structures such as marine risers, TLP tension members, deep water pipelines and hydrophone cables are susceptible to vortex-induced vibration. These strumming oscillations are of great practical importance because of their long term destructive effects which may cause failure by fatigue. The implementation of good design procedures that account for strumming vibration is becoming more desirable as the offshore industry moves into deeper water where substantial steady currents are more often encountered.

The problems associated with vortex-induced vibrations have proved to be extremely difficult both theoretically and experimentally due to the complex interaction between structural motions and the vortex-shedding. The well-known wake capture phenomenon is a typical example revealing such a fluid-structure interaction. If one of the natural frequencies of the structure is near the vortex shedding frequency, lock-in can occur and the shedding frequency is captured by, or synchronized with, the structure frequency. The oscillatory lift and drag forces induced by vortex shedding are amplified due to the coupling between structural response and vortex shedding. The complexities

involved in a complete formulation of the flow-induced vibration problem preclude a complete solution at this time.

Several semi-empirical mathematical models formulated with a van der Pol type oscillator have been proposed [9] in an attempt to simulate and/or predict the vortex-induced vibrations in the cross-flow direction. Due to the empirical nature of these models, their performance is not altogether convincing. However, these models were able to produce results which are qualitatively similar to those obtained experimentally. Hartlen and Currie [9], Griffin [11] and Iwan and Blevins [13] covered the field in some detail.

Many of the key developments of the past decade have resulted from experimental investigations of flow-induced oscillations. Considerable experimental work has been conducted to treat various aspects of the problem under controlled laboratory conditions. Sarpkaya [24], Griffin [12] and King [18] have given comprehensive reviews.

The emphasis has been placed mostly on the study of vibration characteristics in the cross-flow direction. The behavior in the in-line direction is much less understood. One peculiar experimental observation in the in-line direction is that the in-line response frequencies do not

always correspond to the structure natural frequencies, instead they are equal to the double or sum of some of the cross-flow response frequencies for both lock-in and non-lock-in cases. No attempt has been made to investigate the relationship between cross-flow and in-line responses, or equivalently, lift and drag forces. Even the answer to the preliminary question of whether they are correlated or independent is still not available. In the design of, for example, a marine riser, the correlation between the response in these two perpendicular directions plays an important role in fatigue life estimation, because of its relation to the stress statistics of the structure.

The purpose of the experiment described in the thesis was to study the relationship between in-line and cross-flow responses of a long flexible cylinder under realistic field conditions. These tests were more realistic than laboratory ones, because it was possible to use a cylinder of sufficient length so that many different natural modes could be excited in both directions thus permitting observation of the relationship, if existent, between them.

Experiments were performed on long flexible cylinders 75 feet in length which were exposed to a uniform currents ranging from 0 to 2.4 feet/second. Measurements taken included current, drag, tension and biaxial acceleration at

seven locations unequally spaced along the test cylinders. The angular orientations of the biaxial accelerometers were initial unknowns, which had to be resolved by evaluation of the gravitational acceleration components recorded with the data. Once the orientation was established the real in-line and cross-flow vector acceleration components were obtained. A numerical double integration technique was developed to determine the vector displacement time histories at the seven measurement locations. By a least squares error minimization method, it was possible to evaluate the individual modal contributions for in-line and cross-flow motions at lock-in and non-lock-in conditions. In other words, the vector displacement response was reduced to the separate time histories of the modal responses of the individual contributing modes. The results of modal analysis show that there exists a strong relation between the drag coefficient and the total vibration energy in these two directions, which represents the behavior of the entire cylinder rather than the local behavior at individual measurement points. This gives the preliminary indication of the existence of a relationship between them.

Linear spectral analysis of the non-lock-in random response indicated that the response in the cross-flow versus in-line directions were almost linearly independent;

therefore, a nonlinear relationship was expected. The frequency doubling and summing phenomena suggested that a higher order spectral analysis was required to investigate the nonlinear interaction which might exist between in-line and cross-flow responses. The bispectrum, which is a cumulant average of a product of three spectral components, was then used to detect the existence of quadratic correlation. The cross-bicoherence spectrum provides evidence of the existence of a quadratic correlation between cross-flow and in-line response.

To determine the fractions of linear and quadratic correlations contributing to the nonlinear relationship, a second order system identification was performed for both lock-in and non-lock-in cases. Due to the nature of nearly deterministic lock-in response, a time domain multiple regression method was applied to the lock-in system identification problem, while a frequency domain error minimization method was used for the non-lock-in random vibration case. The results showed that nonlinearities higher than second order were negligible for both lock-in and non-lock-in cases. In-line and cross-flow responses were linearly independent at non-lock-in. Quadratic correlation accounted for all but a small amount of the nonlinear correlation between in-line and cross-flow.

## CHAPTER 2

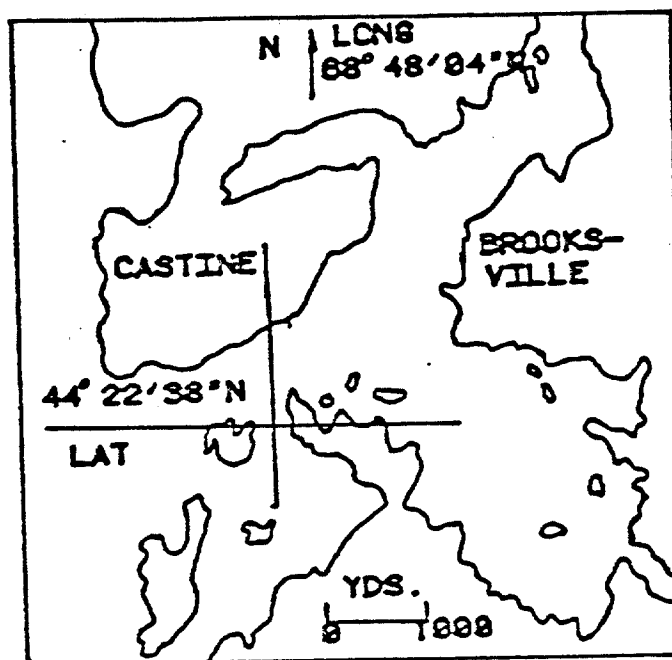
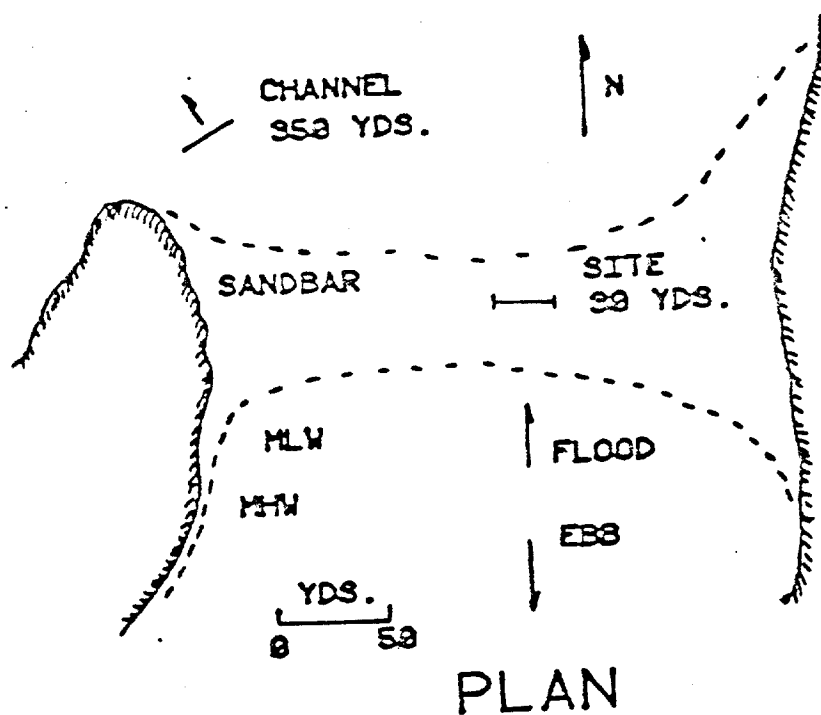
### THE EXPERIMENT

#### 2.1 Test Site

The site chosen for the experiment was a sandbar located at the mouth of Holbrook Cove near Castine Maine as shown in Figure 2-1. At low tide, the sandbar was exposed allowing easy access to the test equipment while at high tide it was covered by about 10 feet of water. The test section was oriented normal to the direction of the current which varied from 0 to 2.4 ft/sec over the tidal cycle with only small spatial differences over the section length at any given moment.

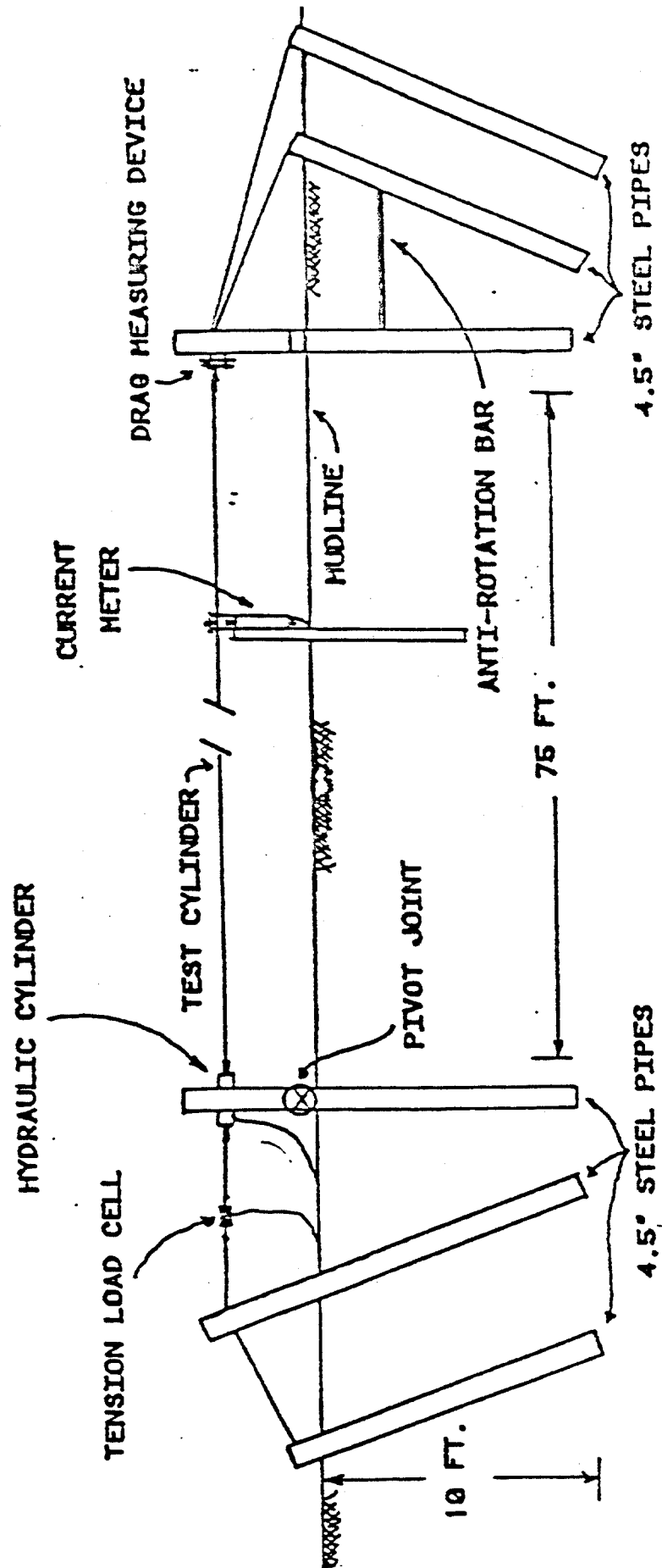
The data taking station for the experiment was the R/V Edgerton chartered from the MIT Sea Grant Program. The Edgerton was moored for the duration of the experiment approximately 300 feet from the sandbar and connected to the instruments on the sandbar by umbilicals.

Prior to the data acquisition part of the experiment, several days were needed to prepare the site. A foundation for the experiment was needed to anchor the supports that were to hold the ends of the test cylinders. To accomplish this, six 4.5 inch diameter steel pipes were water jetted into the sandbar utilizing the fire pump aboard the



FROM NOS CHART 13389





## 2-2 Schematic Diagram of the Experiment Test Section

Edgerton. These six pipes were made of two, five-foot sections joined by a coupling so that the overall length of each was 10.0 feet. In addition, one 2.0 inch steel pipe, 6 feet long, was jetted into the sandbar to be used as a current meter mount. Figure 2-2 shows a schematic diagram of the experiment test section.

## 2.2 Test Cylinder

### 2.2.1 Cable

A 75 foot long instrumented cable was developed specifically for the experiments that were performed in the summer of 1981. The outer sheath for the cable was a single piece of clear flexible PVC tubing, which was 1 1/4 inches in outer diameter by 1.0 inch in inside diameter. Three 1/8 inch diameter stainless steel cables ran through the tubing and served as the tension carrying member. A cylindrical piece of 1/2 inch diameter neoprene rubber was used to keep the stainless steel cables spaced 120 degrees apart. The neoprene rubber spacer was continuous along the length except at seven positions where biaxial pairs of accelerometers were placed. Starting at the east end these positions were at  $L/8$ ,  $L/6$ ,  $L/4$ ,  $2L/5$ ,  $L/2$ ,  $5L/8$ , and  $3L/4$ . These accelerometers were used to measure the response of the cable. The accelerometers were Sundstrand Mini-Pal Model 2180 Servo Accelerometers which are sensitive to the

direction of gravity. Each is 1/2 inch in diameter by 1.5 inches long. The biaxial pairing of these accelerometers made it possible to determine their orientation and hence extract real vertical ( cross-flow ) and horizontal ( in-line ) accelerations of the cable at the seven locations. Three bundles of ten wires each ran along the sides of the neoprene spacer to provide power and signal connections to the accelerometers and to the drag measuring system. An Emerson and Cuming flexible epoxy was used to fill the voids in the cable and make it water tight. The weight per unit length of this composite cable was .7704 lbs/ft in air.

#### 2.2.2 Steel Tubing

In a second set of experiments, the composite cable was placed inside a 1.631 inch O.D. by 1.493 inch I.D. steel tube. The tubing was made of four equal length sections that were joined together. At the internal joints steel nipples were welded to each tube section and stainless steel threaded couplings were used to join them. The tubing was connected to the hydraulic cylinder and to the drag cell mechanism by custom-made universal joints to provide pinned end conditions. These special end connectors also kept the cable inside the tubing under a slight tension, and a neoprene spacer at intervals of 18 inches between the cable

and tubing inhibited any relative motion between the two. The remaining cavity was allowed to fill with water. The weight per unit length of the steel tubing with the cable inside and the voids flooded with water was 2.2344 lbs/ft., in air.

### 2.2.3 Lumped Masses

In another set of experiments, lumped masses were fastened to the bare cable and their effects studied. The lumped masses were PVC cylinders 12.0 inches long and 3.5 inches in diameter. A 1.25 inch hole was drilled through the center of each lump so that the cable could pass through. In addition, four .625 inch holes were drilled symmetrically around this 1.25 inch center hole so that copper tubes filled with lead could be inserted to change the mass of the lumps. In the field, it was difficult to force the cable through the holes drilled in the PVC so each mass was cut in half along the length of its axis. The masses were placed on the cable in halves and held together by hose clamps. Different tests were run by varying the number and location of lumps and by changing the mass of the lumps. The results of these tests will not be reported in this thesis, but may be found in references [15], [20] and [30].

#### 2.2.4 Faired Cable

Finally, 11.6 x 1/16 inch diameter Endeco plastic stranded fairings were applied to the cable to evaluate their effectiveness as strumming suppression devices.

### 2.3 Measurement System

#### 2.3.1 Drag Measuring system

A load cell mounted at one end of the test cylinder measured the horizontal shear force on one end of the test cylinder. The cylinder and its supports were symmetric, and therefore the measured force was one half the total drag force on the cylinder. Mean drag force was measured. The mechanical details of the drag measuring mechanism may be found in the thesis by J. McGlothlin [20]. The load cell was a Sensotec Model 41, packaged for underwater use. The signal from the load cell traveled through wires in the test cylinders and through the umbilical to the Edgerton where it was conditioned and recorded.

#### 2.3.2 Current Measuring System

The current was measured by a Neil Brown Instrument System DRCM-2 Acoustic Current Meter located 12.5 feet from the west end of the test cylinder and 2 feet upstream. It was set so that it determined the current at the level of

the test cylinders. Signals from the current meter traveled through umbilicals to the Edgerton where they were monitored and recorded. In addition, a current meter traverse was performed using an Endeco current meter to determine the spatial differences in current along the test section. The current was found to be spatially uniform to within + or - 3.0% from end to end for all current speeds above 0.5 feet per second.

### 2.3.3 Tension Measuring System

The tension measuring and adjusting system was located at the east end of the experiment test section. Extensions were made to the two inner water jetted posts at this end. As shown in the diagram, a 5-foot extension was made to the center post and a 3-foot extension was made to the inner most post. What made this 3-foot extension different from the rest was that its attachment to the jetted pipe at the mudline was a pin connection as compared to the standard pipe couplings used on the other extensions. This pin connection gave it the ability to pivot in the plane of the posts. Onto this pivoting post, a hydraulic cylinder was mounted, horizontally, 2.5 feet above the mudline. The test cylinder was connected at one end to this hydraulic cylinder and at the other end to the drag measuring device. The test

cylinder was attached 2.5 feet above the mudline, a sufficient distance to avoid any boundary layer effects caused by the sandbar. A cable ran from the back of the hydraulic cylinder to a Sensotec Model RM In-Line load cell which was anchored at the other end to the center post. In this way, the force on the test cylinder was the force seen by the load cell minus a small amount due to friction in the pin. The output from the tension load cell passed through the umbilicals to the Edgerton where it was monitored. A hydraulic hose ran from a hand operated pump on the Edgerton to the hydraulic cylinder so that the tension could be changed as desired. This was not a constant tension system. Stiction in the hydraulic cylinder kept the distance between the attachment points of the test cylinder a constant unless intentionally changed. Therefore, tension varied slowly with current speed and mean drag force.

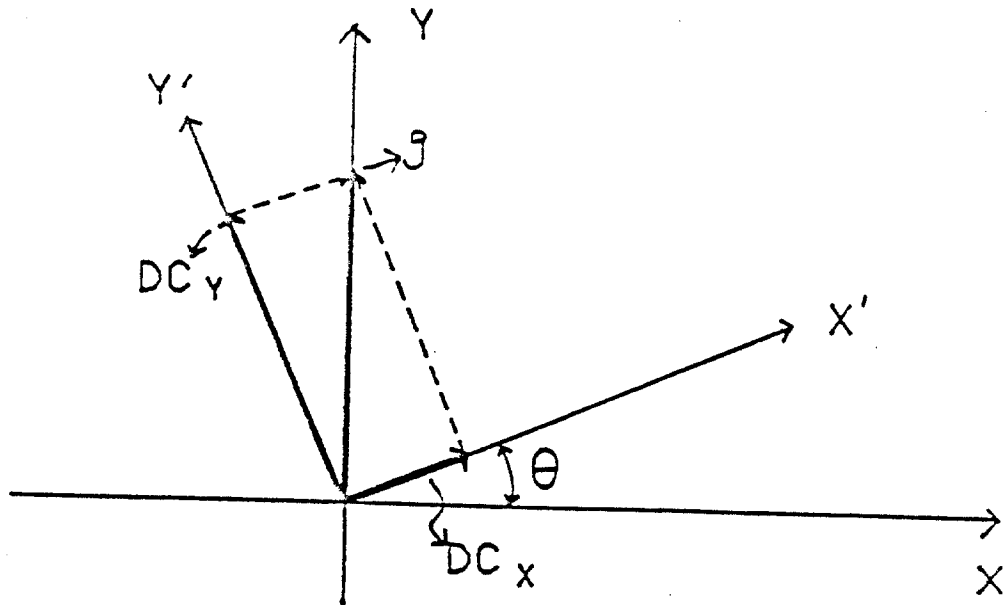
CHAPTER 3  
ANALYSIS OF EXPERIMENTAL DATA

3.1 Vector Rotation of Acceleration Time Series

The orientation of the biaxial accelerometers was initially unknown. Because it was our purpose to study the relation between in-line and cross-flow vibration response, it was necessary to separate the measured acceleration into in-line and cross-flow components. This required determining the accelerometer orientation angle, which then permitted recovery of the in-line and cross-flow components by vector rotation of the acceleration time series. The accelerometers used were sensitive to gravity and gave a DC offset to the recorded signal. Figure 3-1 defines  $x'(t)$  and  $y'(t)$  as the actual orientation of the accelerometer axes.  $\theta$  is the angle of rotation necessary to describe the motion in the desired coordinate system. The  $x'$  and  $y'$  measurements have DC offsets (  $DCx$  and  $DCy$  ) proportional to the component of gravity which was measured in that direction. From these DC offsets the angle  $\theta$  may be obtained.

$$\theta = \tan^{-1} \frac{|DCx|}{|DCy|} + k\pi \quad (3.1.1)$$





VECTOR ROTATION OF  
RAW ACCELERATION

$$\begin{aligned} DC_x &= g \sin \theta \\ DC_y &= g \cos \theta \end{aligned} \quad \Rightarrow \quad \theta = \tan^{-1} \left( \frac{DC_x}{DC_y} \right)$$

$$X(t) = X'(t) \cos \theta - Y'(t) \sin \theta$$

$$Y(t) = X'(t) \sin \theta + Y'(t) \cos \theta$$

3-1 Relation Between Rotated Angle and DC Offset

K depends on the sign of DCx and DCy. After  $\theta$  has been found, the in-line and cross-flow accelerations  $x(t)$  and  $y(t)$  can be found by the vector rotation:

$$x(t) = x'(t)\cos\theta - y'(t)\sin\theta \quad (3.1.2a)$$

$$y(t) = x'(t)\sin\theta + y'(t)\cos\theta \quad (3.1.2b)$$

Figure 3-2 and 3-3 show sample acceleration time histories before and after rotation. Note that the cross-flow acceleration has a DC offset equal to one g or 386.017 in/sec\*\*2.

### 3.2 Integrator

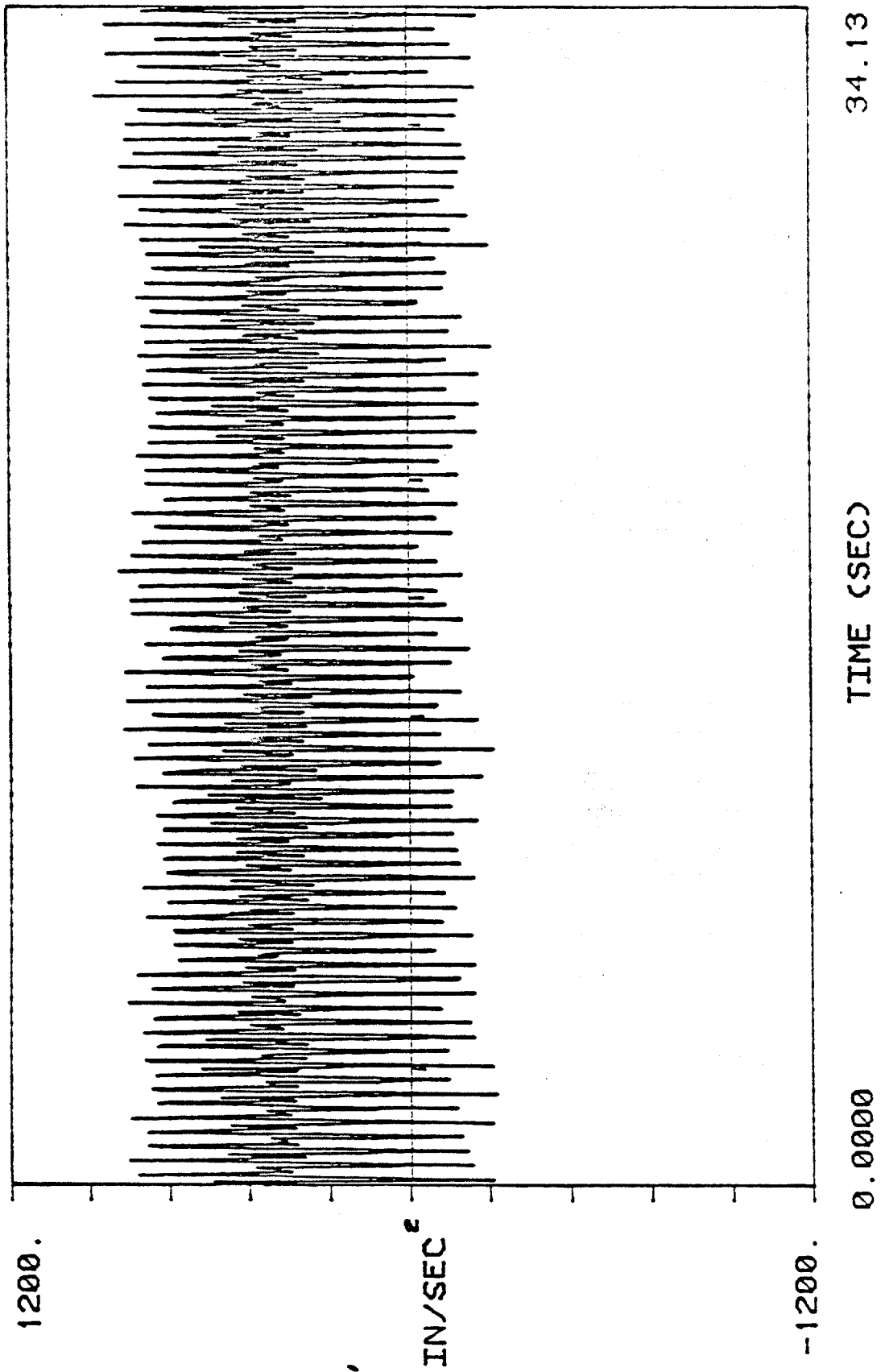
In a continuous time description, equation (3.2.1) represents the integration of acceleration  $a(t)$  to get velocity  $v(t)$ .

$$v(t) = \int_0^t a(t') dt' \quad (3.2.1)$$

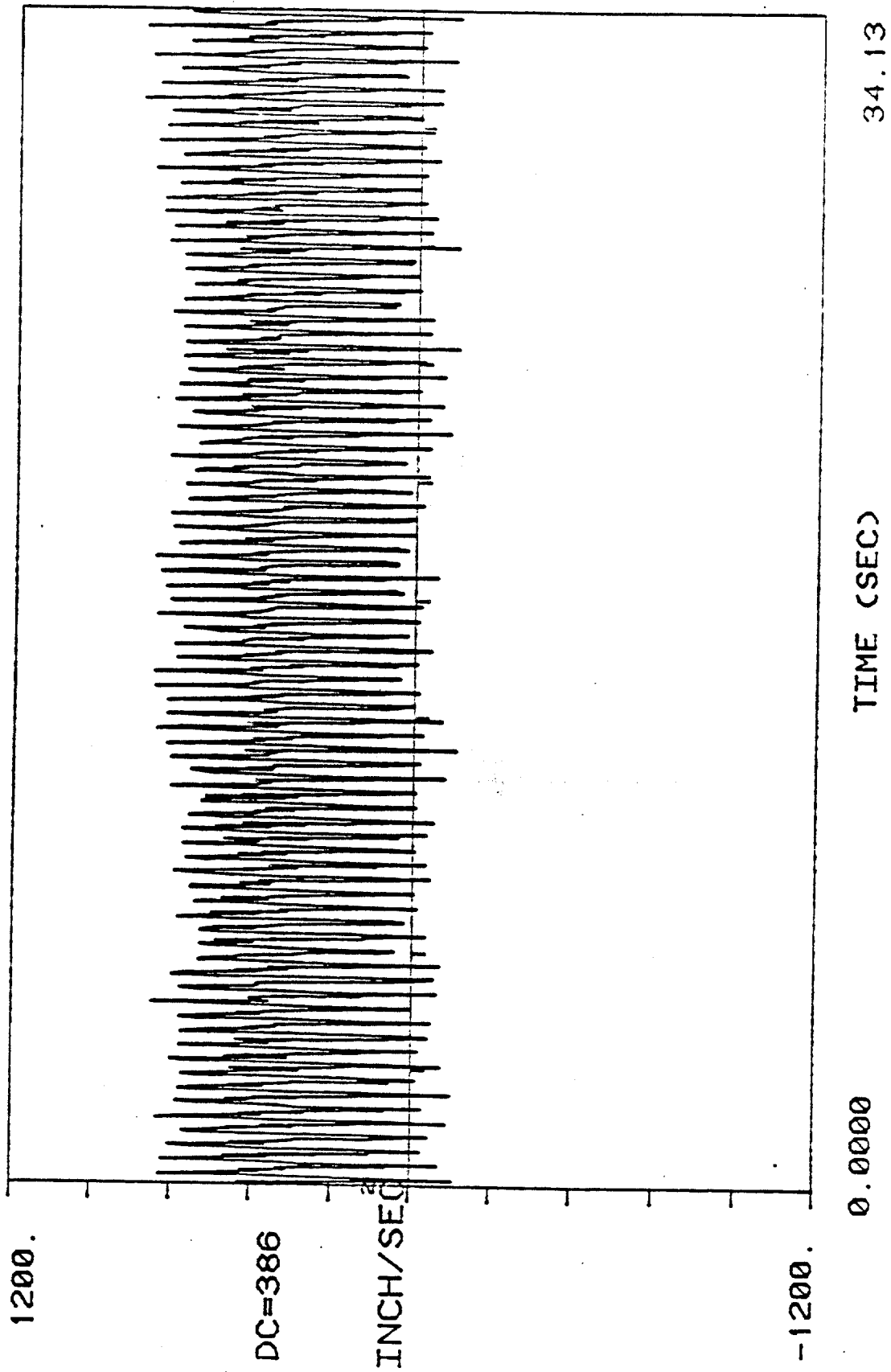
A discrete time approximation for  $v(t)$  can be calculated by a linear constant coefficient difference equation.

$$v[n] = v[n-r] + T \sum_{k=0}^m b[k]a[n-k] \quad (3.2.2)$$

where  $r$  is the order of the filter and the  $b(k)$  are the filter coefficients,  $m$  is the degree of the filter, and  $T$  is the sampling period.



3-2 Recorded Acceleration Before Rotation



3-3 Real Vertical Acceleration After Rotation

Generally, the properties of digital integrators have been developed in the time domain by fitting the data points with a smooth curve. The time domain interpretation as presented in equation 3.2.2 has an equivalent frequency domain formulation. The Z-transform of equation (3.2.2) leads to the system function  $H(z)$ :

$$H(Z) = T \frac{\sum_{k=0}^m b[k] Z^{-k}}{1-Z^{-r}} \quad (3.2.3)$$

Evaluating  $H(z)$  on the unit circle of the z-plane yields the frequency response function  $H(w)$ . If the numerator of  $H(z)$  is a mirror image polynomial then forward and backward integration in time will yield the same result. This leads to:

$$H(W) = T \exp[-i(\frac{m-r}{2})W] \frac{\sum_{k=0}^{[m/2]} 2b(k) \cos(\frac{m}{2} - k)W}{i \sin(rW/2)} \quad \text{for } m \text{ odd} \quad (3.2.4a)$$

$$H(W) = T \exp[-i(\frac{m-r}{2})W] \frac{\frac{1}{2} b(\frac{m}{2}) + \sum_{k=0}^{m/2-1} b(k) \cos(\frac{m}{2} - k)W}{i \sin(rW/2)} \quad \text{for } m \text{ even} \quad (3.2.4b)$$

The frequency response function for an ideal integrator is:

$$H_I(W) = T/(iW) \quad (3.2.5)$$

Recognizing that, if  $x(n)$  and  $X(w)$  are a Fourier transform pair, then  $x(n-m)$  and  $X(w)\exp(-iwm)$  are also a Fourier transform pair. Any system function that can be written as:

$$H(iW) = -i |H(iW)| \exp[-ikW] \quad (3.2.6)$$

where  $K$  is a constant, is a linear phase shift system. Let  $x(n)$  be the input to  $H(w)$  in equation (3.2.4) and  $H_i(w)$  in equation (3.2.5) with  $y(n)$  and  $y'(n)$  being the respective outputs. Rewriting  $H(w)$  and  $H_i(w)$  as:

$$H(iW) = -i |H(iW)| \exp[-i(\frac{m-r}{2})W] \quad (3.2.7)$$

$$H_I(iW) = -i |H_I(iW)| \quad (3.2.8)$$

Then the transfer function between  $y(n)$  and  $y'(n)$  is,

$$\frac{Y(iW)}{Y_I(iW)} = \frac{|H(iW)|}{|H_I(iW)|} \exp(-i\frac{m-r}{2}W) \quad (3.2.9)$$

There is a linear phase shift between the ideal integrator result and this integrator result. A comparison of the magnitudes of (3.2.4) and (3.2.5) can be used to examine the accuracy of the integrator. An error measurement  $E(w)$  is defined as:

$$E(W) = 20 \log \frac{|H(W)|}{|H_I(W)|} = 20 \log W |H(W)| \quad (3.2.10)$$

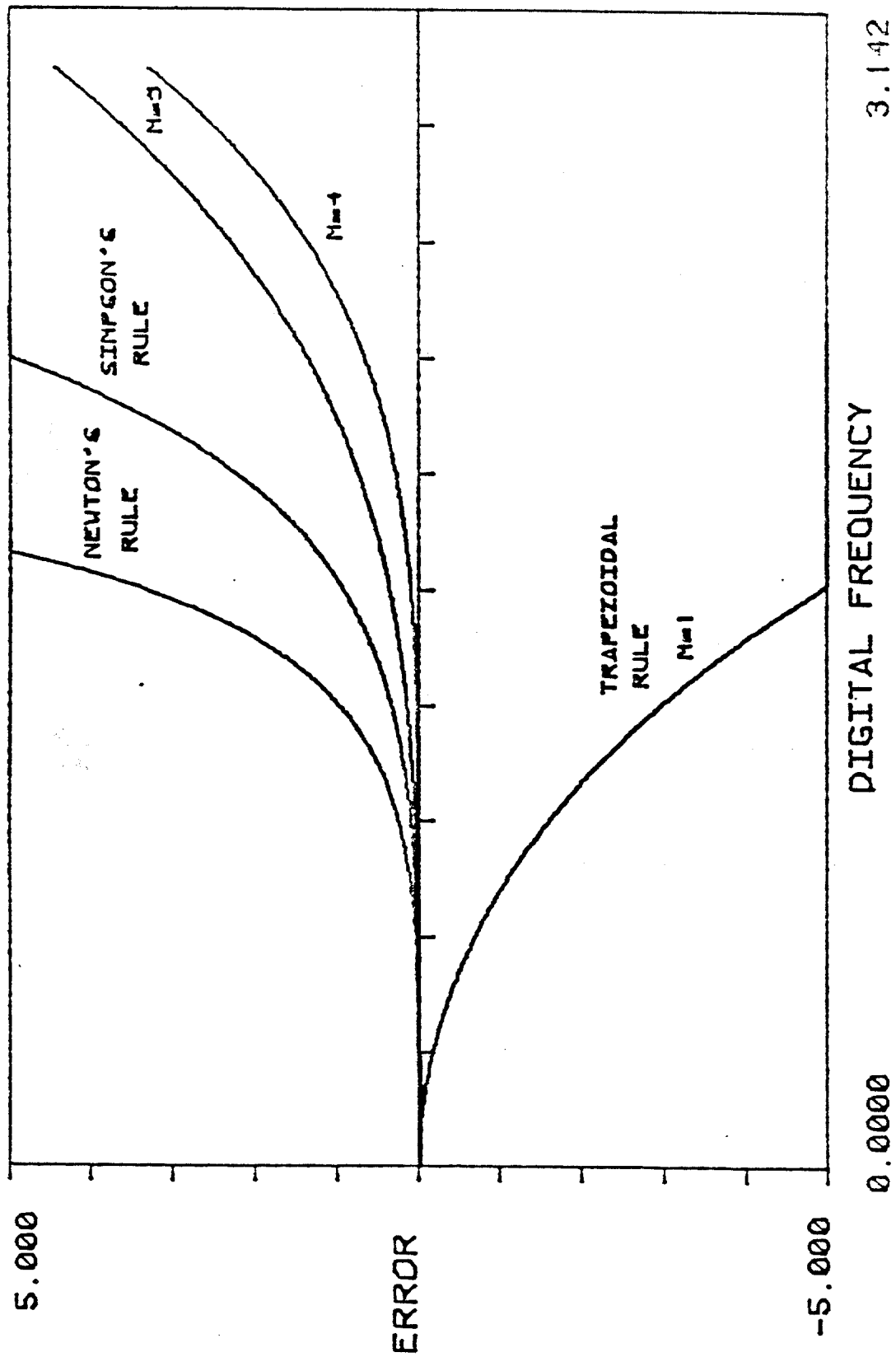


Figure 3-4 shows  $E(w)$  for a variety of integrators. The choice of integrator is highly dependent on the dominant frequency range of the time series relative to the sampling frequency. As an example, if the data were sampled at a relatively high frequency and most energy of the signal concentrate at a frequency lower than  $0.1\pi$ , then the trapezoidal rule integration would be the appropriate one to use. For the Castine experiment, the sampling frequency was 30 Hz, and the typical frequency range for the cylinder response was from 2 to 9 Hz. This corresponds to dimensionless digital frequencies in the range from  $0.13\pi$  to  $0.6\pi$  where  $\pi$  corresponds to half the sampling frequency. Figure 3-4 shows that the error for Trapezoidal rule integration in this range is from 2% to 50%, and 0.1% to 10% for Simpson's rule. The errors are larger at the higher frequencies. Many maximally flat integrators have been presented in the literature (25). Figure 3-4 shows two examples for filters of degree  $m=2$  and 4. The error for  $m=4$  is reduced to a maximum of 0.5% at the highest frequency of interest.

Schuessler and Ibler (25) pointed out two basic mistakes in the application of this integration formula. First, the filter coefficients  $b(k)$  should be time-varying instead of constant according to the equation:



$$b(k,n) = \begin{cases} b(k) u(n-r+k) & k=0,1,\dots,(r-1) \\ b(k) & k=r,r+1,\dots,m \end{cases} \quad (3.2.11)$$

where  $b(k)$  are filter coefficients and  $u(k)$  is a unit step function. The reason is that according to the continuous integration equation (3.2.1)  $v(0)=0$  must hold. But by using the digital integrator (3.2.2),  $v(0)=b(0)a(0)$  rather than zero. If (3.2.10) is used,  $v(0)=b'(0,0)a(0)=b(0)u(-r)a(0)=0$  which yields the correct result. Second, the Newton-Codes formulas are, in fact, valid only for  $n=i*r$  with  $i=0,1,2,\dots$ , so Schuessler and Ibler proposed that the sampling frequency at input and output should be different. This is accomplished by applying an interpolator to the input sequences before the integrator is applied. The combination of the interpolator and integrator into one system led them to propose a new integration formula.

$$v(n) = v(n-1) + T/3 \sum_{k=0}^{2L-1} b'(k,n) a(n-k) \quad (3.2.12)$$

where  $L$  is the length of the interpolator and

$$b'(n,k) = \begin{cases} b(k) u(n-L+k) & 0 \leq k \leq L-1 \\ b(k) & L \leq k \leq 2L-1 \end{cases} \quad (3.2.13)$$

### 3.3 Low Frequency Noise Expansion

The vibration velocity,  $v(t)$ , and displacement,  $d(t)$ , can be obtained from the acceleration,  $a(t)$ , by numerical

integration. If  $v(0)$  is the initial velocity at  $t=0$ , the time of the start of data collection, then

$$v(t) = v(0) + \int_0^t a(t') dt' \quad (3.3.1)$$

The initial velocity  $v(0)$  is unknown. However, a bounded displacement  $d(t)$  is desired. This requires that there be no linear trend or DC component in the velocity  $v(t)$ . The value  $v(0)$  can be arbitrarily set to zero. Following the integration of  $a(t)$  a straight line is fitted to  $v(t)$ . The offset and trend which are found may be then removed from  $v(t)$ . Equation (3.3.1) can be rewritten as:

$$v(t) = a(t) * u(t) \quad (3.3.2)$$

where  $u(t)$  is the unit step function and  $*$  denotes a convolution integral. Taking the Fourier transform of equation (3.3.2) yields:

$$V(W) = A(W) [ \pi \delta(w) + 1/(iW) ] = A(0) \pi + A(W)/(iW) \quad (3.3.3)$$

$$A(0) = \int_{-\infty}^{\infty} a(t) dt \quad (3.3.4)$$

The term  $A(0)$  can be removed by fitting a straight line to  $a(t)$  to remove any linear trend or DC component in acceleration  $a(t)$ . The transfer function between  $a(t)$  and  $v(t)$  is:

$$H(W) = V(W)/A(W) = 1/(iW) \quad (3.3.5)$$

The same procedure can be applied to integrate  $v(t)$  to get  $d(t)$  except that the assumption for the zero mean  $d(t)$  is no longer true. But, we are interested only in the dynamic response of the cylinder, so  $d(0)$  can be set arbitrarily. Integration has characteristics of a low-pass filter with a gain which goes to infinity as the frequency goes to zero. This leads to the undesirable expansion of low frequency noise in the integration process. Figure 3-5 shows a sample of an acceleration time series. Figure 3-6 is the FFT of this acceleration. A negligible component of low frequency noise is shown. Figure 3-7 show that after integration, low frequency noise blew up in the velocity time series.

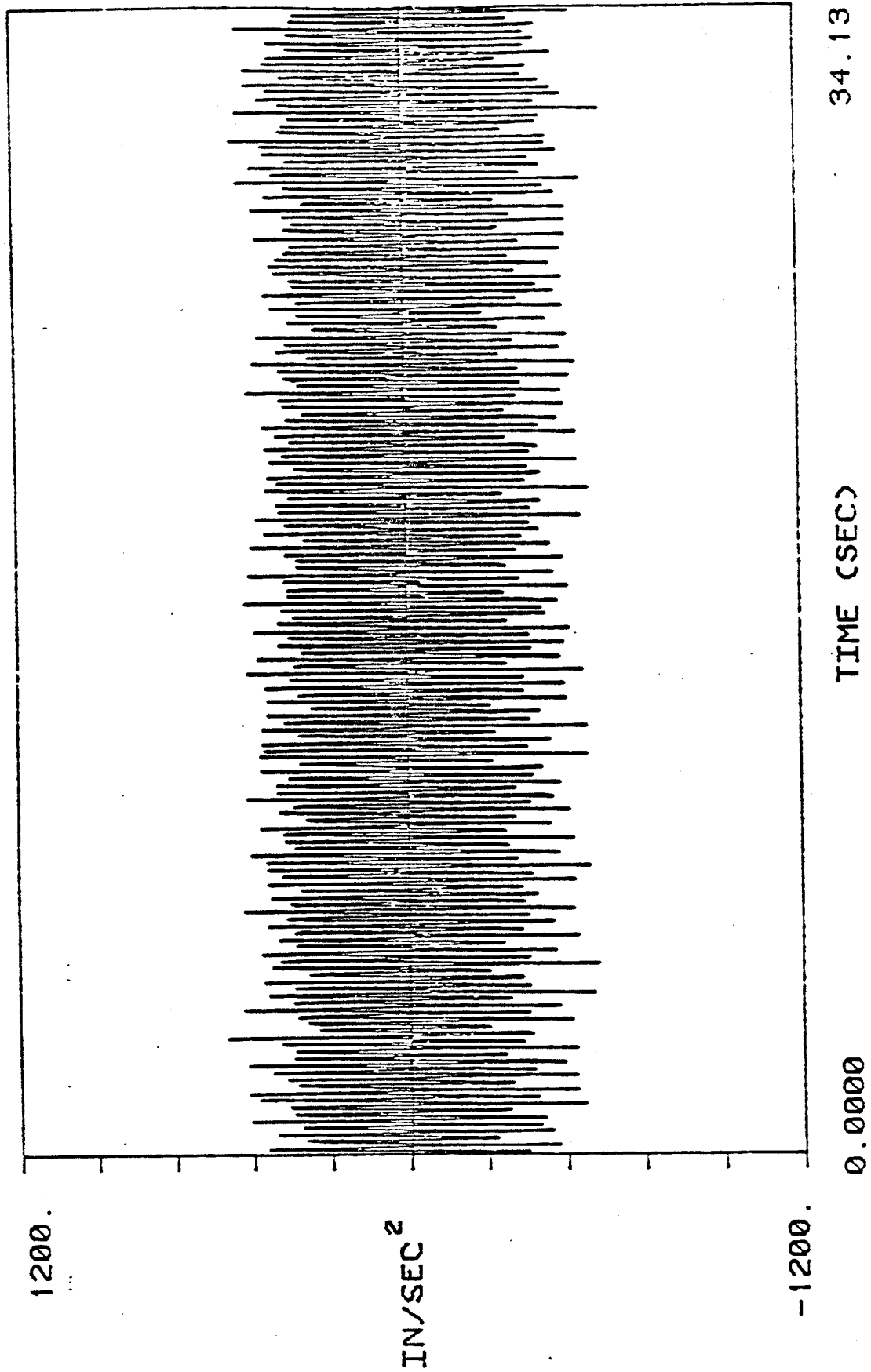
This reveals that low frequency noise expansion leads to unacceptable integration errors. To correct the problem, a high-pass filter is required.

### 3.4 High-Pass Filter

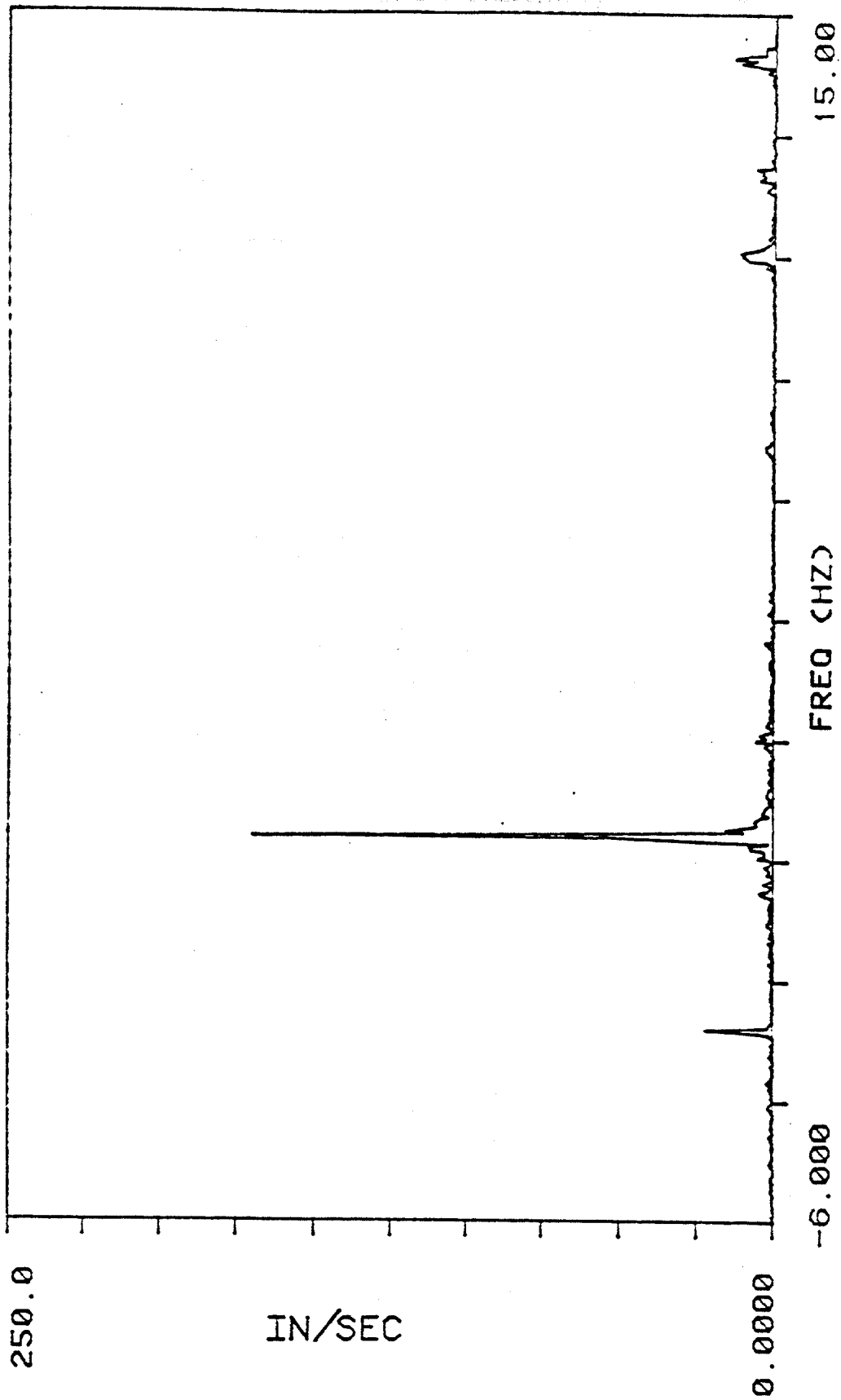
A linear digital filter is a linear time-invariant system represented by a linear constant coefficient difference equation [22]:

$$y[n] = \sum_{k=1}^N a_k y[n-k] + \sum_{k=0}^M b_k x[n-k] \quad (3.4.1)$$

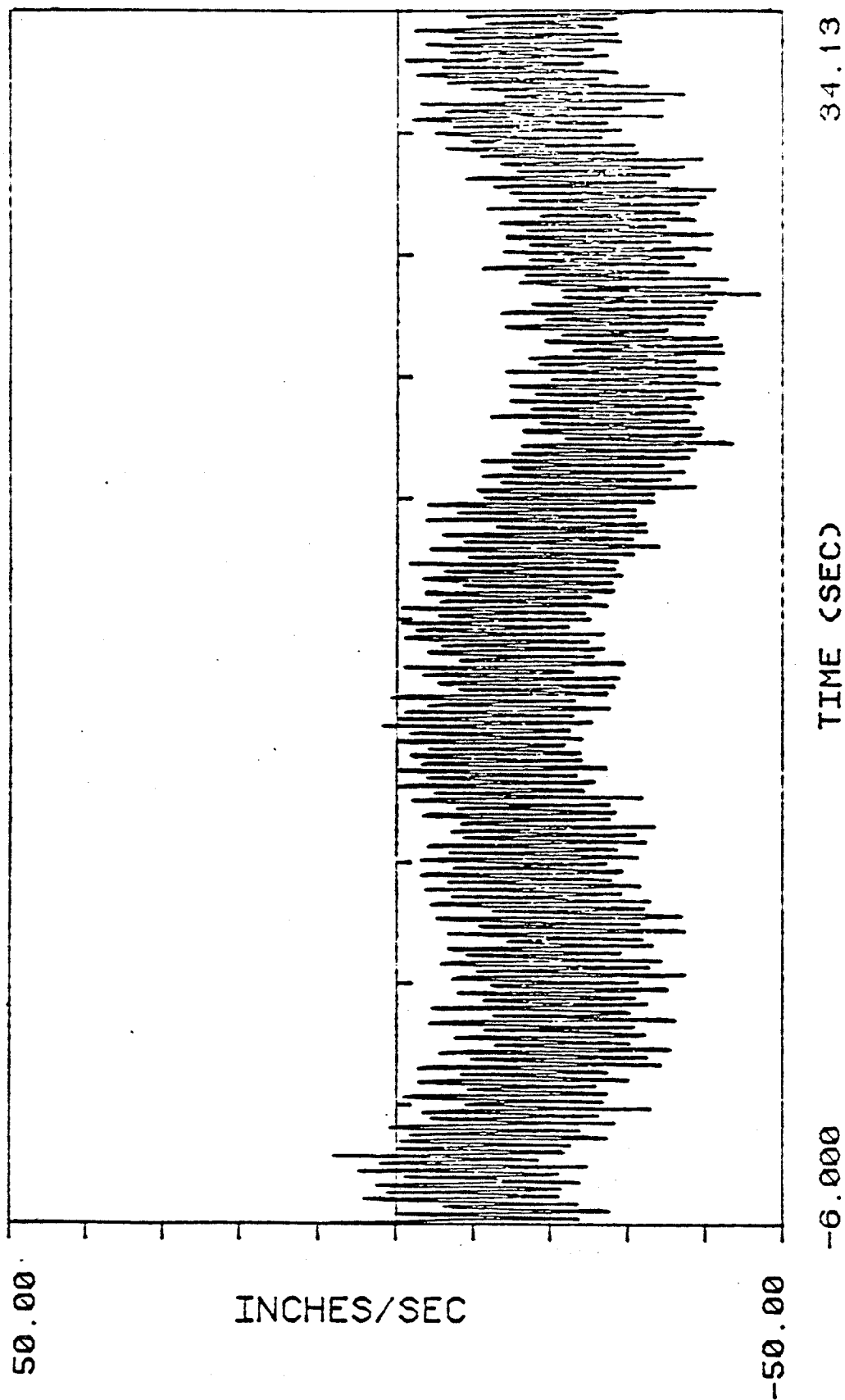
The corresponding system function is given by



3-5 Real Horizontal Acceleration After Rotation



3-6 FFT of Acceleration in Figure 3-5



3-7 Velocity After One Integration with  
Low Frequency Noise Expansion

$$H(z) = \frac{\sum_{k=0}^M b_k z^{-k}}{1 - \sum_{k=1}^N a_k z^{-k}} \quad (3.4.2)$$

where  $x(n)$  is the input signal,  $y(n)$  is the output signal, and  $a_k$  and  $b_k$  are filter coefficients. For a stable causal filter all the poles of this system function must lie inside the unit circle.

For an ideal low-pass (or high-pass) filter, the transfer function magnitude contains a sharp discontinuity at the cut-off frequencies and the required filter order is infinite. Thus a transition band at the cut-off frequencies and a tolerance error in pass-band and stop-band are provided to approximate the desired filter.

If the system function  $H(z)$  in (3.4.2) contains poles solely at the origin, the filter is called a finite impulse response (FIR) filter. Otherwise it is an infinite impulse response (IIR) filter.

a FIR filter is always stable and a linear phase is always achievable by choosing a symmetric impulse response function. For the same desired filter characteristics, the FIR filter must be of a much higher order than the comparable IIR filter, and therefore the FIR filter may require more computer time. However, IIR filter always has

nonlinear phase characteristics. As a consequence, the choice of IIR or FIR filter is dependent on the desired phase requirement as well as computer time efficiency. For this research, both of these filters are used and it depends on the particular purpose in the data analysis. For the modal analysis the phase informations are important and the FIR filter was used. While in the RMS response calculation of the 2 and 1/2 hours long records, the IIR filter was used for the purpose of computer efficiency.

McClellan, Parks and Rabiner [19] formulated the FIR filter design problem in terms of a weighted Chebyshev approximation problem and solved it using the Remez multiple exchange algorithm. The relative approximation error in these optimal filters is spread out uniformly in frequency, so a lower filter order would be sufficient. A computer program for the design of an IIR elliptic filter has been published by Gray and Markel [10]. The elliptic filter possesses the equiripple characteristics and has been widely used to achieve the restrictive frequency domain requirement. The above FIR and IIR filters design method was used in the double integration procedure.

The following procedures, outlined by Rabiner and Gold [23], could be used to eliminate the nonlinear phase effect of an IIR filter. Let  $x(n)$  and  $y(n)$  be the sequences before



and after the filter respectively.  $R$  is the time inverse device, and  $H(z)$  is the filter system function. These can be used in the following sequence

$$x[n] \longrightarrow [H(z)] \xrightarrow{r[n]} [R] \xrightarrow{s[n]} [H(z)] \xrightarrow{t[n]} [R] \longrightarrow y[n]$$

$$R(W) = X(W) H(W)$$

$$S(W) = R(-W) \quad (3.4.3)$$

$$T(W) = S(W) H(W)$$

$$Y(W) = T(-W)$$

These relations imply the following:

$$Y(W) = X(W)H(W)H(-W) = X(W) |H(W)|^2 \quad (3.4.4)$$

The new system function between  $x(n)$  and  $y(n)$  is the square of the magnitude of the original filter's system function and has zero phase shift. However, since this zero phase condition is achieved by applying the IIR filter twice, i.e., on the signal itself and on a time reversed version of the once filtered signal, filter transients will exist on both ends of the resultant signal.

### 3.5 Double Integration Procedures

A summary of the procedure for double integration of a digital acceleration signal follows. The procedure contains the following steps:

1. Obtain the acceleration spectrum and divide it by  $w^4$  to obtain the theoretical displacement spectrum. Use these two spectra as a subjective aid in the determination of the high-pass cutoff frequency necessary for the prevention of low-frequency noise expansion.
2. Using the method of least squares, fit a straight line to the block of data to be integrated. Use this to remove DC offset and any linear trends from the data prior to integration. The typical block length is 1024 data points in the results presented here.
3. High-pass filter the signal using either IIR or FIR filter to remove any low frequency noise. The choice of the type of filter is based on the discussion in section 3.4
4. Integrate the signal using the Schuessler-Ibler integrator.
5. Repeat step 2 to step 4 for the second integration to obtain the displacement signal from velocity.
6. Least squares fit a straight line to the displacement signal to remove any linear trend or offsets.

7. High-pass filter the displacement signal to remove low frequency components that were expanded in the integration.

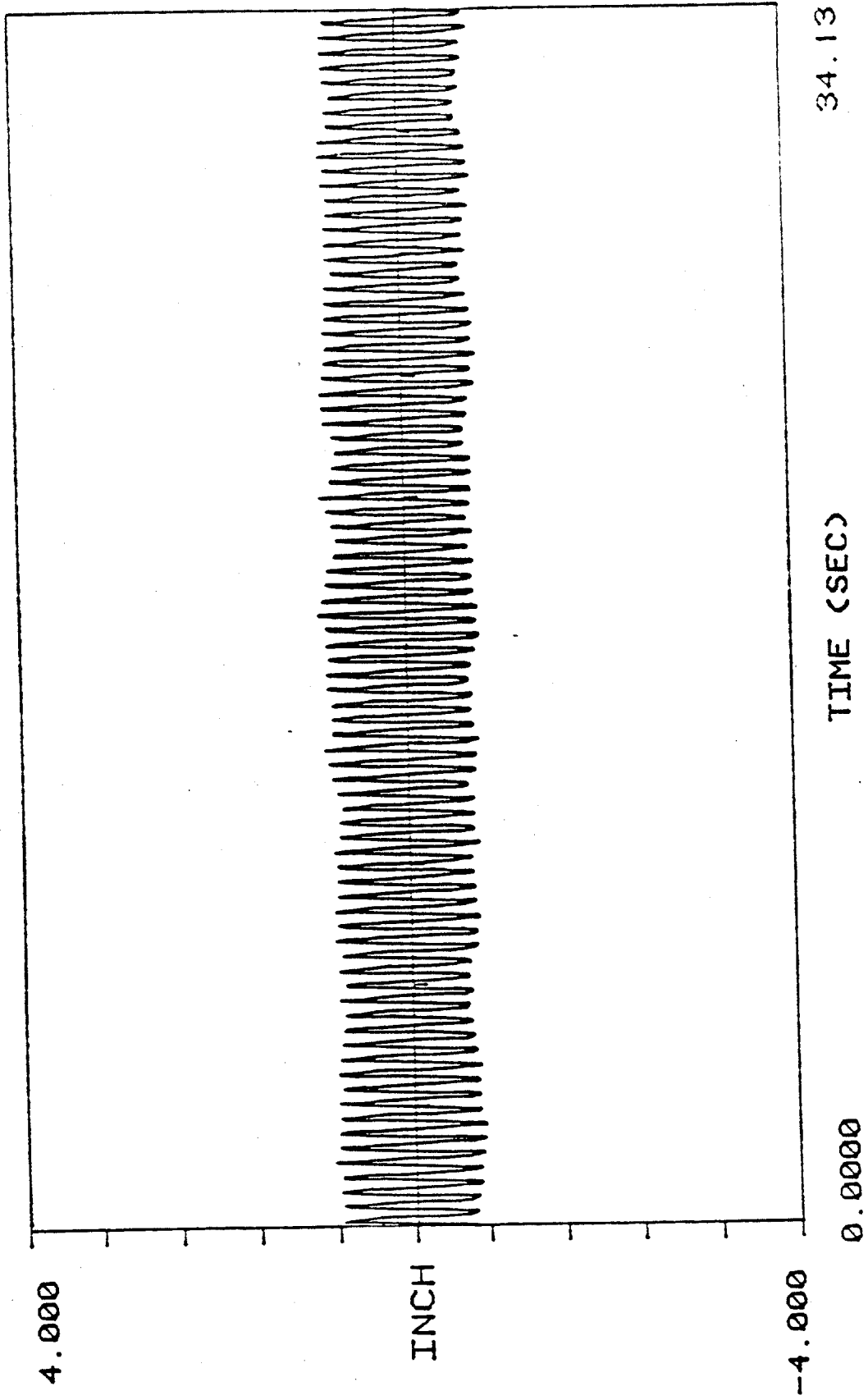
It must be emphasized here that the choice of integrator is highly data dependent as discussed in section 3.2. The Schuessler and Ibler integrator is appropriate for the Castine data but may not be a good choice for other data.

### 3.6 Cylinder motion at Lock-in and Non-lock-in

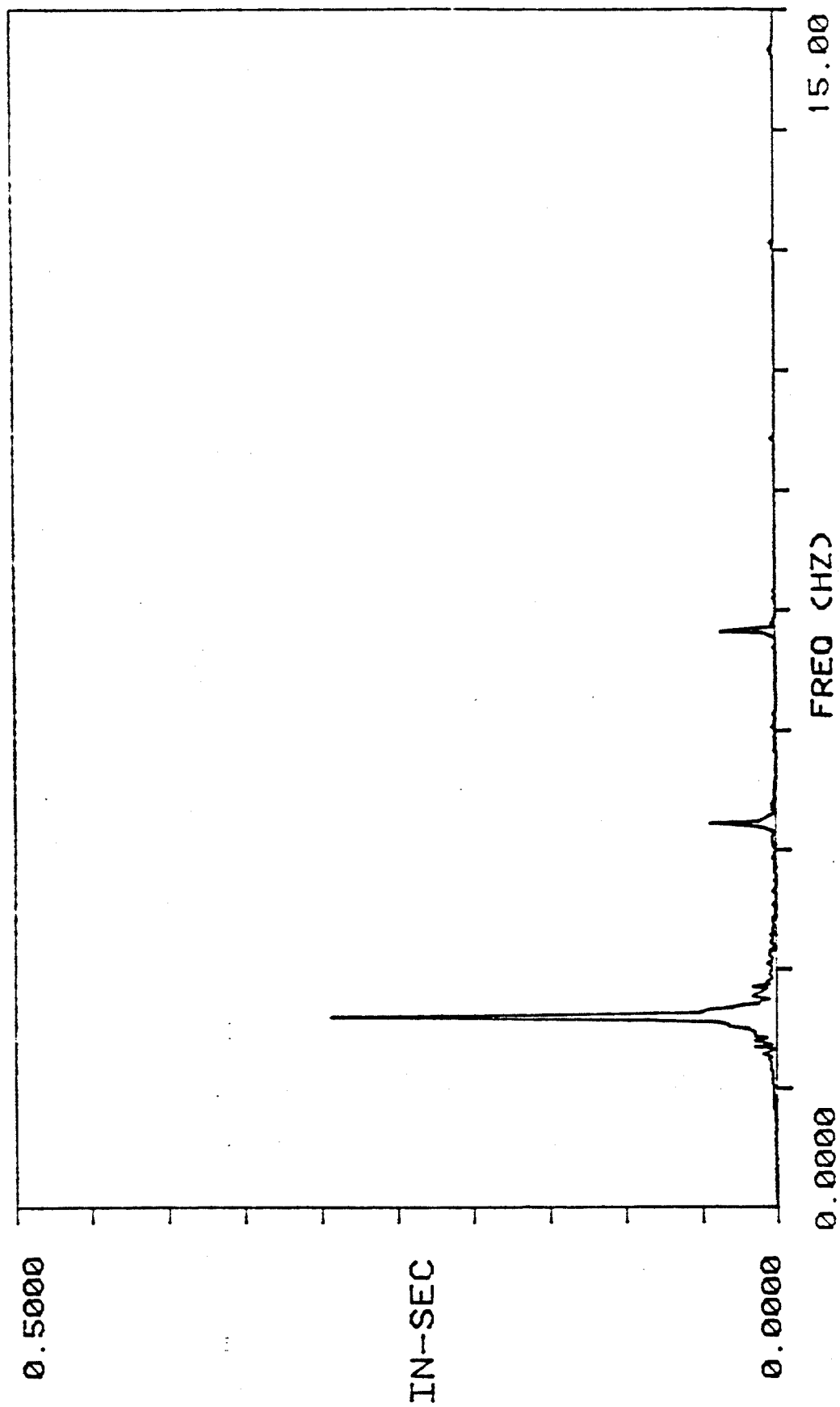
In the preceeding sections, the data analysis process was presented, including vector rotation, high-pass filter and double integration procedures. In this section, typical analysis results of cylinder motion at lock-in and non-lock-in are presented. Compressed 2 1/2-hour records of drag coefficient, current speed, and RMS displacement response are also presented.

#### 3.6.1 Cylinder Motion at Lock-in

Lock-in occurs when the vortex shedding frequency falls within a few percent of a natural frequency of the cylinder. The vortex shedding process is synchronized with the cylinder's motion, and a stable nearly sinusoidal transverse displacement of nearly constant amplitude is observed. Figure 3-8 shows an example of cross-flow displacement of



3-8 Vertical Displacement of the Pipe at Lock-In at  $L/4$

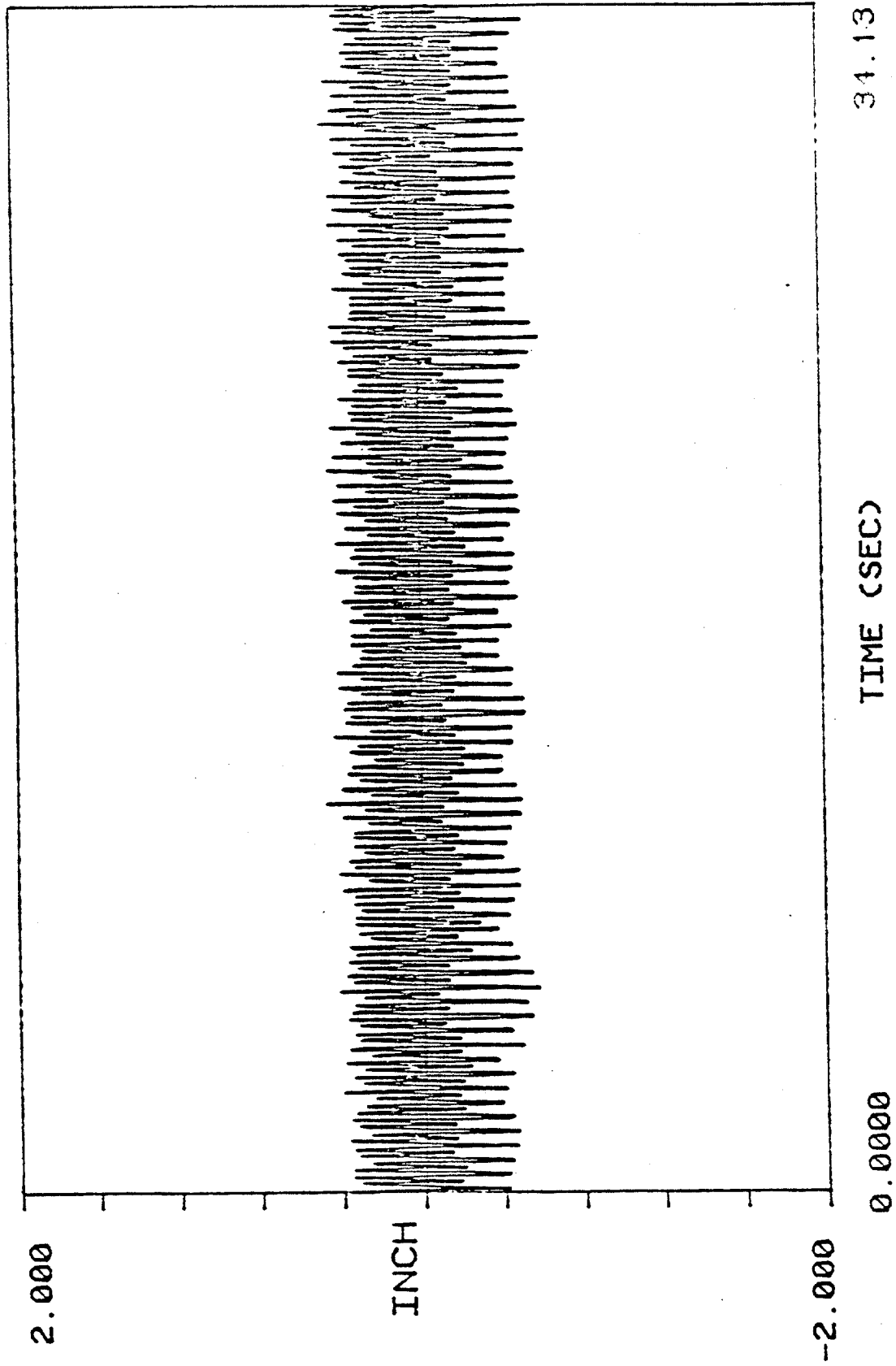


3-9 FFT of the Displacement in Figure 3-8

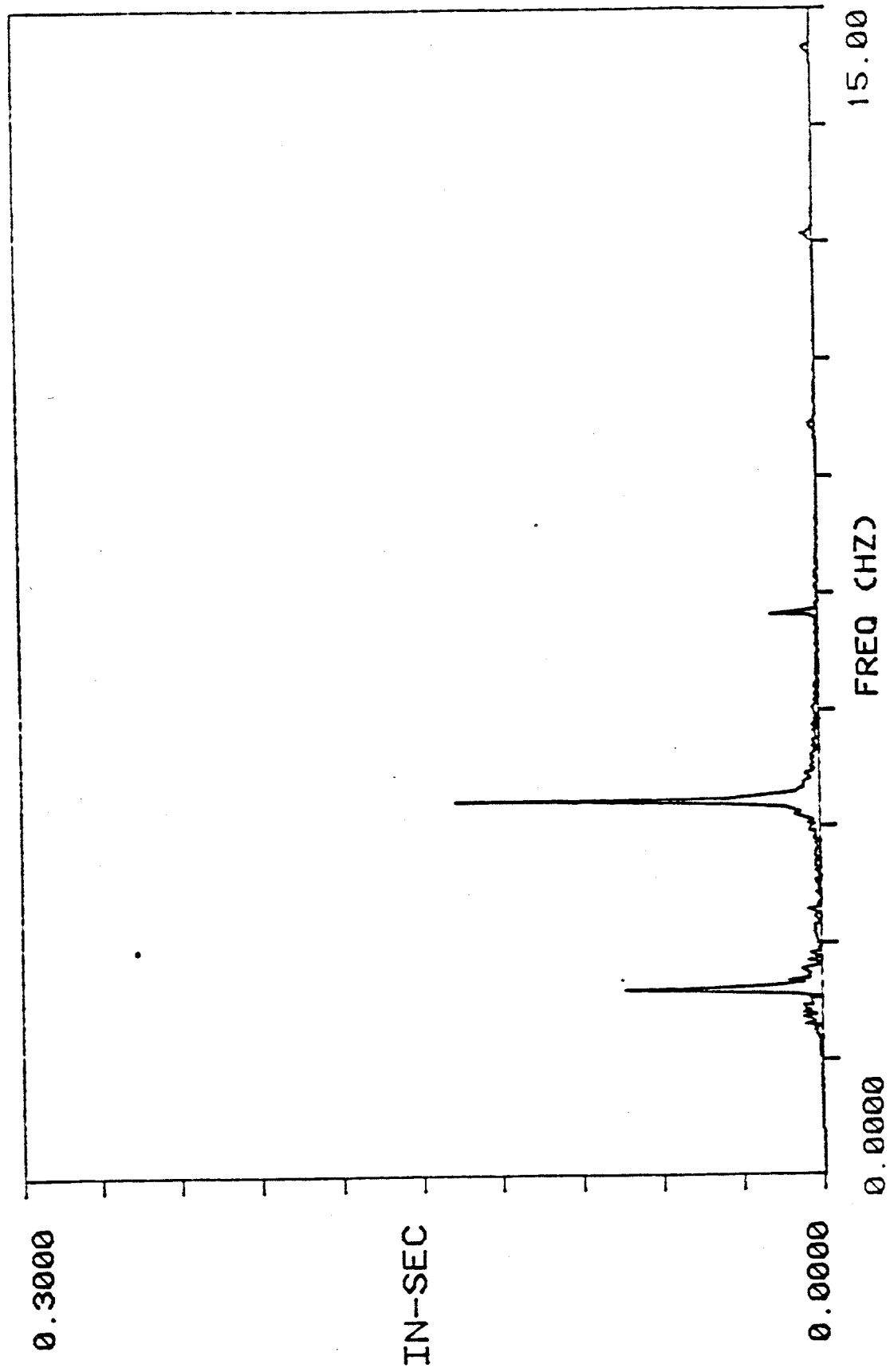
the pipe at  $L/4$  during lock-in with the third mode. Figure 3-9 is the corresponding magnitude of FFT. A single dominant peak is observed.

In the in-line direction, the motion is quite different from the cross-flow response at lock-in. A periodic but nonsinusoidal displacement is observed in the in-line direction as shown in figure 3-10. Figure 3-11 presents the magnitude of the FFT. One important observation in this result is that the dominant frequency in the in-line direction is exactly double that in the cross-flow direction. This frequency doubling phenomenon is always observed at lock-in case.

By double integration of both measured in-line and cross-flow acceleration time histories, it is possible to plot the trajectory of the motion of a point on the cylinder. Figure 3-12 shows the motion at  $L/4$  projected onto a plane which is normal to the cylinder axis. In this case the cross-flow motion was locked-in at third-mode and the in-line motion was at twice the frequency of the cross-flow motion and was dominated by response in the fifth-mode. A small amount of third-mode motion also appears in the in-line response. Without it there would be nearly perfect figures of eight.

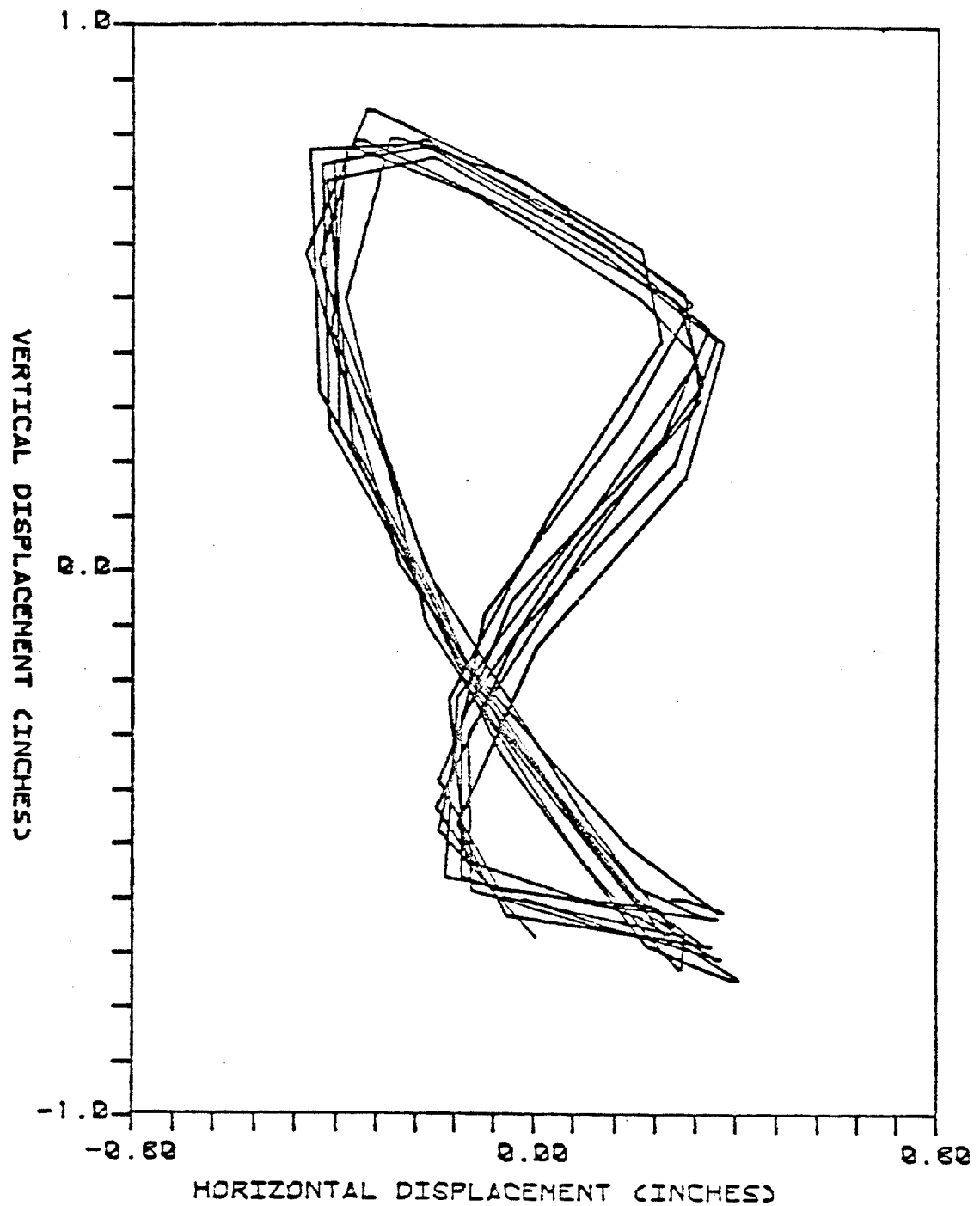


3-10 Horizontal Displacement of the Pipe at Lock-in at L/4



3-11 FFT of the Displacement in Figure 3-10



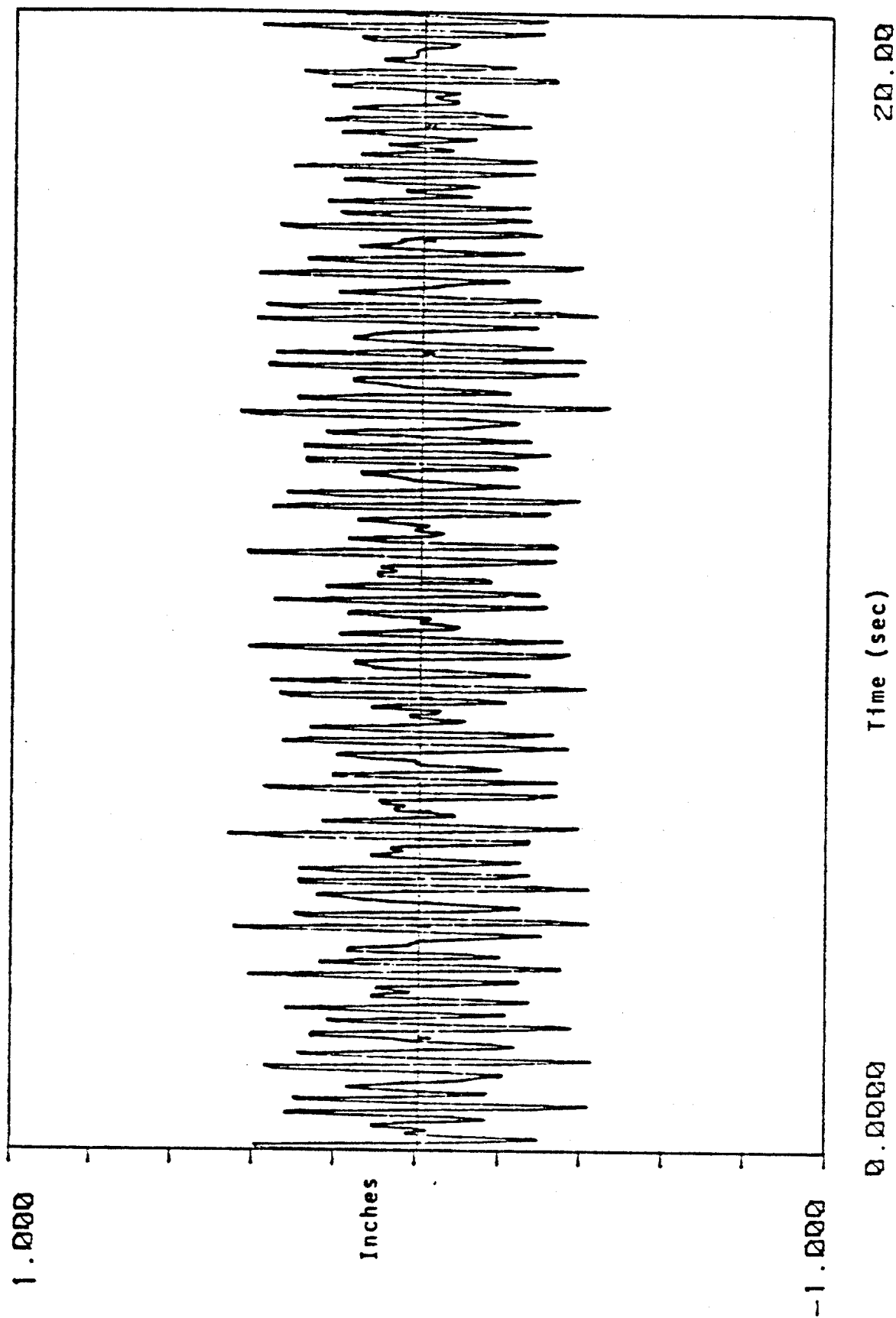


3-12 Two-Dimensional Motion Time History at Lock-in at L/4  
(Figure 3-8 vs. 3-10)

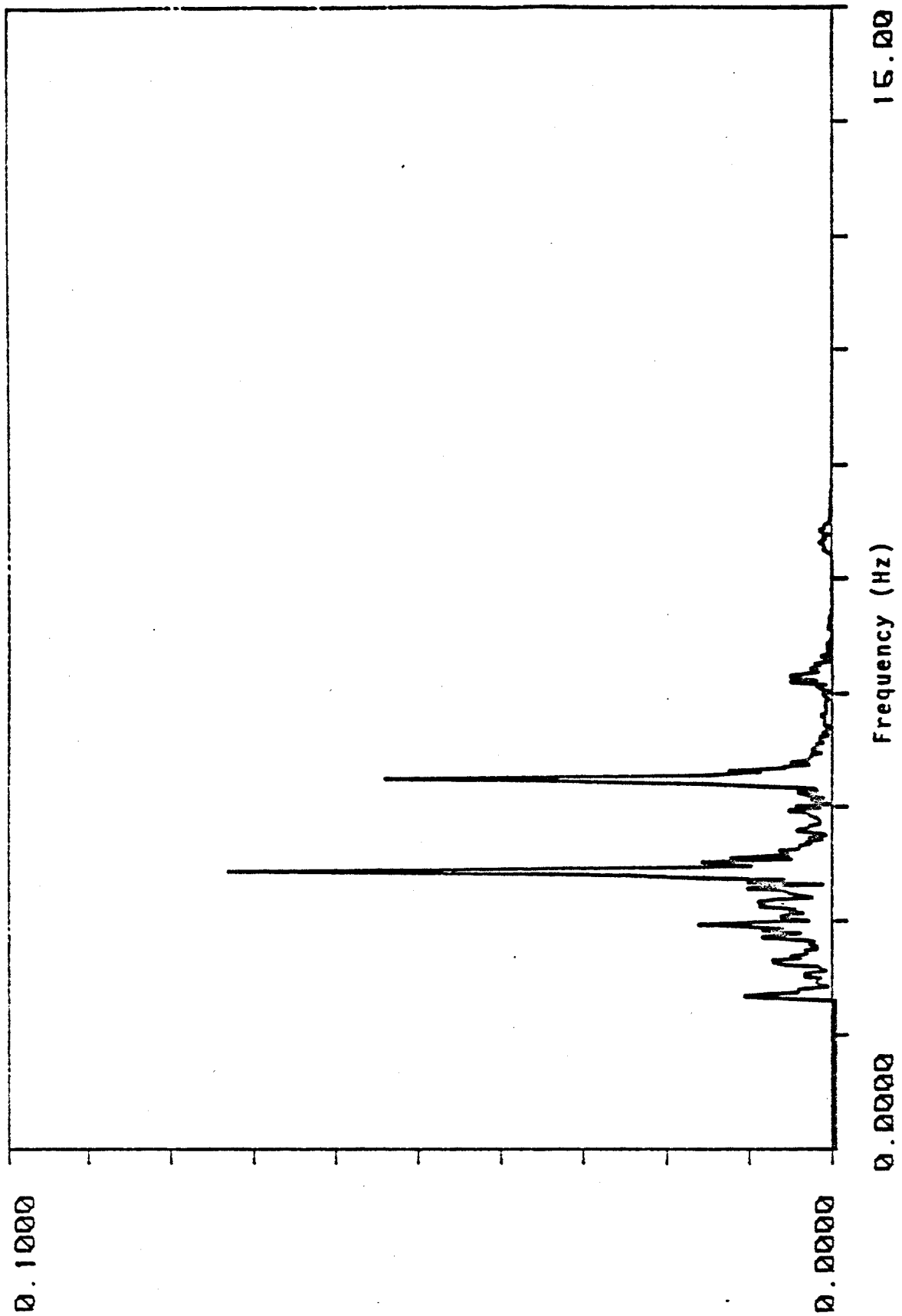
At this point in the analysis, one does not generally know for certain which natural modes of vibration are responding. It will in fact be shown that the in-line response does not always excite a resonant natural frequency.

### 3.6.2 Cylinder Motion at Non-lock-in

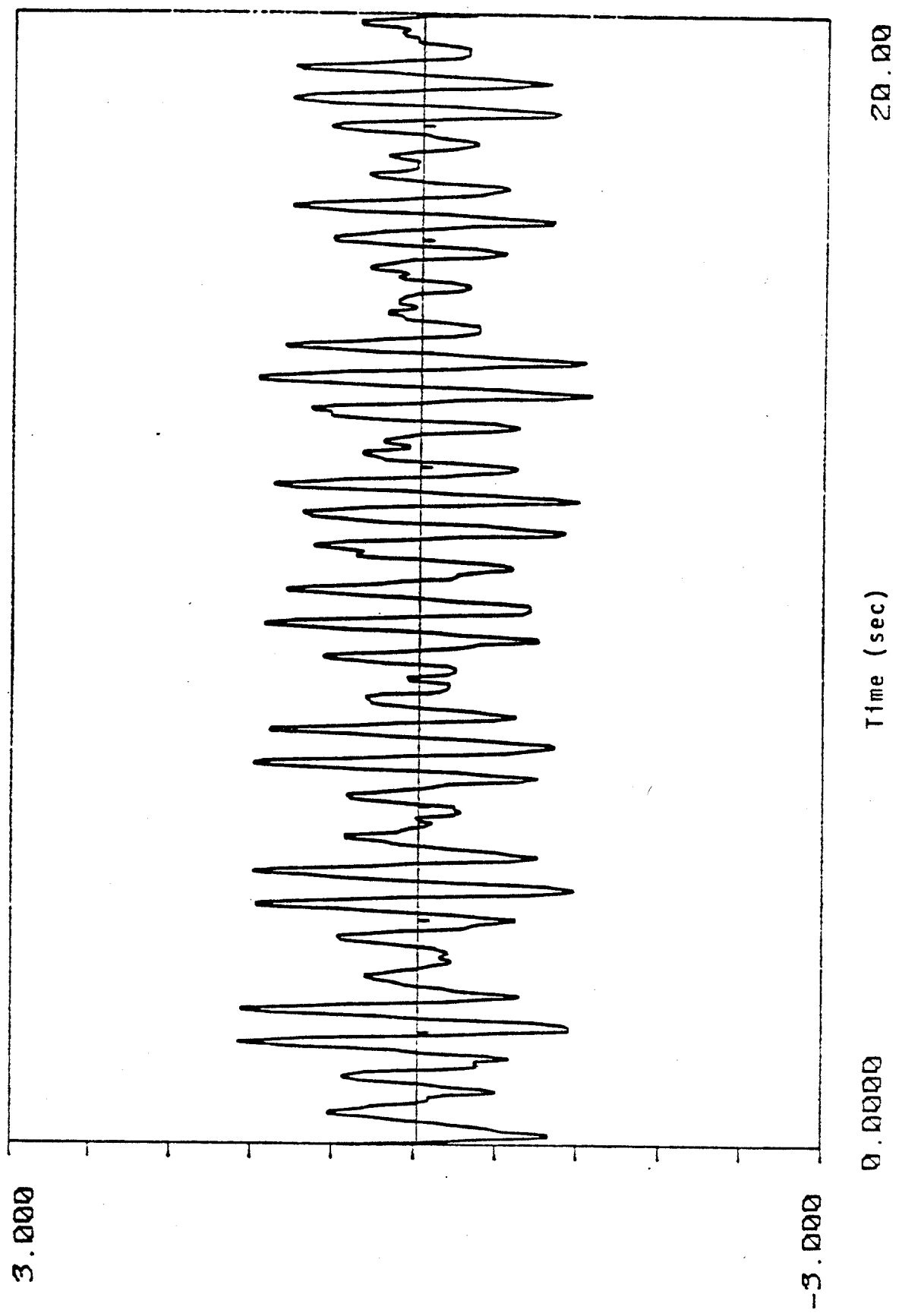
When the vortex shedding frequency is outside of the lock-in range, non-lock-in vibration results. The response is characterized by fluctuations of amplitude and frequency in both in-line and cross-flow directions. The lift force correlation length along the cylinder becomes much shorter than that at lock-in. Figure 3-13 through 3-16 show typical displacement time histories and their magnitude of FFTs in the cross-flow and in-line direction. Wide band lift and drag forces are implied. Figure 3-17 shows the corresponding displacement trajectories. One other important observation in the non-lock-in case is that the in-line response frequencies are equal to the sum of response frequencies in the cross-flow direction. Also the in-line response frequencies do not correspond to any natural frequency of the cylinder. The linear coherence spectrum between in-line and cross-flow responses as shown in Figure 3-18, indicated that they are two linear independent random processes. This result is not surprising



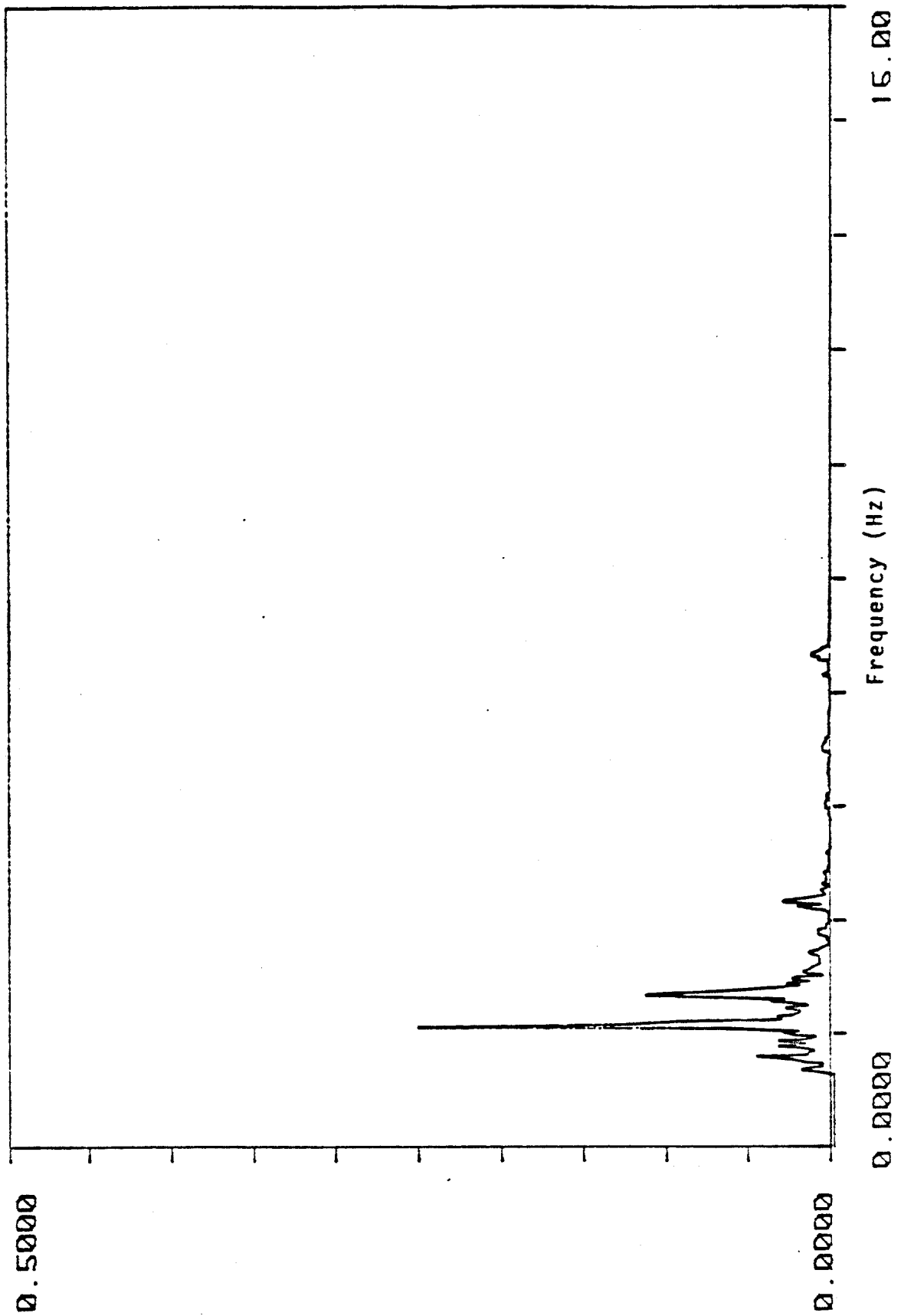
3-13 In-Line Displacement of the Pipe at Non-lock-in at L/8



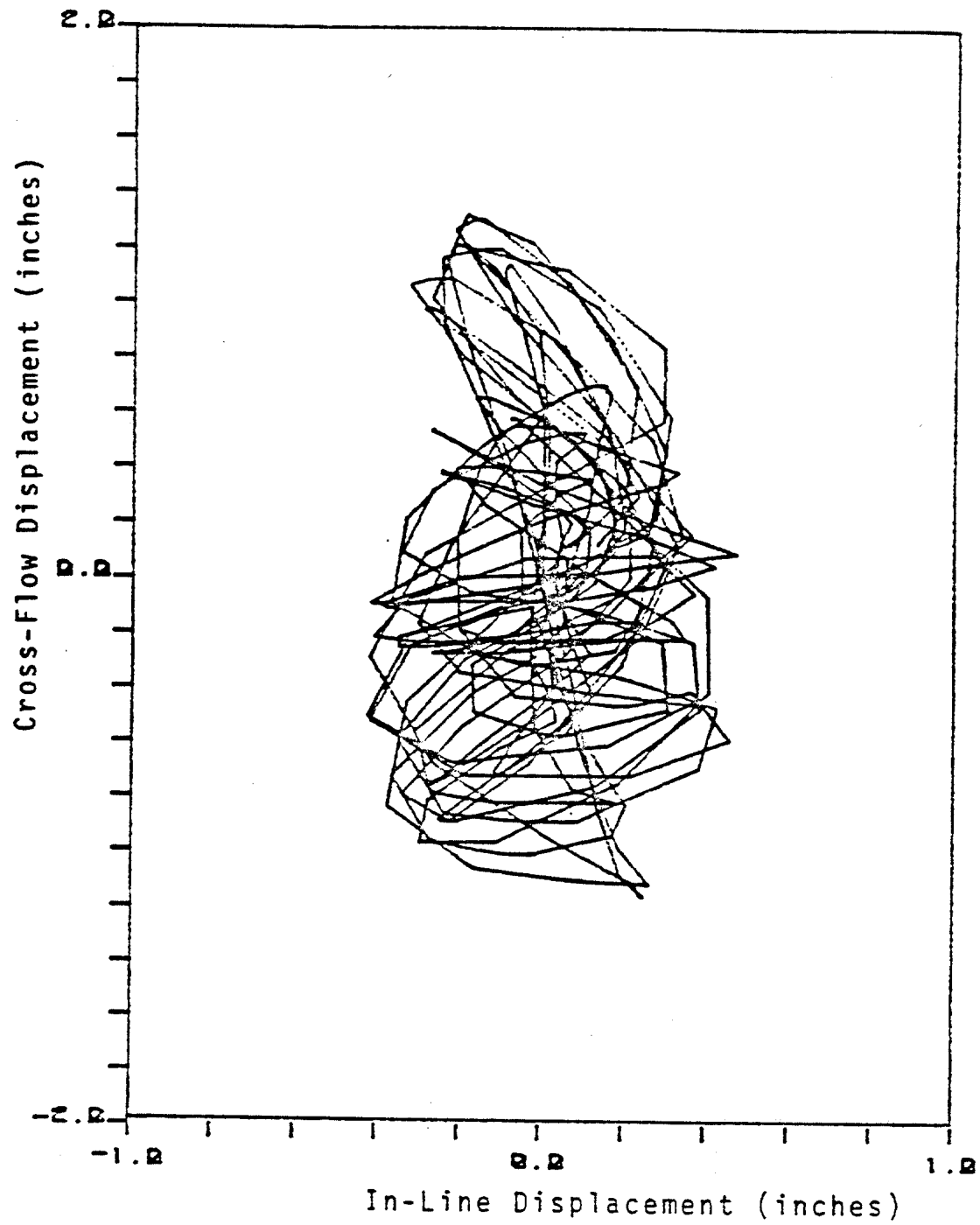
3-14 FFT of the Displacement in Figure 3-13



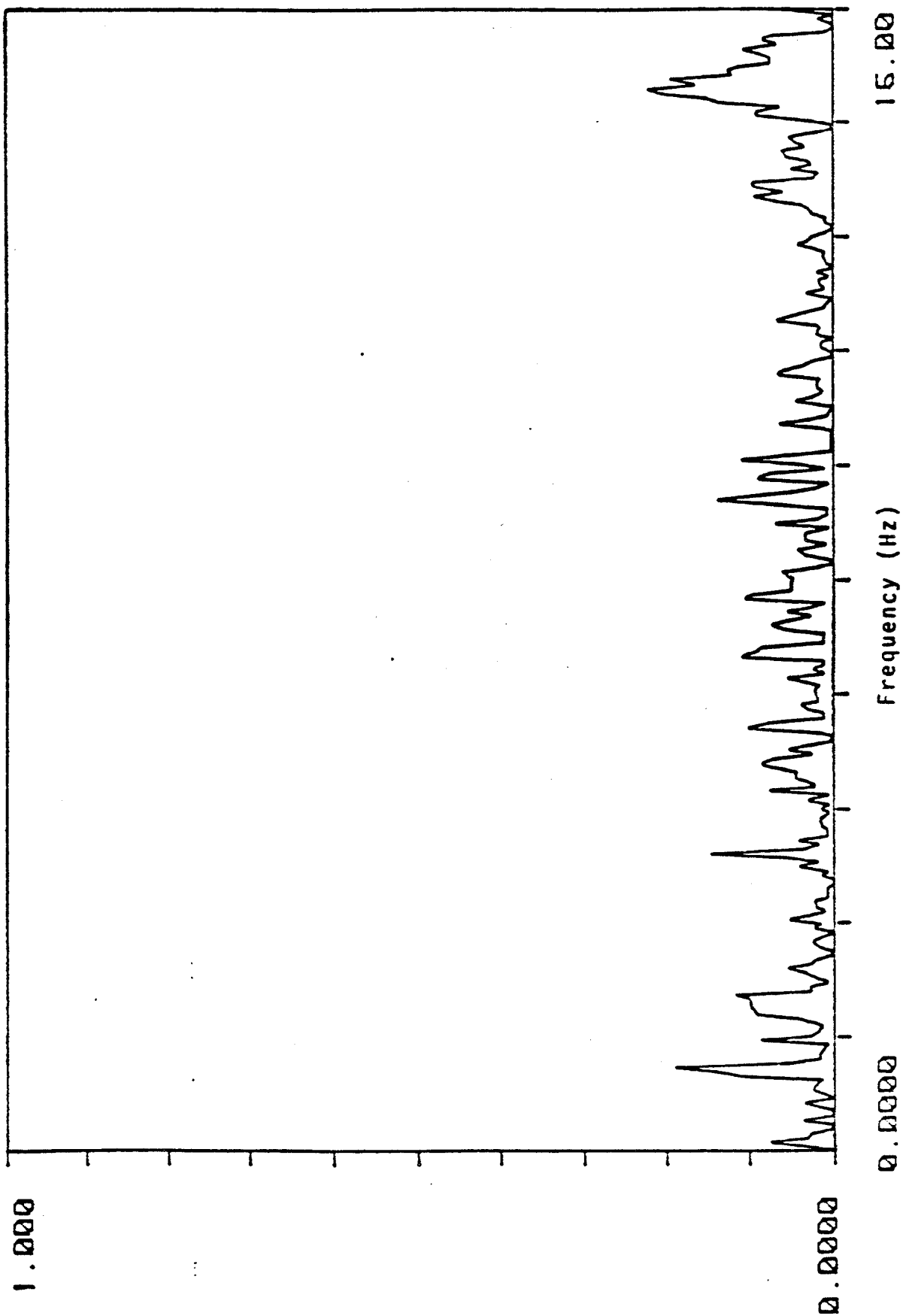
3-15 Cross-Flow Displacement of the Pipe at Non-lock-in at L/8



3-16 FFT of the Displacement in Figure 3-15



3-17 Two-Dimensional Motion Time History at Non-lock-in at  $L/8$   
(Figure 3-15 vs. 3-13)



3-18 Linear Cross-Coherence Between In-Line and Cross-Flow  
Responses at Non-lock-in



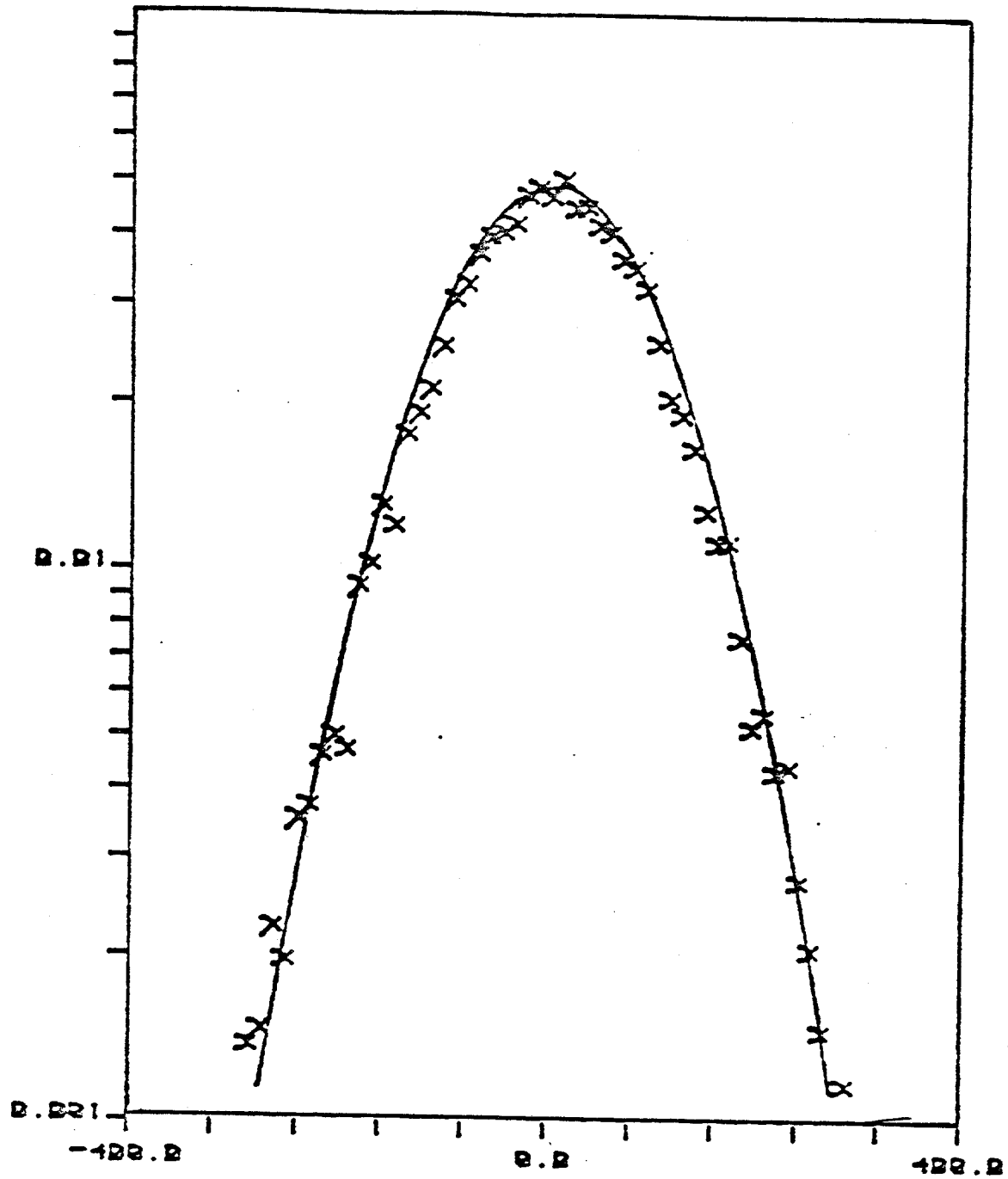
because the response frequencies in these two directions are totally different.

The frequency doubling and summing phenomena for both lock-in and non-lock-in cases raise the question of whether the responses in the in-line and cross-flow directions are independent or not. If they are not independent, then the task becomes how to prove they are related and what kind of relationship it is.

Finally, the probability distribution at non-lock-in case was examined. Figure 3-19 shows the histogram of the cross-flow response for the non-lock-in case. There appears to be no significant departure of the histogram from a Gaussian distribution. A Chi-square goodness of fit test with a 5% significance level was performed on the histogram from which we concluded that the non-lock-in cross-flow response can be approximated by a Gaussian random process. This result is very important for latter analysis.

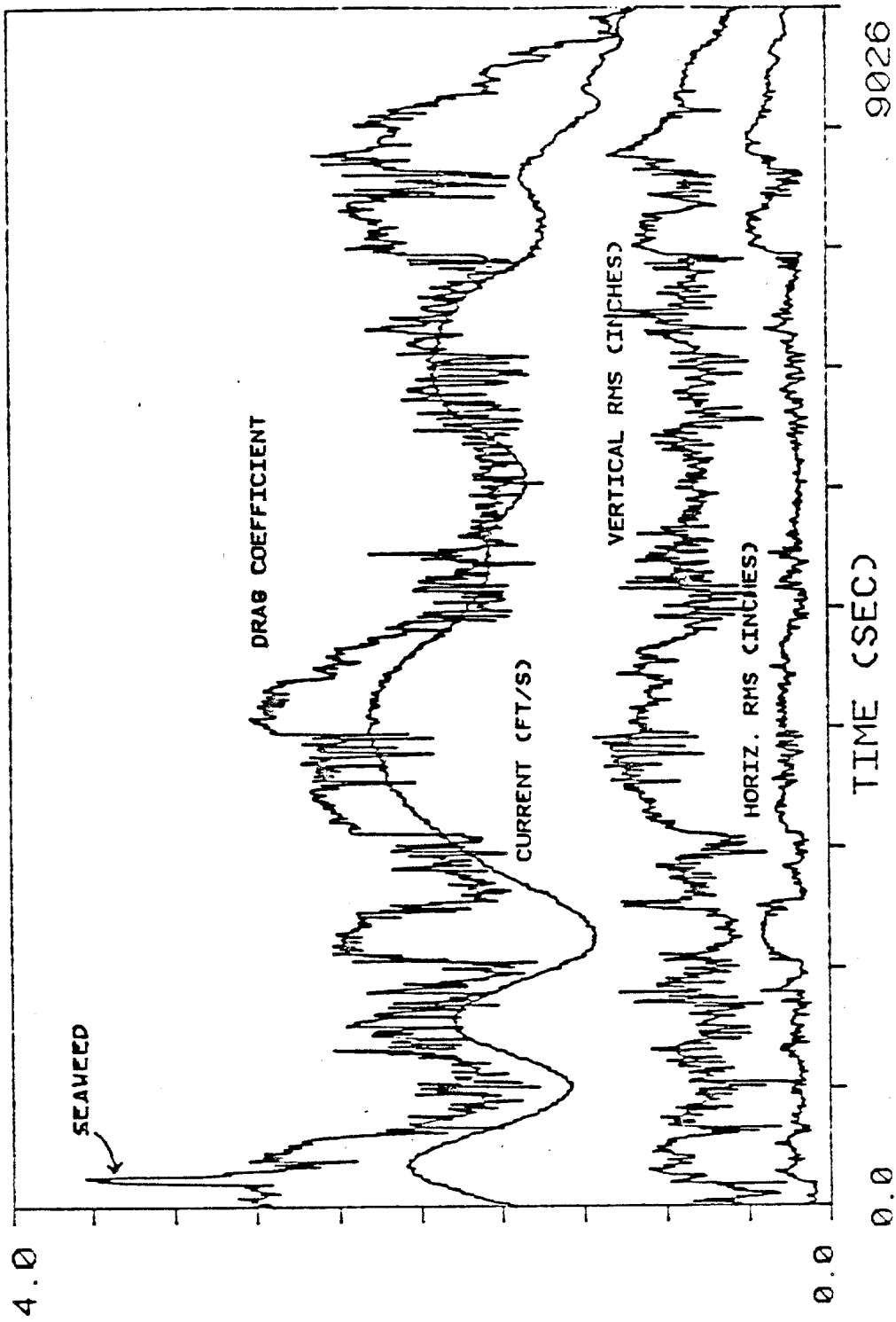
### 3.7 Current, Drag Coefficient and RMS Displacement

the RMS data for in-line and cross-flow displacements for complete 2 1/2-hour data acquisition cycles were calculated for the pipe, bare cable, faired cable and a cable with lumped masses. The RMS data were calculated by a moving average whose window was 8.53 seconds in length.

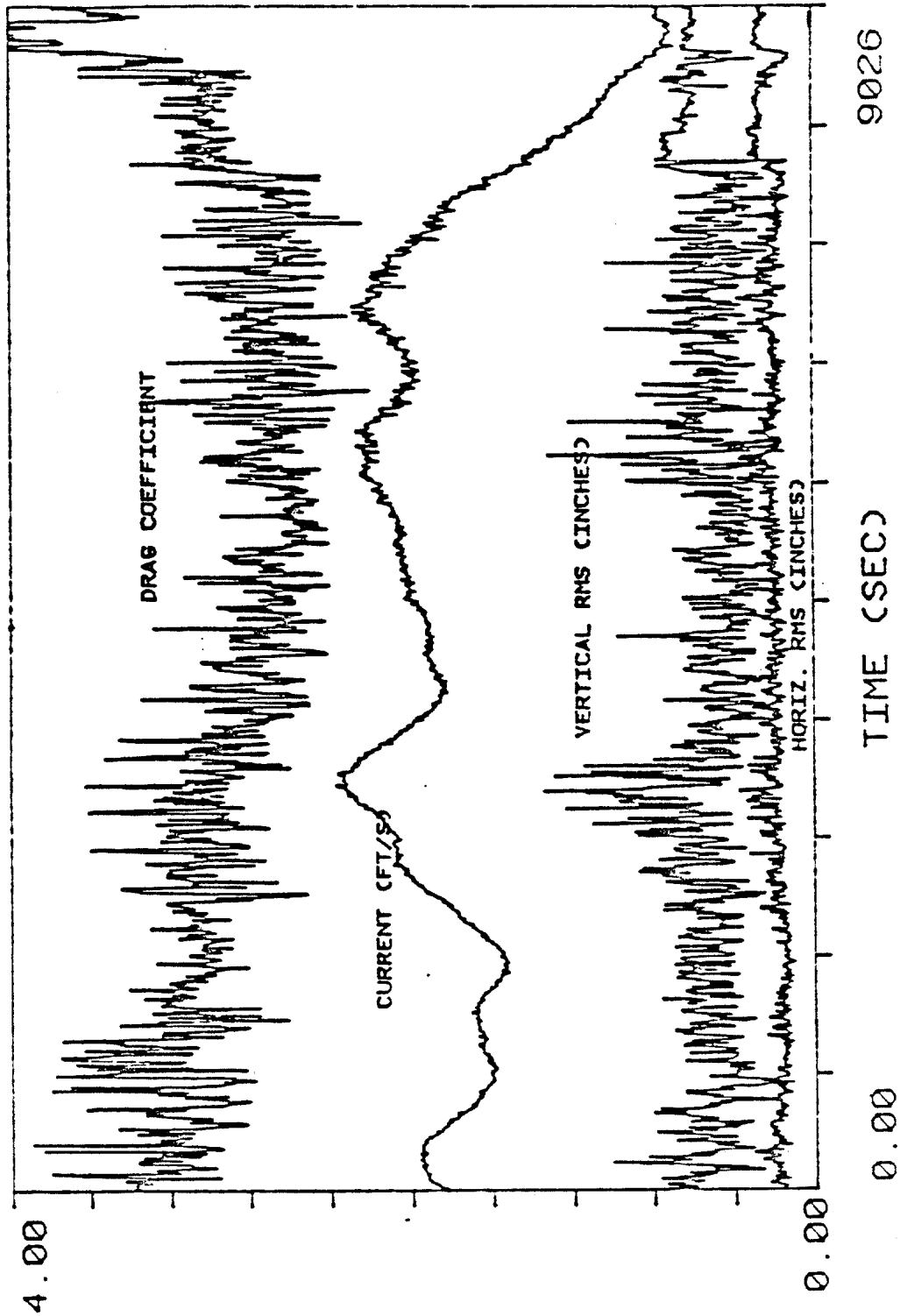


3-19 Cross-Flow Response Histogram at Non-lock-in

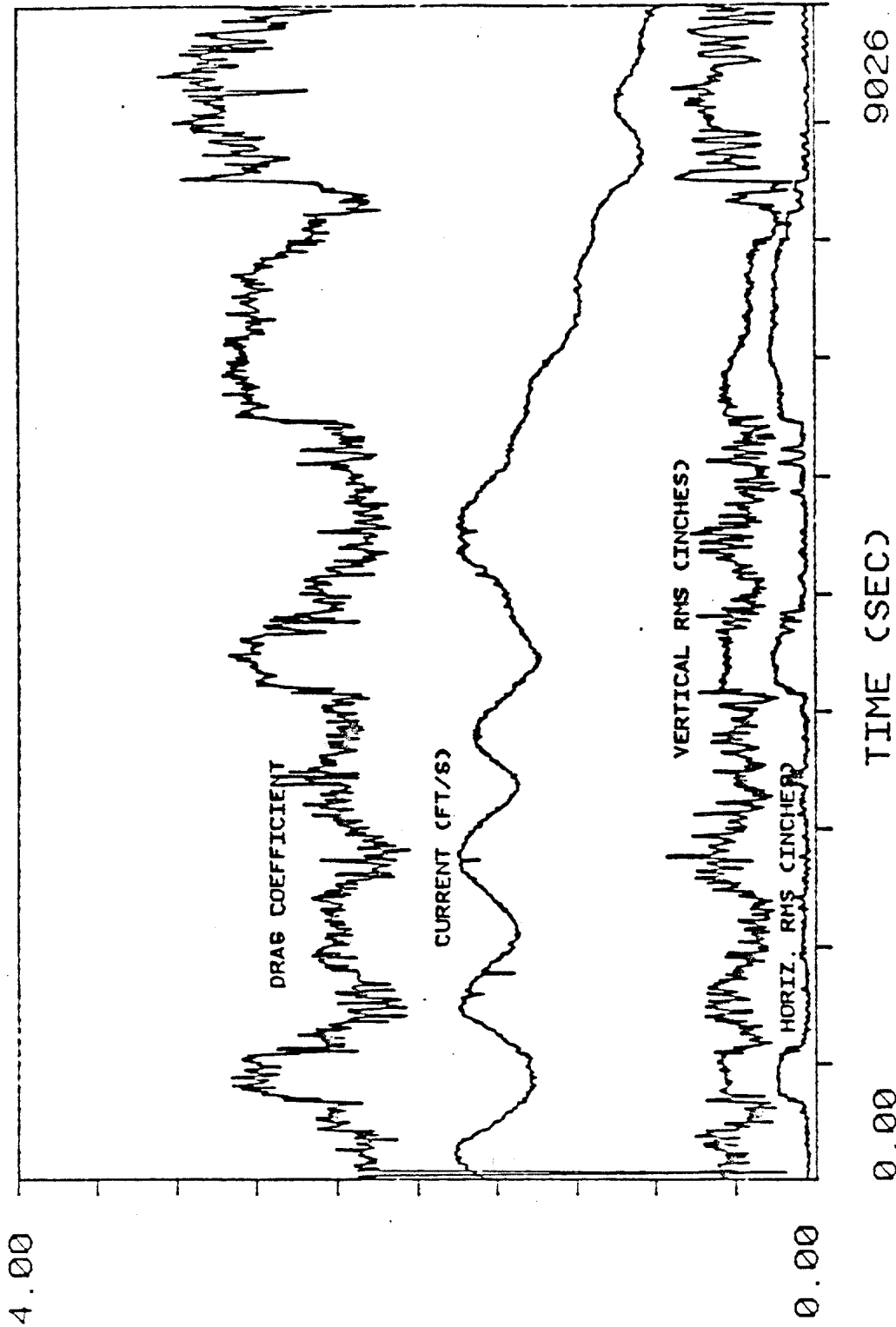
These results are presented in figure 3-20 to 3-23, along with linear moving average values of drag coefficient and current speed. The displacement data are taken from location  $1/6 L$  for the pipe and the bare cable, from location  $3/4 L$  for the cable with lumps and from location  $2/5 L$  for the faired cable. Over the  $2\frac{1}{2}$ -hour test, some periods correspond to lock-in responses, and others to non-lock-in responses. As current speed falls within a lock-in range, a substantial increase of cross-flow and/or in-line RMS displacement is observed. A corresponding elevated plateau in the drag coefficient is also observed. These are raw RMS displacements at the specified location and have not been corrected for mode shape. Due to the fact that these raw data are highly positional or modal dependent, the in-line and cross-flow RMS displacements in these figures do not give a good indication of any relation existing between these two direction's responses. In the next chapter, modal analysis is used to represent the behavior of the entire cylinder in order to provide a better indication of any possibly existing relation between in-line and cross-flow responses.



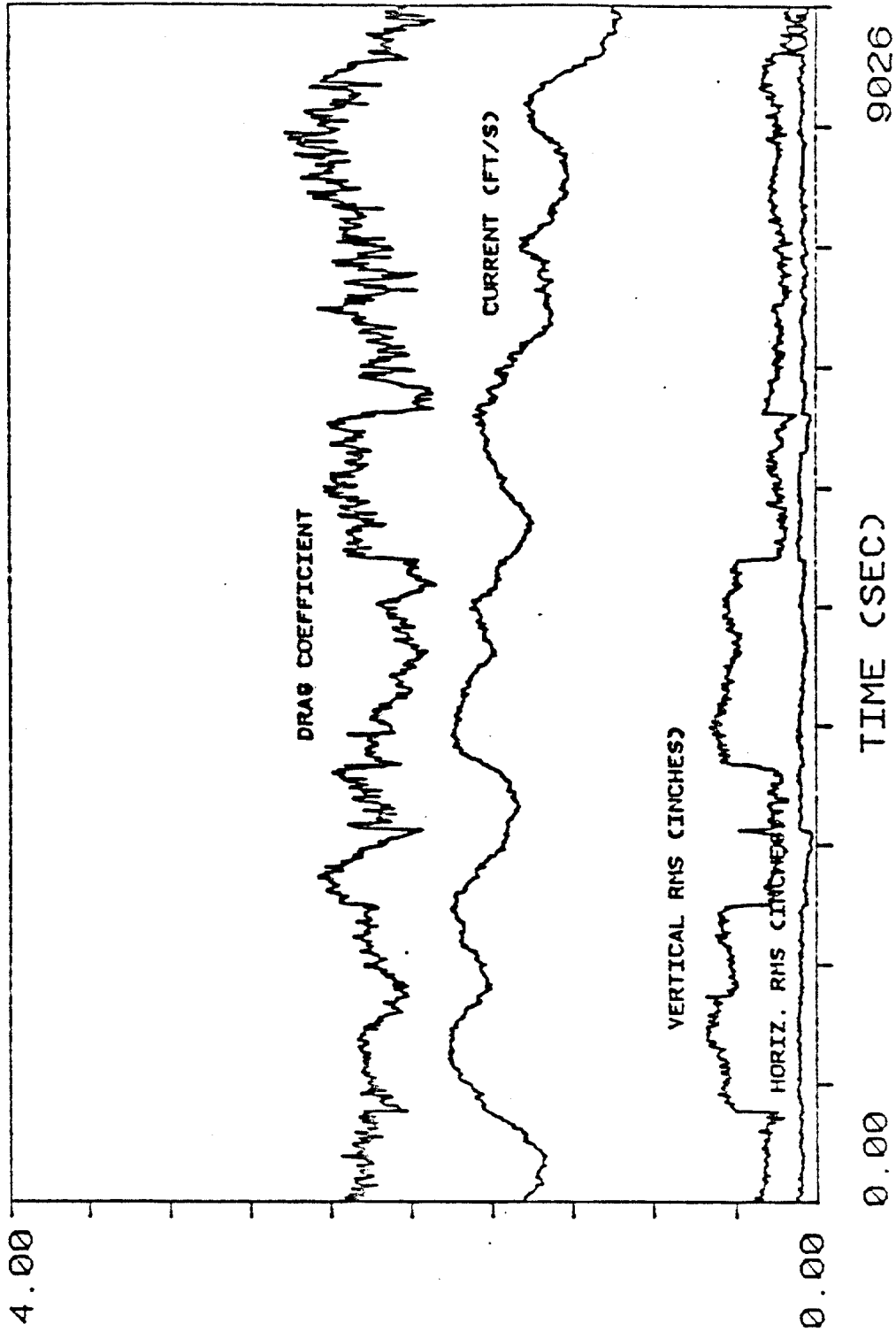
3-20 2 1/2-Hour Record of the Displacement, Current, and Drag  
Coefficient for the Pipe at L/8



3-21 2 1/2-Hour Record of the Displacement, Current, and Drag  
Coefficient for the Bare Cable at L/6



3-22 2 1/2-Hour Record of the Displacement, Current, and Drag  
Coefficient for the Cable With 2 Light (L/6, L/2) and  
4 Heavy (L/3, 5L/8, 3L/4, 7L/8) Lumped Masses at 3/4L



3-23 2 1/2-Hour Record of the Displacement, Current, and Drag  
Coefficient for the Paired Cable at 2L/5

## CHAPTER 4

### MODAL ANALYSIS

In the last chapter, it was stated that there exist frequency doubling and summing phenomena for both lock-in and non-lock-in cases, from which we expect that the in-line and cross-flow responses should not be totally independent in spite of the fact that they are linearly independent, as indicated by the linear coherence spectrum. In this chapter, a least squares error minimization method is used to estimate the natural coordinates of all the participating modes. Total vibration energies in both directions are then calculated from the natural coordinates and the known mode shapes. If in-line and cross-flow responses are indeed related, the vibration energies, which represent the behavior of the entire cylinder, should be able to provide evidence of the existence of a relationship between in-line and cross-flow directions.

#### 4.1 Modal Analysis of a Uniform String

The response of a cylinder under external load can be described conveniently by using modal analysis. The method is intended to express the response as a superposition of the system's eigenfunctions multiplied by their corresponding time-dependent natural coordinates. As an illustration of this method, consider a uniform string under



tensile load with pinned end boundary conditions. The equation of motion for this boundary problem is:

$$T \ddot{y}(x,t) - R(x) \dot{y}(x,t) + f(x,t) = m(x) \ddot{y}(x,t) \quad (4.1.1)$$

The response  $y(x,t)$  may be expressed as a superposition of normal modal responses.

$$y(x,t) = \sum_{r=1}^{\infty} Y_r(x) P_r(t) \quad (4.1.2)$$

where  $Y_r(x)$  is the normalized mode shape and has the following orthogonality property.

$$\int_0^L m(x) Y_r(x) Y_s(x) dx = \delta_{rs} \quad (4.1.3)$$

Substitution of (4.1.2) into (4.1.1) multiplication by  $Y_s(x)$ , and integration from  $x=0$  to  $L$  leads to:

$$P_r(t) + \dot{P}_r(t) \int_0^L R(x) Y_r(x) Y_r(x) dx + W_r^2 P_r(t) = N_r(t) \quad (4.1.4)$$

If  $R(x)$  is proportional to  $m(x)$ , orthogonality of normal modes leads to a set of uncoupled single degree of freedom oscillation equations in terms of the natural coordinates  $P_r(t)$ .

$$\text{For } R(x) = C m(x) \quad (4.1.5)$$

$$\ddot{P}_r(t) + C \dot{P}_r(t) + W_r^2 P_r(t) = N_r(t) \quad (4.1.6)$$

where  $N_r(t)$  the modal force is defined as:

$$N_r(t) = \int_0^L Y_r(x) f(x,t) dx \quad (4.1.7)$$

In reality, the damping may not be governed by equation (4.1.5). However, for lightly damped well separated modes, the uncoupled normal mode equations may be derived for a beam under tension, with pinned end conditions. For a uniform beam the mode shapes are sinusoids as they are for a uniform string. By using modal analysis, the continuous system is reduced to many single degree of freedom systems. In the next section we will estimate the natural coordinate time histories,  $P_r(t)$ , from measured responses at the accelerometer locations.

#### 4.2 Estimation of Natural Coordinates

In the preceding section, the response of the cylinder was expressed in terms of a superposition of mode shapes  $Y_r(x)$  multiplied by the natural coordinates  $P_r(t)$ :

$$y(x,t) = \sum_{r=1}^{\infty} P_r(t) Y_r(x) \quad (4.2.1)$$

In this experiment, the response was measured at seven positions. They are at  $L/8$ ,  $L/6$ ,  $L/4$ ,  $2/5L$ ,  $L/2$ ,  $5/8L$ ,  $3/4L$ . In this study, a least squares method was used to estimate the natural coordinates in terms of the measured responses at these seven positions. For any test case the

response is dominated by a finite number of modes usually 2 to 6 in number. A first guess at the responding modes may be obtained by inspection of the response spectrum at any one location. By summing the normal mode responses over the apparent participating modes, the following equations are obtained, where the range  $M-N$  covers all of the participating modes. The mode shapes can be calculated theoretically. For the pin-supported uniform cylinder, the mode shapes are given by

$$Y_r(X) = \sin(r X/L)$$

At time  $t=t_0$ , the response of position  $X=X_j$  can be expressed as:

$$y(x_j, t_0) = \sum_{i=m}^N P_i(t_0) Y_i(x_j) + E(x_j) \quad (4.2.2)$$

Where  $E(X_j)$  is the error term.

Rewriting (4.2.2) in matrix form

$$\{y\} = [Y] \{P\} + \{E\} \quad (4.2.3)$$

where  $y_j$  is the vector of the measured response

$Y_{ij}$  is the mode shape matrix

$P_i$  is the vector of natural coordinate

$E_j$  is the vector of error

$$i=m, N \quad j=1, 7$$

The sum of error squares  $ee$  is given by

$$ee = \langle E \rangle \{E\} = \{ \{y\} - [Y] \{P\} \}^T \{ \{y\} - [Y] \{P\} \} \quad (4.2.4)$$

$$= \{y\}^T \{y\} - 2 \{P\}^T [Y]^T \{y\} + \{P\}^T [Y]^T [Y] \{P\}$$

The vector of natural coordinates  $P_i$  is to be determined such that the error squared term is minimized.

$$\min[ee] = \min[\{E\}^T \{E\}]$$

Let

$$\frac{d}{dP_i}(ee) = 0 \quad (4.2.5)$$

and solve for  $P(t)$

$$\{P\} = [[Y]^T [Y]]^{-1} [Y]^T \{y\} \quad (4.2.6)$$

or

$$\{P\} = [T] \{y\} \quad (4.2.7)$$

where  $[T]$  is the transfer matrix:

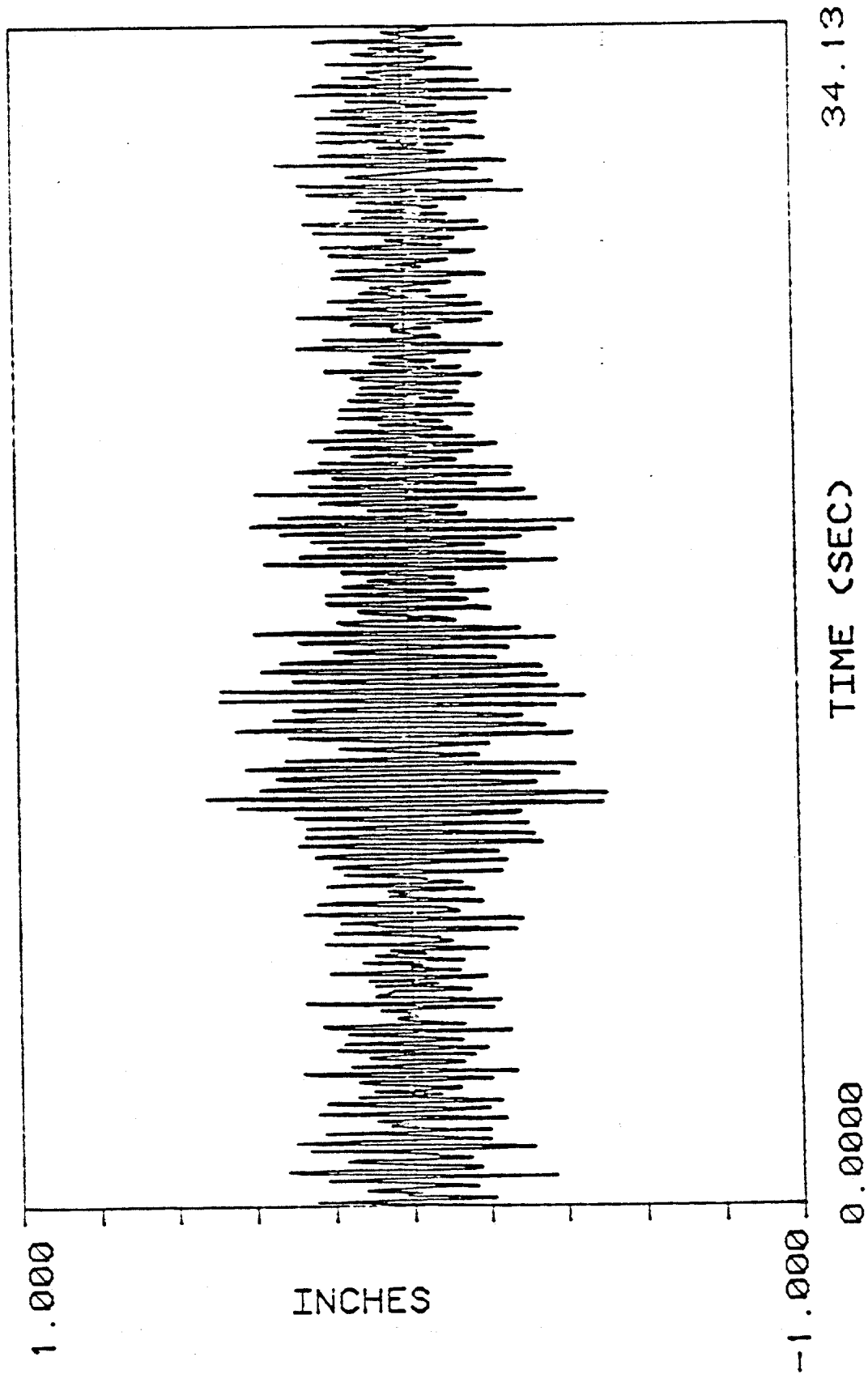
$$[T] = [[Y]^T [Y]]^{-1} [Y] \quad (4.2.8)$$

Equation (4.2.7), decomposes the measured response at the seven positions into the natural coordinates provided the mode shapes are known and the guess of the responding modes is initially correct. Figure 4-1 shows an example of the horizontal pipe vibration displacement at position  $L/8$ . It is clear that several modes were excited. In the

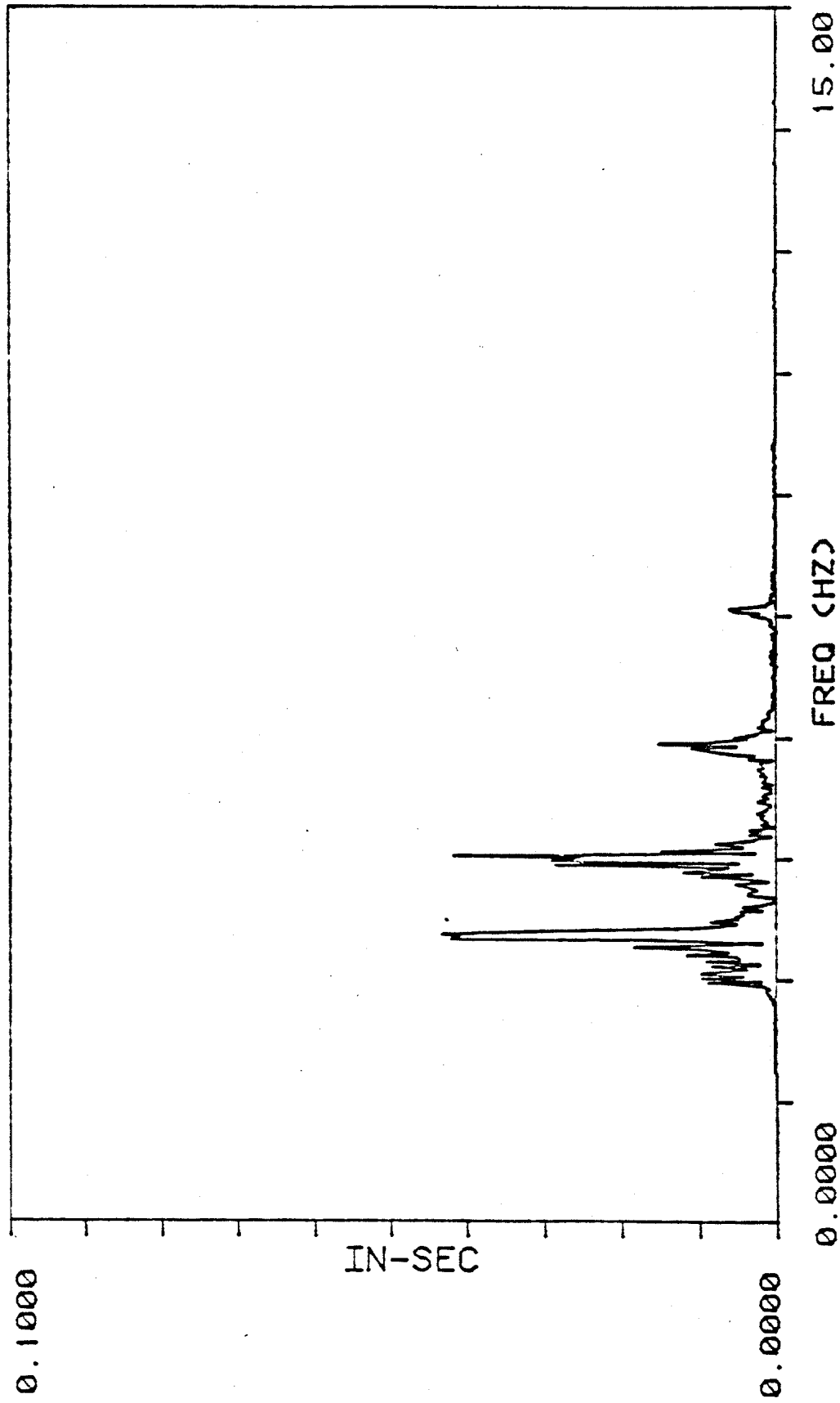
displacement spectrum, there are several peaks, each corresponding to one particular mode to be identified. Using the method discussed above, the natural coordinate time histories were obtained for the 4th, 5th, 6th and 7th modes corresponding to each peak in the displacement spectrum, shown in figure 4-2. These natural coordinate time histories are shown in figure 4-3. The FFT of fourth- and fifth-mode natural coordinates are shown in figure 4-4 and 4-5. Each natural coordinate time history represents the antinode displacement for that mode. their sum does not equal the displacement portrayed in figure 4-1 because it is the motion at a specific point on the cable. Their sum correctly weighted by the value of the respective mode shapes at that location would equal the displacement shown in Figure 4-1.

#### 4.3 Vibration Energy

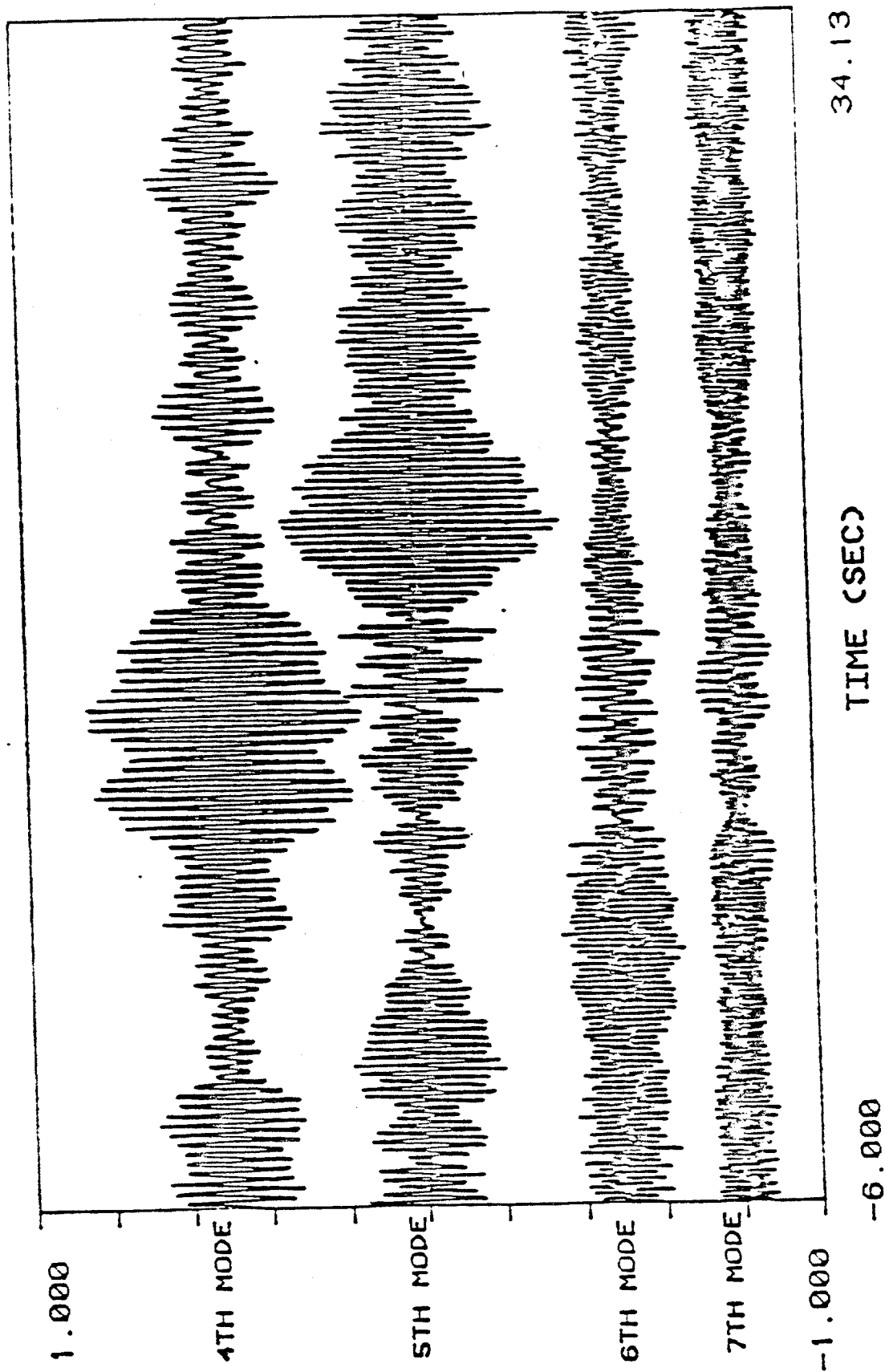
Lock-in responses can be analyzed with deterministic models, unlike non-lock-in random responses. At constant current speed when the cylinder is at non-lock-in, the participation of different contributing modes varies with time. An example of this phenomenon spanning a short period of time is presented in figure 4-3 obtained from the modal analysis. It is enlightening to study non-lock-in response on a longer time scale. A 448-second record of non-lock-in



4-1 In-Line Displacement at Non-lock-in at L/8  
With 4th, 5th, 6th, and 7th Modes Responding

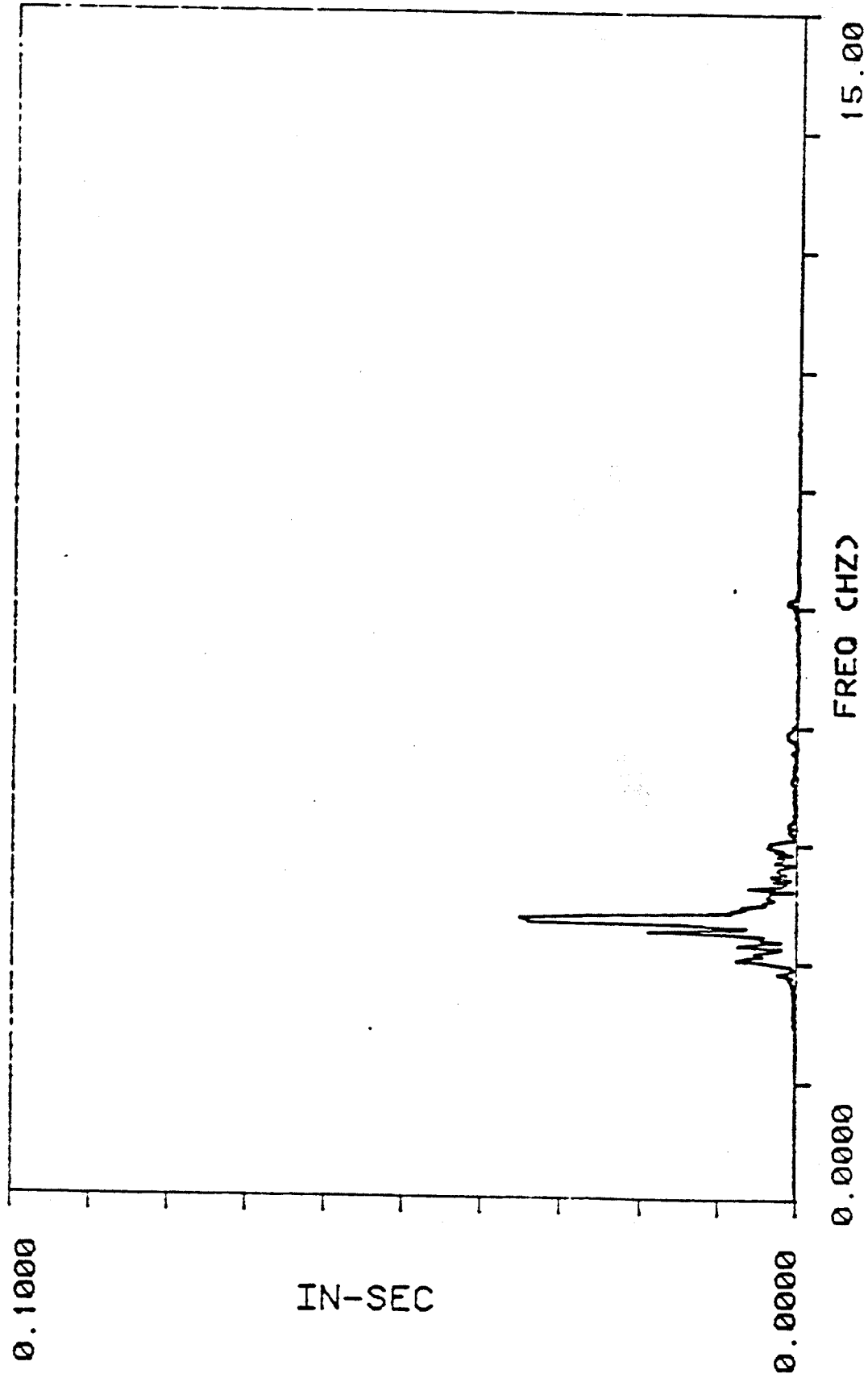


4-2 FFT of the Displacement in Figure 4-1

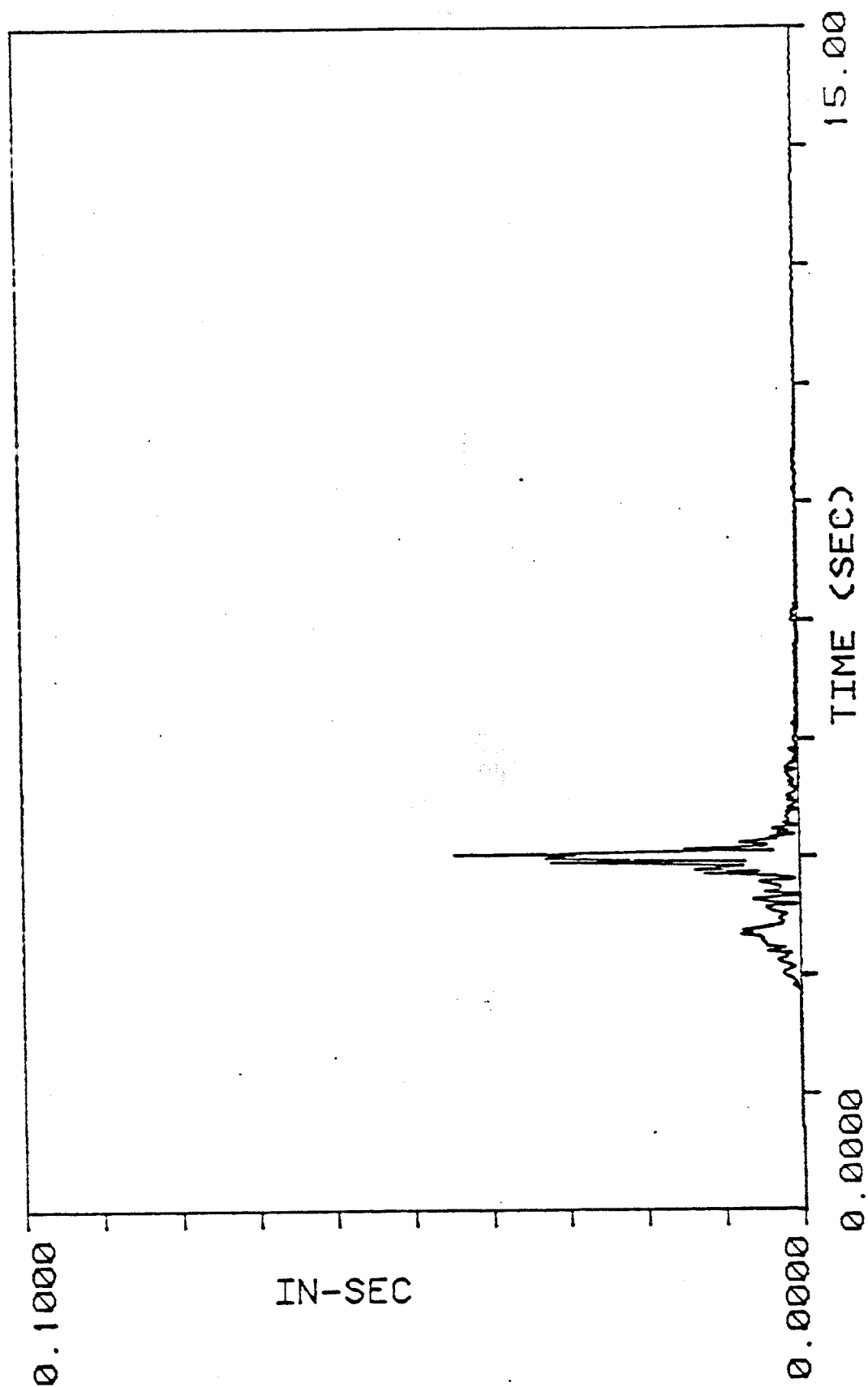


4-3 Natural Coordinate Time Histories for the 4th, 5th, 6th  
and 7th Modes of the Pipe

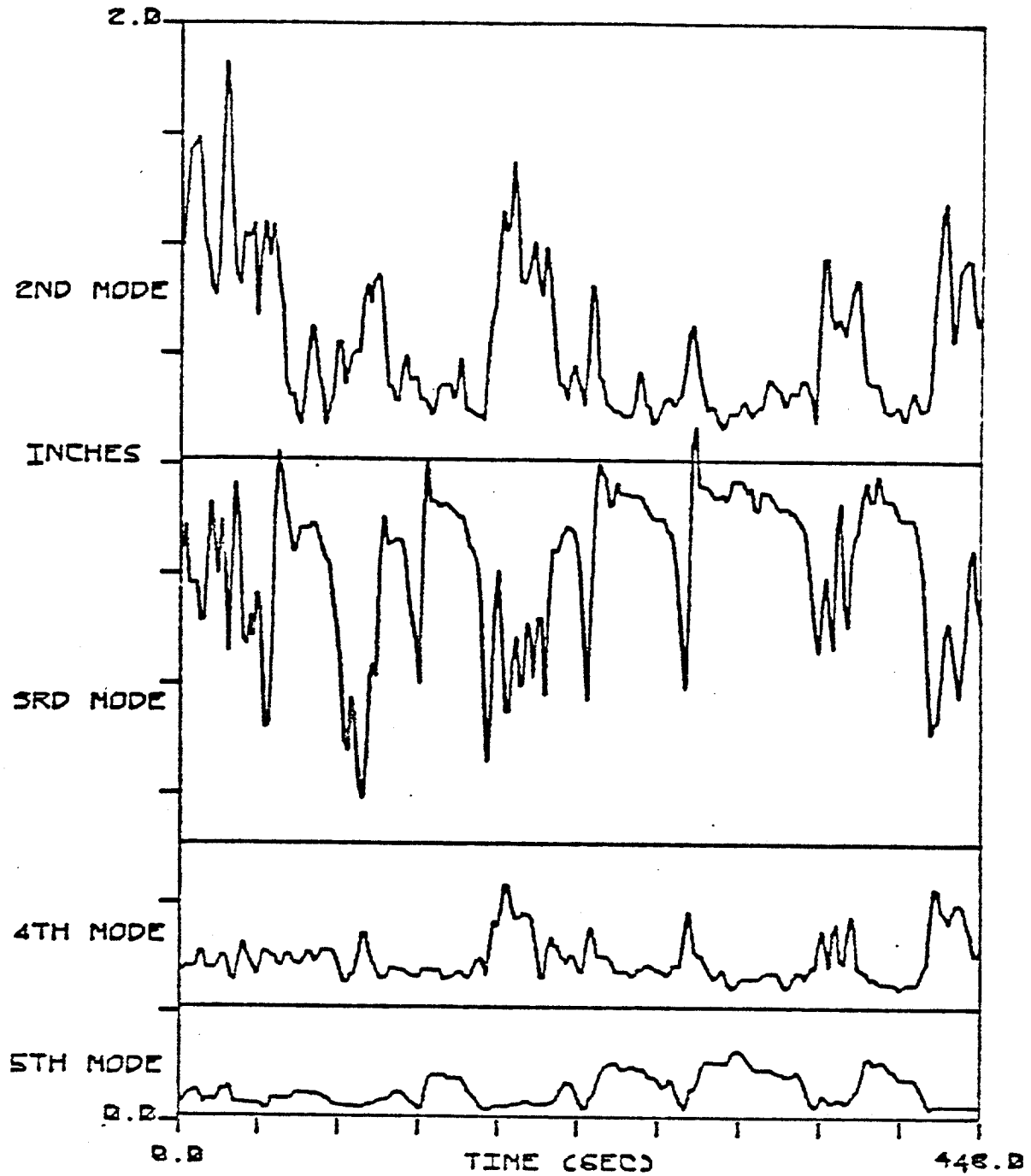




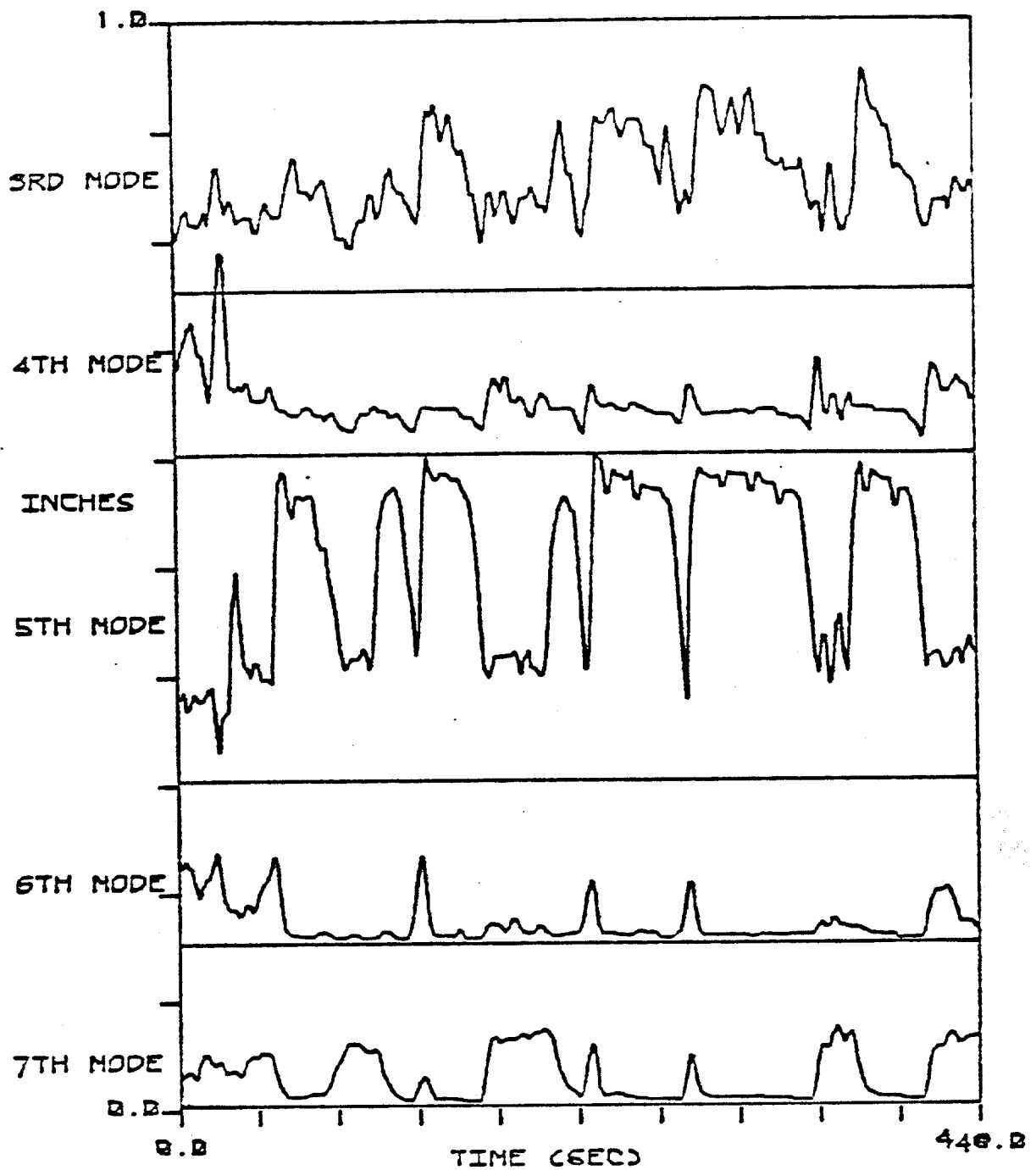
4-4 FFT of the 4th Natural Coordinate Time History



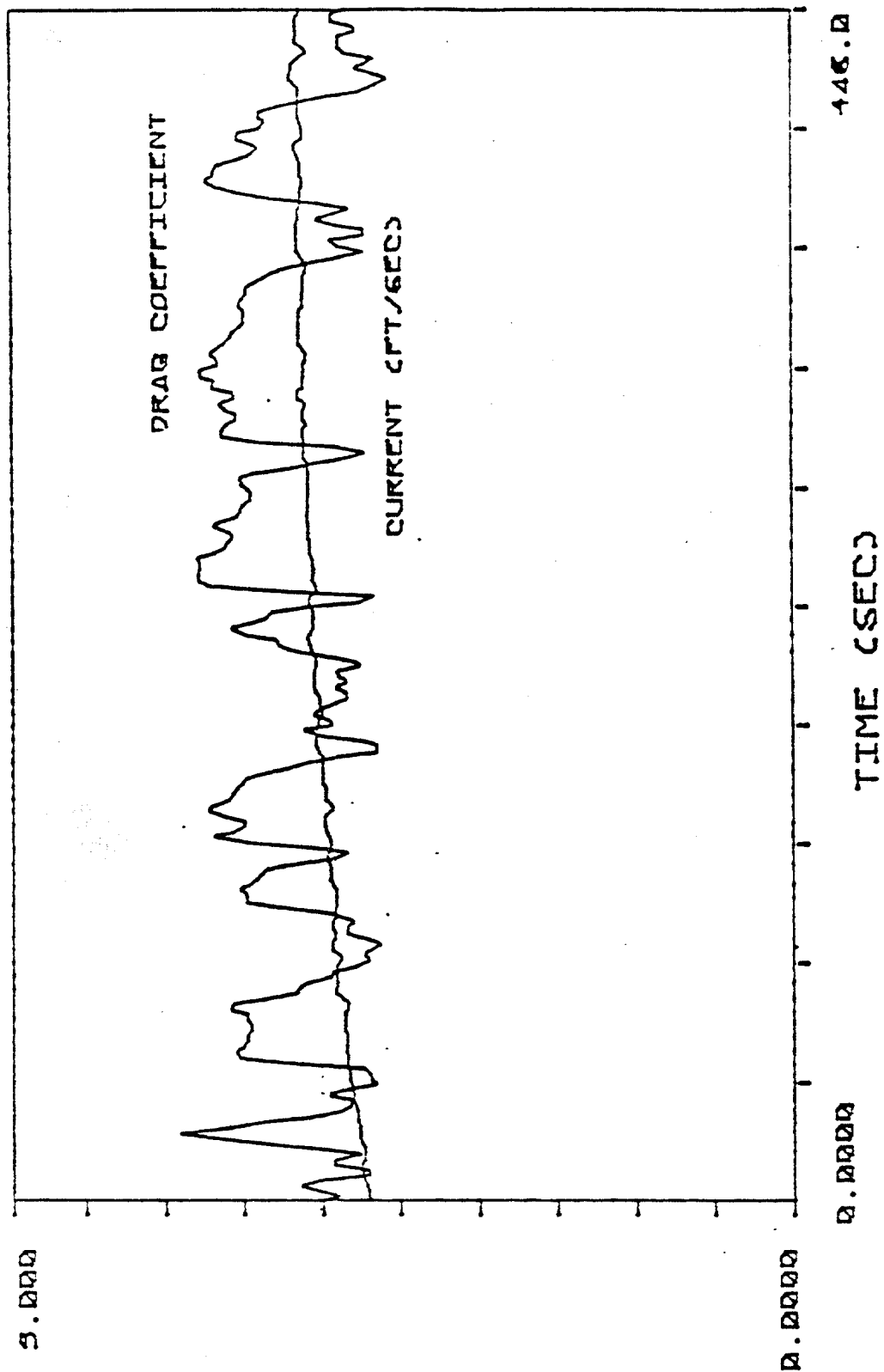
4-5 FFT of the 5th Natural Coordinate Time History



4-6 RMS of the Natural Coordinates for the 2nd, 3rd, 4th and 5th Cross-Flow Modes of the Pipe



4-7 RMS of the Natural Coordinates for the 3rd, 4th, 5th, 6th and 7th In-Line Modes of the Pipe



4-8 Drag Coefficient and Current Corresponding to Figure  
4-6 and 4-7

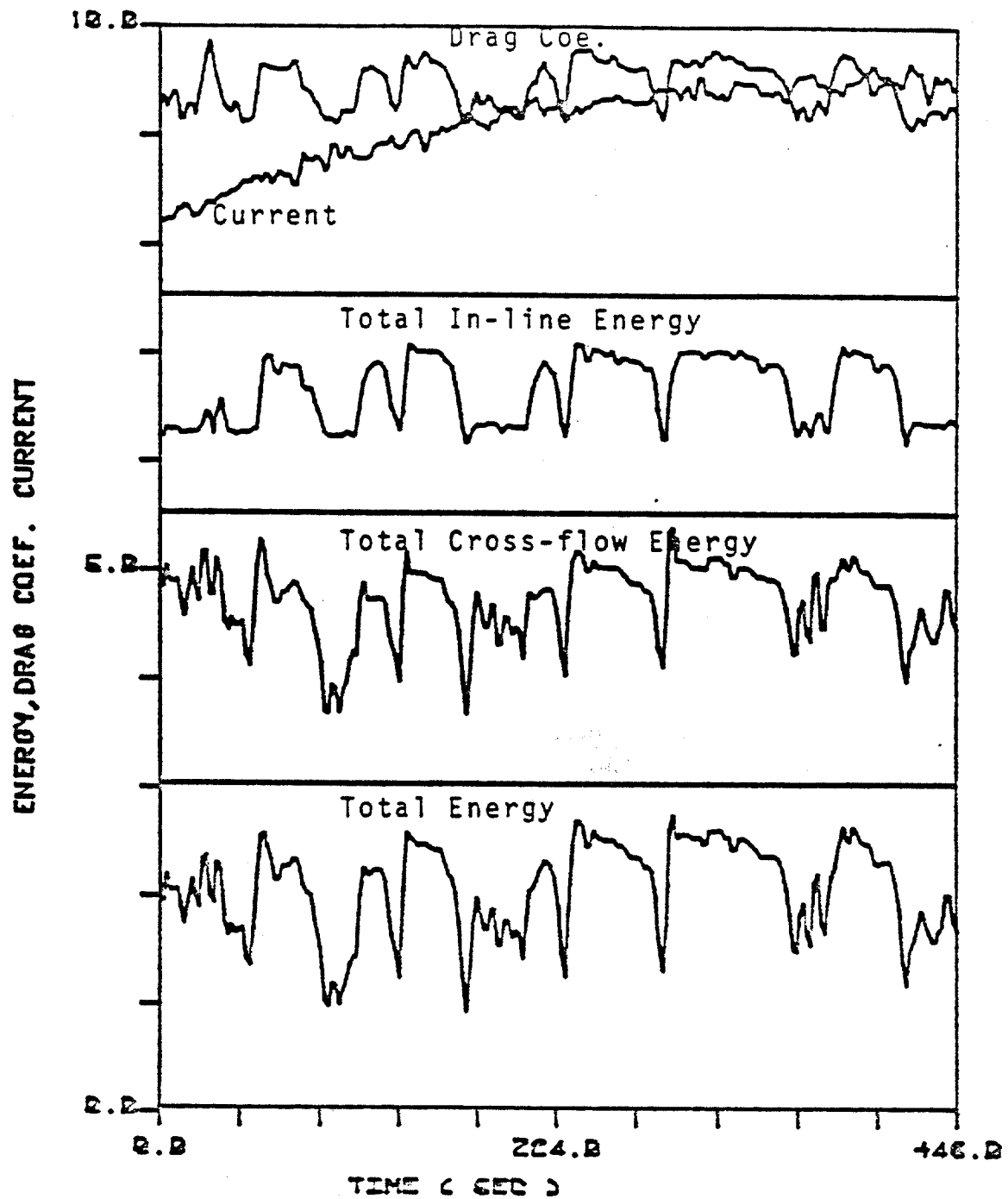
pipe response was analyzed and the contributing modal responses were separated by the modal analysis. Moving average RMS natural coordinate responses in both directions were calculated. These are plotted in figure 4-6 and 4-7. These responses reflect the RMS values of the individual modal anti-node response. Notice that as the response of one mode recedes, another appears to take its place. The current and drag coefficient for the same time interval is shown in figure 4-8.

Moving average vibration energies were calculated from these natural coordinates and mode shapes in both in-line and cross-flow directions as shown in figure 4-9. The vibration energy is given by

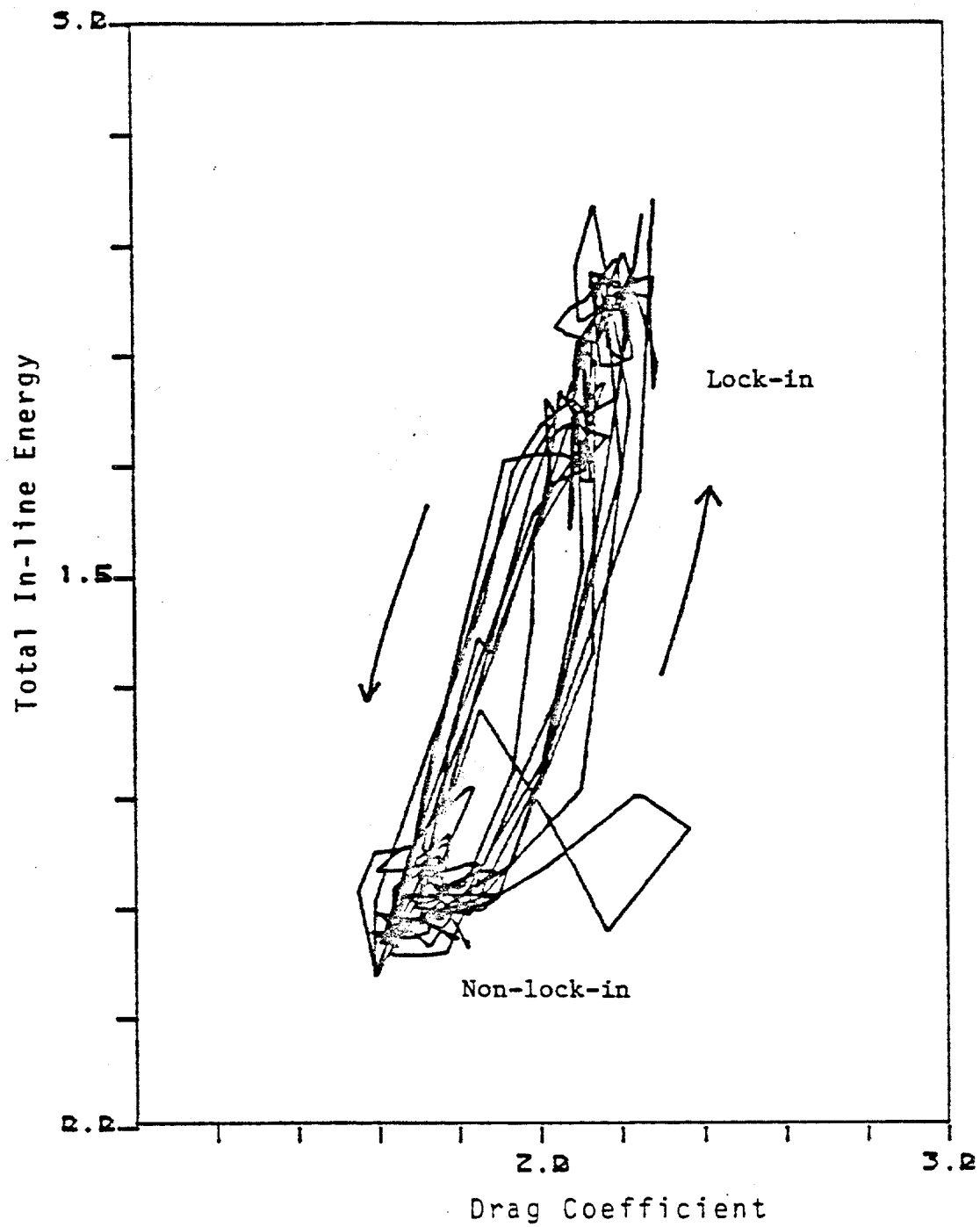
$$E(t) = L/4 \sum_r \{ EI \Pr^2(t) (n_\pi / L)^4 + T \Pr^2(t) (n_\pi / L)^2 + m \Pr^2(t) \}$$

Relationships between in-line and cross-flow vibration energy were observed which implied that in-line and cross-flow responses shouldn't be independent of each other in spite of their linear independence. We then expected the relationship must be nonlinear.

The drag coefficient is also related to the vibration energy as shown in figure 4-9. The scatter diagram between drag coefficient and in-line vibration energy in figure 4-10 shows an interesting result. From lock-in to non-lock-in



4-9 Drag Coefficient, Current, Total In-Line and Cross-Flow Vibration Energy, and Total Energy of the Pipe



4-10 Scatter Diagram of Drag Coefficient vs. Total In-Line Vibration Energy in Figure 4-9



case, the path of the change is different from that of the non-lock-in to lock-in case. This history dependent property has been observed by several other investigators [24].

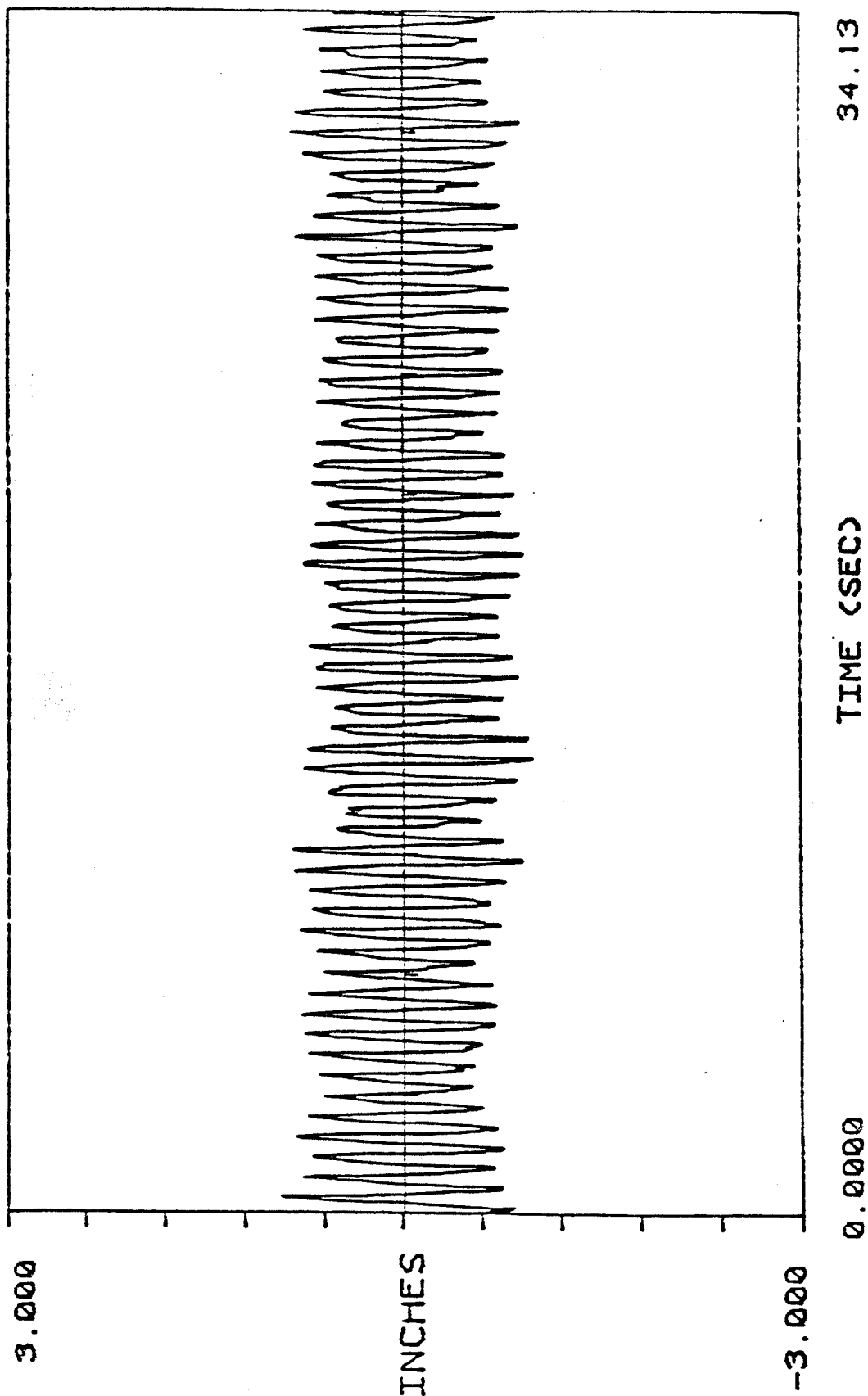
#### 4.4 Response Mode of In-line Motion

In section 3.6 it was stated that the in-line response frequencies are equal to the sum of the cross-flow response frequencies. The question arises, what mode responds in the in-line direction. These modal identification methods have been used to provide the answer, with some very surprising results. One such interesting case is described below.

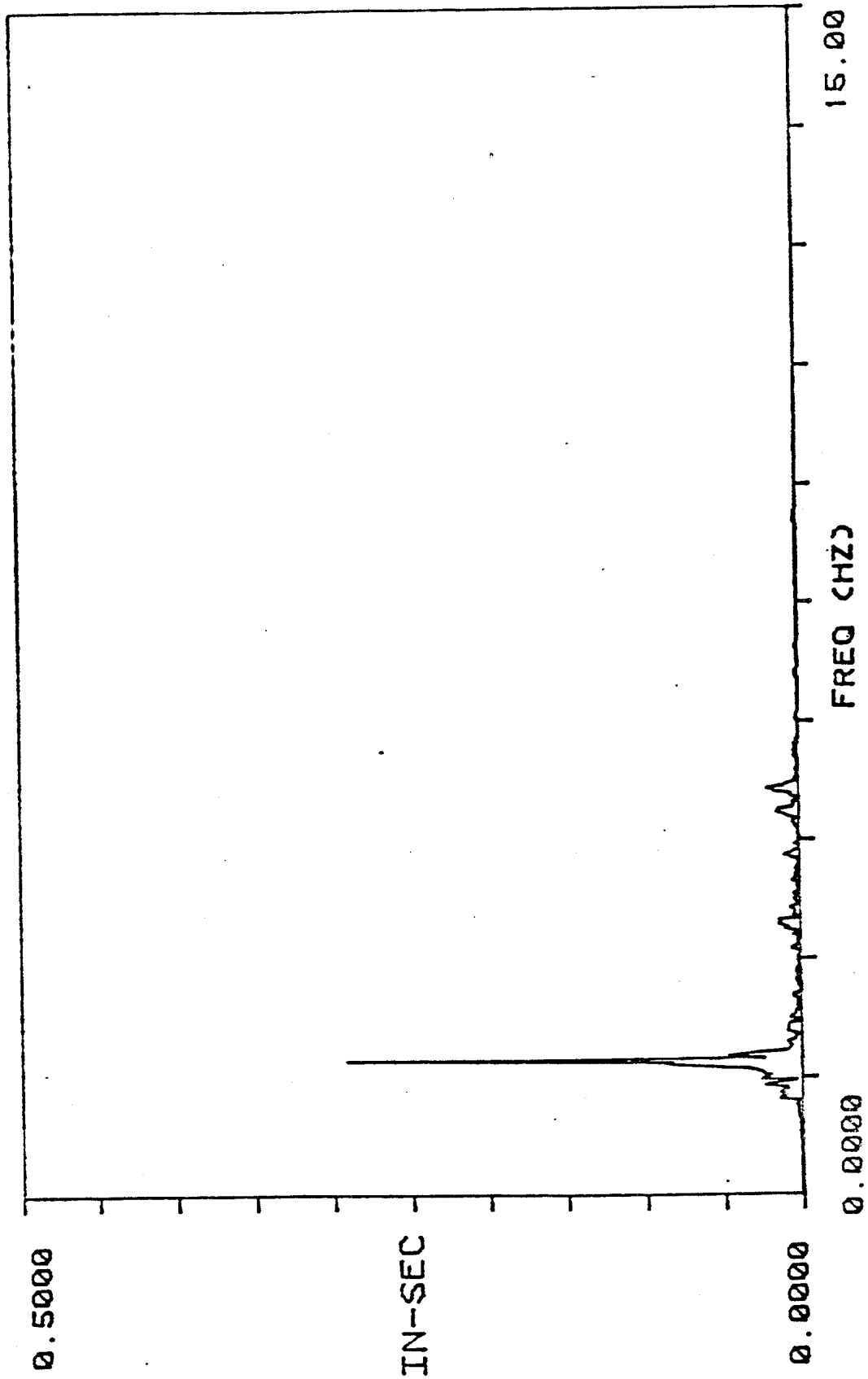
For a taut cable, all of the natural frequencies are integer multiples of the lowest. Therefore it is reasonable to expect that the fluctuating drag forces will excite an in-line mode whose natural frequency is twice that of the mode which is responsible for the cross-flow lock-in. As will be shown, this is often not the case. Figures 4-11 through 4-14 are the displacements and FFT's of the cable in the cross-flow and in-line direction at  $L/8$ . The cross-flow motion is at the second-mode natural frequency of the cable, and the in-line motion is at the fourth-mode natural frequency. Least squares modal identification was carried out in both directions and the resulting natural coordinates revealed that the cross-flow vibration was in the

second-mode shape, while the in-line vibration was in the third-mode shape as shown in Figure 4-15, instead of the fourth-mode as had been expected. The frequency of this third mode motion was not the natural frequency of the third mode but was in fact equal to the natural frequency of the fourth mode. The response was not resonant, but inertia controlled response of the third mode.

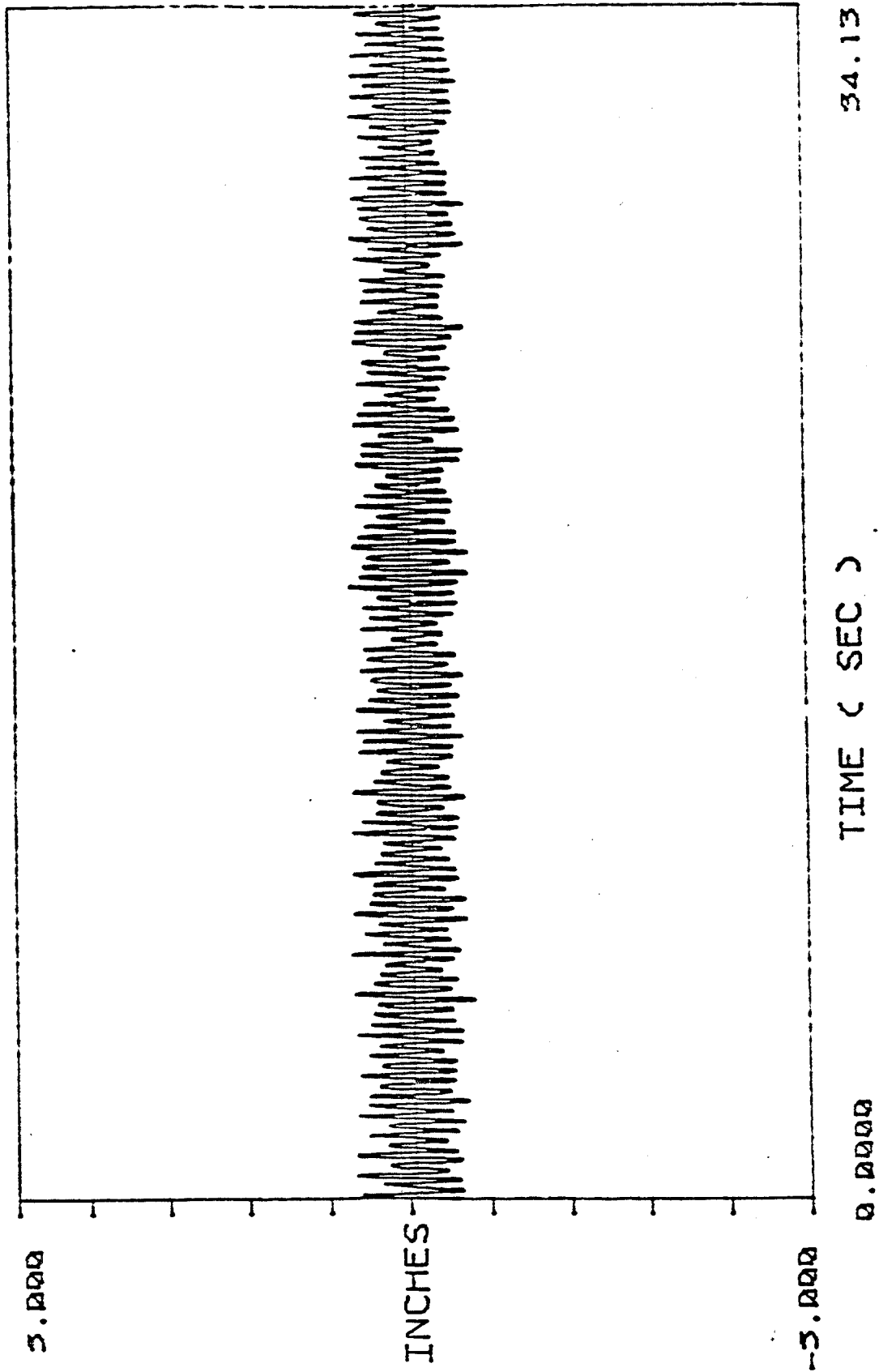
Similar peculiar results of the non-resonant in-line motion also happened for the non-lock-in case as mentioned in section 3.6. What were the in-line response frequencies? How to predict them? These questions will be answered by understanding the relationship between in-line and cross-flow response.



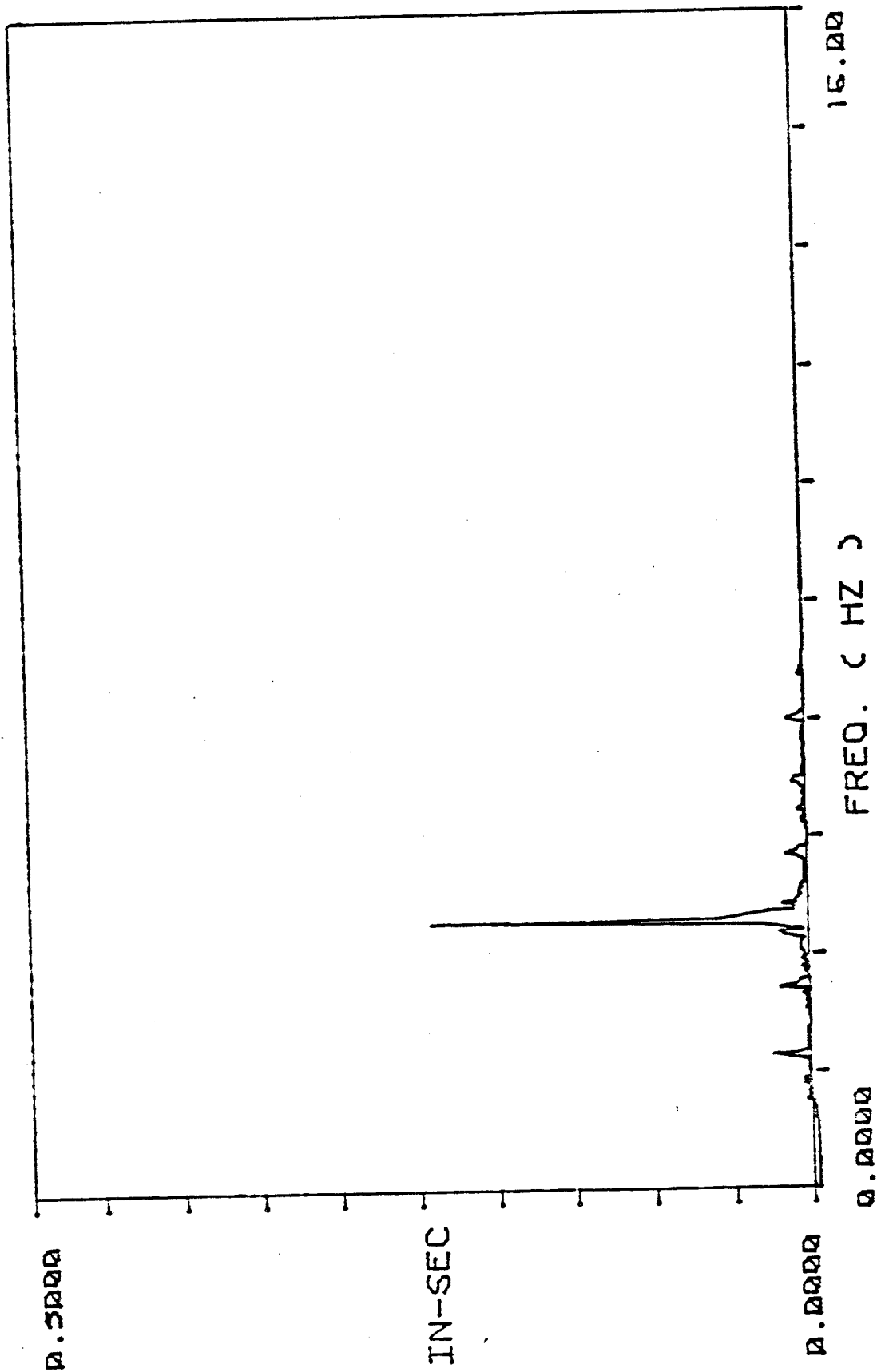
4-11 Cross-Flow Displacement of the Cable at L/8



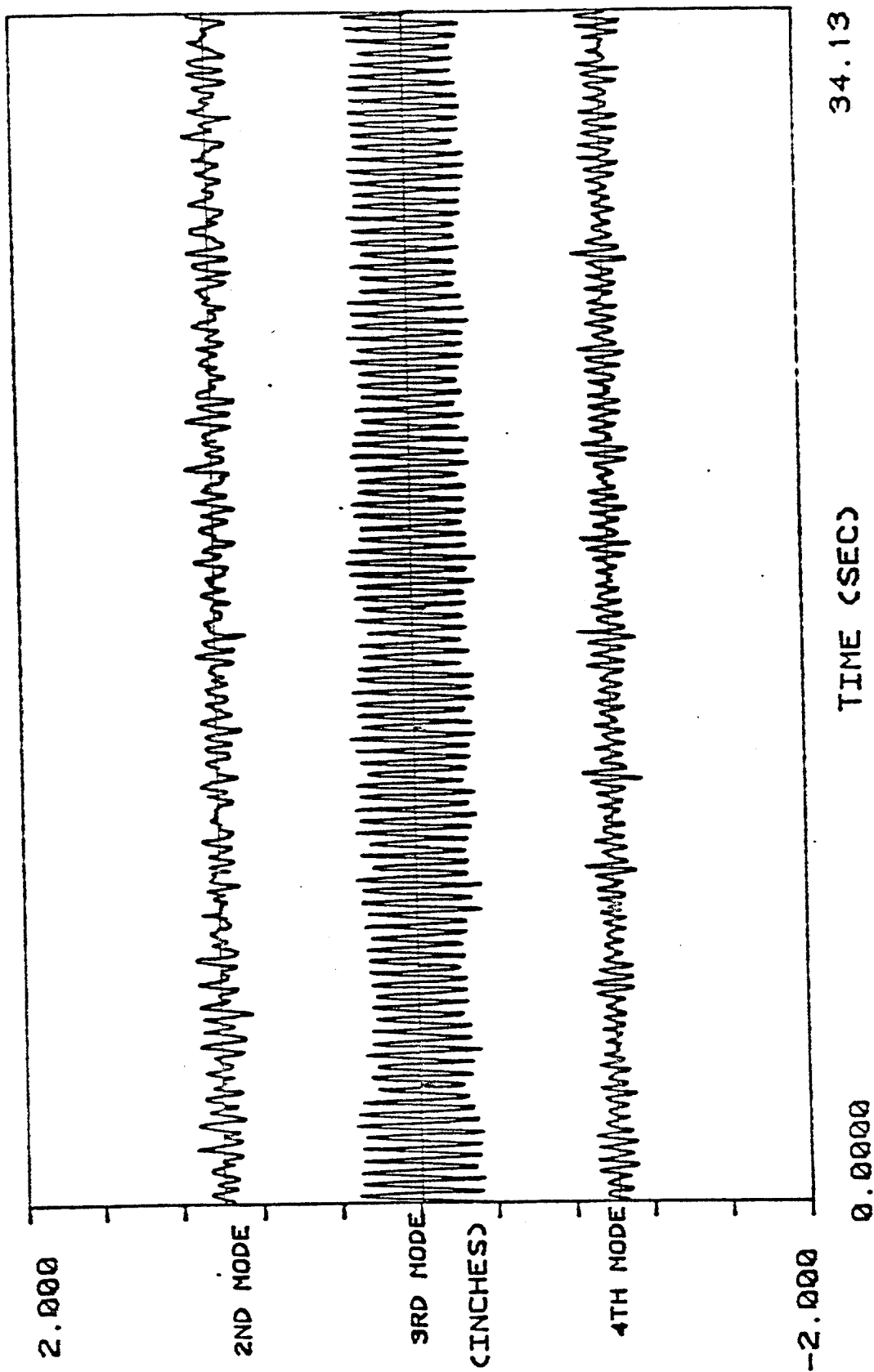
4-12 FFT of the Cross-Flow Displacement in Figure 4-11



4-13 In-Line Displacement of the Cable at L/8



4-14 FFT of the In-Line Displacement in Figure 4-13



4-15 In-Line Natural Coordinate Time Histories for 2nd,  
3rd and 4th Modes of the Cable

## CHAPTER 5

### BISPECTRAL ANALYSIS OF QUADRATIC CORRELATION

From the results of modal analysis, we know there must exist some kind of relation between in-line and cross-flow response as indicated by the closely related total vibration energies in these two directions as shown in figure 4-9. Next question is what kind of nonlinear relationship is it. In order to answer this question, a higher order spectral analysis is required to study the correlation between time histories resulting from a nonlinear process. In this chapter, the bispectrum, which is a cumulant average of a product of three spectral components, is used to investigate the quadratic coupling between these two direction responses.

#### 5.1 Introduction to The Cumulant Spectrum

For a set of random variables  $x_1, x_2, \dots, x_n$  the characteristic function is defined as [16]

$$\phi_{12\dots n}(V_1, V_2, \dots, V_n) = E[\exp(i \sum_{j=1}^n x_j V_j)] \quad (5.1.1)$$

The joint moment  $m_{12\dots n}$  and joint cumulant  $k_{12\dots n}$  can be expressed in terms of the characteristic function as



$$\begin{aligned}
 m_{12\dots n}(x_1, x_2, \dots, x_n) &= E[x_1, x_2, \dots, x_n] \\
 &= (-i)^n \frac{\partial^n \phi_{12\dots n}}{\partial V_1 \partial V_2 \dots \partial V_n} \Big|_{V_1=V_2=\dots=V_n=0}
 \end{aligned}
 \tag{5.1.2}$$

and

$$\begin{aligned}
 k_{12\dots n}(x_1, x_2, \dots, x_n) &= C[x_1, x_2, \dots, x_n] \\
 &= (-i)^n \frac{\partial^n \ln \phi_{12\dots n}}{\partial V_1 \partial V_2 \dots \partial V_n} \Big|_{V_1=V_2=\dots=V_n=0}
 \end{aligned}
 \tag{5.1.3}$$

where  $E[.]$  represents expected value, and  $C[.]$  represents the cumulant average. The relation between the joint cumulant and the joint moment can be expressed as

$$\begin{aligned}
 k_1 &= m_1 \\
 k_{12} &= m_{12} - m_1 m_2 \\
 k_{123} &= m_{123} - m_{12} m_3 - m_{13} m_2 - m_{23} m_1 + 2 m_1 m_2 m_3 \\
 k_{1234} &= m_{1234} - (m_{12} m_{34} + m_{13} m_{24} + m_{14} m_{23} + m_{123} m_4 + m_{124} m_3 + m_{134} m_2 \\
 &\quad + m_{234} m_1) + 2(m_{12} m_3 m_4 + m_{13} m_2 m_4 + m_{14} m_2 m_3 + m_{23} m_1 m_4 + m_{24} m_1 m_3 \\
 &\quad + m_{34} m_1 m_2) - 6 m_1 m_2 m_3 m_4
 \end{aligned}
 \tag{5.1.4}$$

From this relationship, the following two important properties are obtained:

- a) When  $n=3$ ,  $k_{12\dots n}=0$  for Gaussian random variables.
- b)  $k_{12\dots n}=0$ , when random variables  $x_1, x_2, \dots, x_n$  can be

divided into any two or more groups which are statistically independent of each other.

Notice that the moment  $m_{12\dots n}$  would not be zero, although the random variables  $x_1, x_2, \dots, x_n$  consist of independent groups, but the cumulant  $k_{12\dots n}$  would be zero. As a result, the cumulant can measure the extent of statistical dependence of the random variables.

For a stationary random time series  $x(t)$ , the  $n$ th order cumulant function is [6]:

$$C_n(U_1, U_2, \dots, U_{n-1}) = C[x(t)x(t+U_1)x(t+U_2)\dots x(t+U_{n-1})] \quad (5.1.5)$$

The Fourier representation of  $C_n(U_1, U_2, \dots, U_{n-1})$  is:

$$C_n(U_1, \dots, U_{n-1}) = \int \dots \int F_n(W_1, \dots, W_{n-1}) \exp(-i \sum_{k=1}^{n-1} W_k U_k) dW_1 \dots dW_{n-1} \quad (5.1.6a)$$

$$F_n(W_1, \dots, W_{n-1}) = \sum_{U_1} \dots \sum_{U_{n-1}} C_n(U_1, \dots, U_{n-1}) \exp(i \sum_{k=1}^{n-1} W_k U_k) \quad (5.1.6b)$$

$F_n$  is  $n$ th order cumulant spectrum. It can be shown that [16]:

$$C[X_1, X_2, \dots, X_n] = F_n(W_1, W_2, \dots, W_{n-1}) \delta\left(\sum_{j=1}^n W_j\right) \quad (5.1.7)$$

where

$$X_k = 1/T \int_0^T x(t) \exp(i W_k t) dt \quad (5.1.8)$$

$$\delta(x) = \begin{cases} 1, & \text{if } x=0 \\ 0, & \text{otherwise} \end{cases} \quad (5.1.9)$$

Equation (5.1.7) states that cumulant average of the Fourier amplitude of  $x(t)$  will be zero except when their sum frequency vanished. However if the waves at frequencies  $W_1, W_2, \dots, W_n$  can be divided into statistically independent groups, the cumulant spectrum will be zero even though their sum frequency is zero.

As a conclusion, cumulant spectrum will be zero unless both following two conditions are satisfied:

- a) Sum frequency  $W_1 + W_2 + \dots + W_n = 0$
- b) Waves at frequencies  $W_1, W_2, \dots, W_n$  are statistically related to each other.

Let  $x(t)$  be a zero mean stationary time series, the auto-bispectrum  $B(W_j, W_k)$  of  $x(t)$  is defined as:

$$B_{xxx}(W_j, W_k) = C[X_j X_k X_{j+k}]^* \quad (5.1.10)$$

The auto-bicoherence spectrum, a normalized auto-bispectrum,  $b(W_j, W_k)$  is:

$$b_{xxx}(W_j, W_k) = \frac{1}{\{E[|X_j|^2] E[|X_{j+k}|^2]\}^{0.5}} B_{xxx}(W_j, W_k) \quad (5.1.11)$$

By using Schwarz' inequality, it can be shown that auto-bicoherence spectrum  $b(W_j, W_k)$  is bounded by  $0 \leq b(W_j, W_k) \leq 1$ . If the wave at  $W_j + W_k$  is excited by coupling of the waves at  $W_j$  and  $W_k$ , the auto-bicoherence spectrum will be close to unity. On the other hand, if wave at  $W_j + W_k$  is uncorrelated quadratically to the waves at  $W_j$  and  $W_k$ ,  $b_{xxx}(W_j, W_k)$  will be near zero.

Let  $x(t)$  and  $y(t)$  be two zero mean jointly stationary time series, the cross-bispectrum  $B_{xy}(W_j, W_k)$  between  $x(t)$  and  $y(t)$  is:

$$B_{xy}(W_j, W_k) = C[X_j X_k Y_{j+k}] \quad (5.1.12)$$

The cross bicoherence spectrum  $b_{xy}(W_j, W_k)$  between  $x(t)$  and  $y(t)$  is:

$$b_{xy}(W_j, W_k) = \frac{1}{\{E[|X_j|^2] E[|Y_{j+k}|^2]\}^{0.5}} B_{xy}(W_j, W_k) \quad (5.1.13)$$

The cross bicoherence spectrum also ranges from zero to unity. If the wave at  $W_j + W_k$  in  $y(t)$  is excited by coupling of waves at  $W_j$  and  $W_k$  in  $x(t)$ , the cross-bicoherence spectrum  $b_{xy}(W_j, W_k)$  will be close to unity. If the wave at

$W_j + W_k$  in  $y(t)$  is uncorrelated quadratically to the waves at  $W_j$  and  $W_k$  in  $x(t)$ ,  $b_{xxy}(W_j, W_k)$  will be near zero.

## 5.2 Cross-bicoherence Spectrum Test Examples

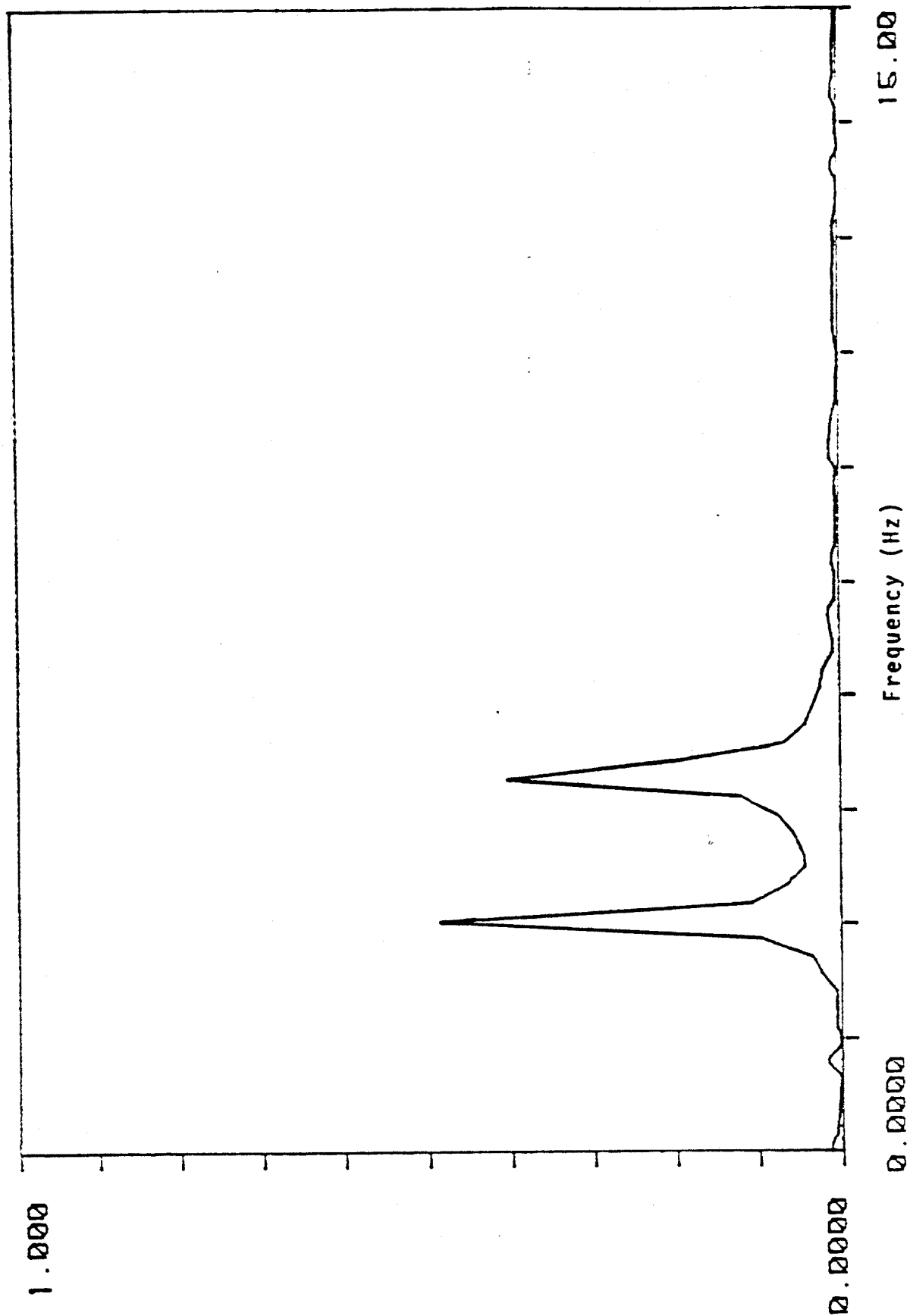
In order to illustrate how the cross-bicoherence spectrum can detect quadratic coupling between waves, the following five examples were tested. Six time series were generated on a computer as follow:

$$\begin{aligned}
 x(t) &= \cos(Wat + Pa) + \cos(Wbt + Pb) + n(t) \\
 y_1(t) &= \cos(Wct + Pc) + n(t) \\
 y_2(t) &= \cos(Wct + Pa + Pb) + n(t) \\
 y_3(t) &= \cos(Wat + pa) * \cos(Wbt + Pb) + n(t) \\
 y_4(t) &= \cos(Wat + Pa) * \cos(Wbt + Pb) + 0.5 \cos(Wct + Pc) + n(t) \\
 y_5(t) &= \cos(Wat + Pa) * \cos(Wbt + Pb) ** 2 + n(t)
 \end{aligned}
 \tag{5.2.1}$$

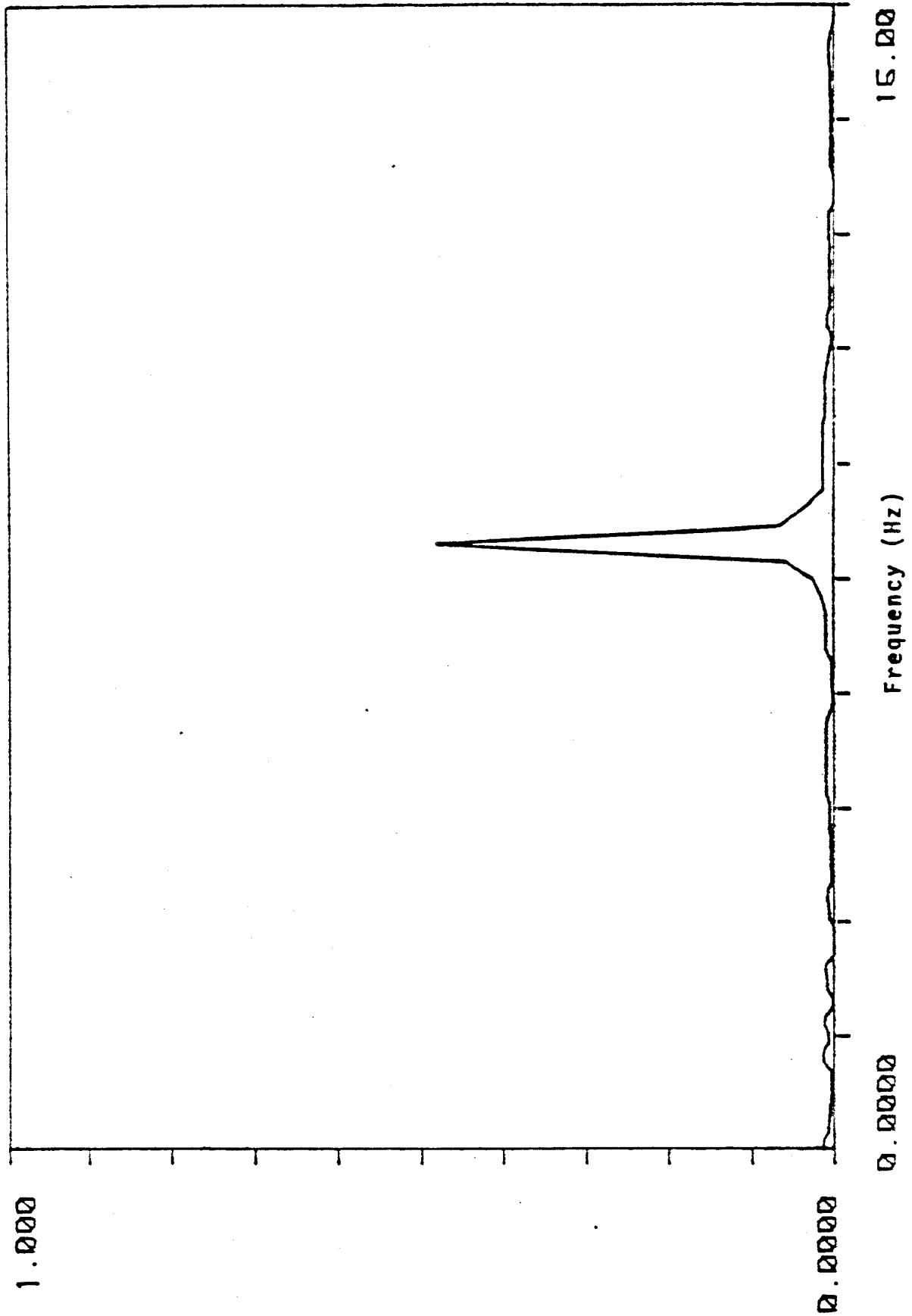
-20 dB Gaussian white noise  $n(t)$  was added to each series and these noise components were independent for each series. Random phase  $Pa$ ,  $Pb$ ,  $Pc$  were chosen from a set of independent pseudo random numbers, uniformly distributed over  $(0, 2\pi)$ , and  $fa = 3$  Hz,  $fb = 5$  Hz,  $fc = fa + fb = 8$  Hz. The sampling frequency was 30 Hz.

Figures 5-1 through 5-6 show the spectra of  $x(t)$  and  $y_1(t)$  to  $y_5(t)$ , and figure 5-7 through 5-11 show the cross-bicoherence spectrum between  $x(t)$  and  $y_1(t)$  to  $y_5(t)$ . Notice that  $y_1(t)$  and  $x(t)$  are uncorrelated while  $y_2(t)$  and

$x(t)$  are correlated quadratically, but the spectra of  $y_1(t)$  and  $y_2(t)$  are identical to each other. This is because the spectrum is independent of the phase of the waves. Both cross-spectra  $S_{xy1}(W)$  and  $S_{xy2}(W)$  are also zero because they are linear independent of each other. However the cross-bicoherence spectrum  $b_{xyl}(W_1, W_2)$  and  $b_{xy2}(W_1, W_2)$  is sensitive to phase.  $b_{xyl}(W_1, W_2)$  in figure 5-7 shows no quadratic correlation between  $x(t)$  and  $y_1(t)$ , but  $b_{xy2}(W_1, W_2)$  in figure 5-8 shows a peak close to unity at frequencies  $(W_a, W_b)$  which means that wave at  $W_c = W_a + W_b$  in  $y_2(t)$  is quadratically correlated to the waves at  $W_a$  and  $W_b$  in  $x(t)$ . Higher order spectral analysis must be invoked to detect any possible correlation between waves due to quadratic nonlinearity. The wave at  $W_c = W_a + W_b$  in  $y_3(t)$  is due to the product of waves at  $W_a$  and  $W_b$  in  $x(t)$ , so  $b_{xy3}(W_1, W_2)$  in figure 5-9 shows a peak close unity at  $(W_a, W_b)$ . In series  $y_4(t)$ , a wave at frequency  $W_c$ , independent of  $x(t)$ , was added to  $y_3(t)$ . Figure 5-10 shows that  $b_{xy4}(W_a, W_b) = 0.48$  which implies that only half of the power at  $W_c$  is due to the quadratic interaction of the wave at  $W_a$  and  $W_b$  in  $x(t)$ . In the last example, even though  $y_5(t)$  is coupled cubically with  $x(t)$ , no correlation was detected in the cross-bicoherence spectrum  $b_{xy5}(W_1, W_2)$  in figure 5-11. This is because bispectrum can only detect correlation between waves which are quadratically coupled.

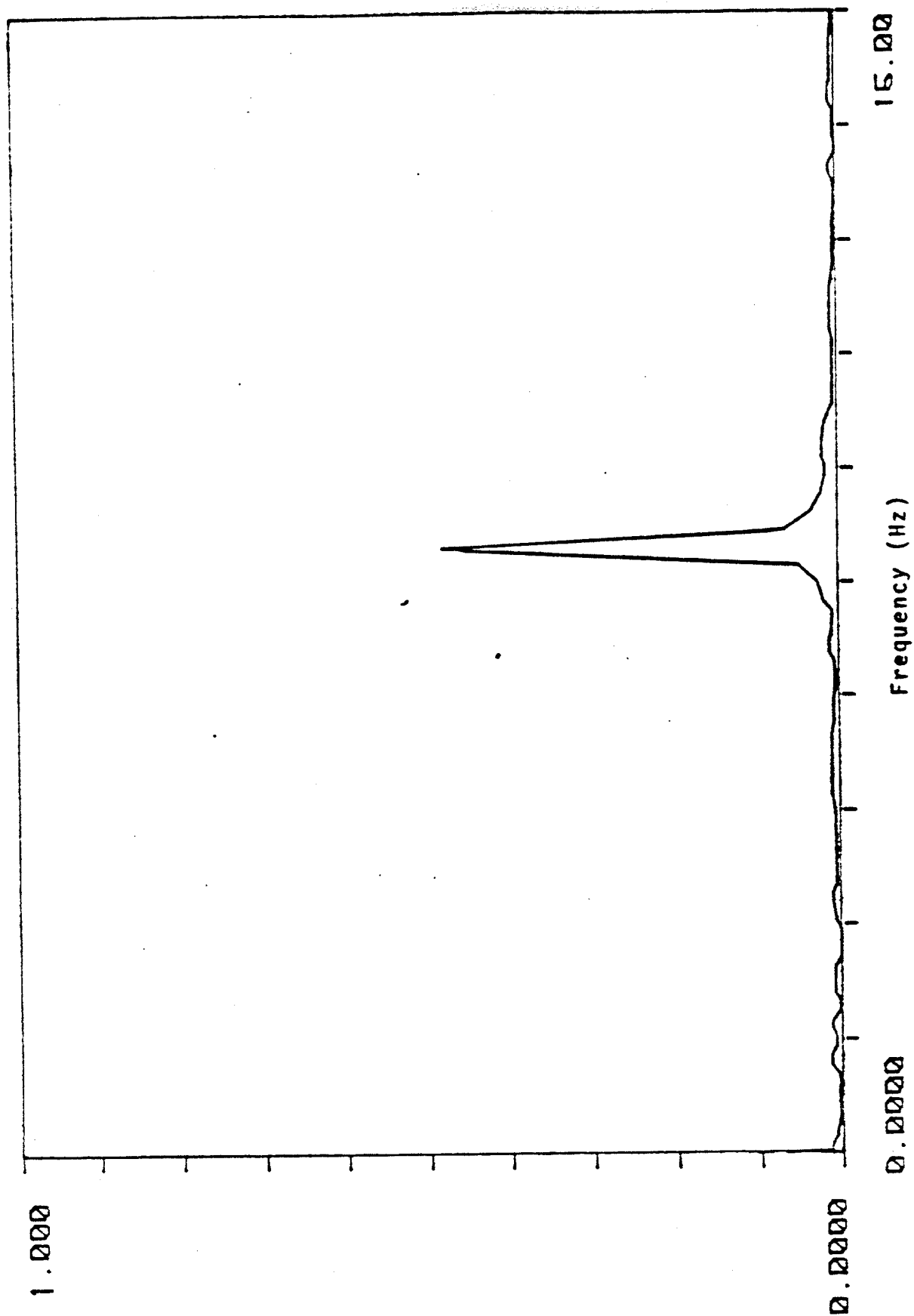


5-1 Power Spectrum of the Test Data  $x(t)$

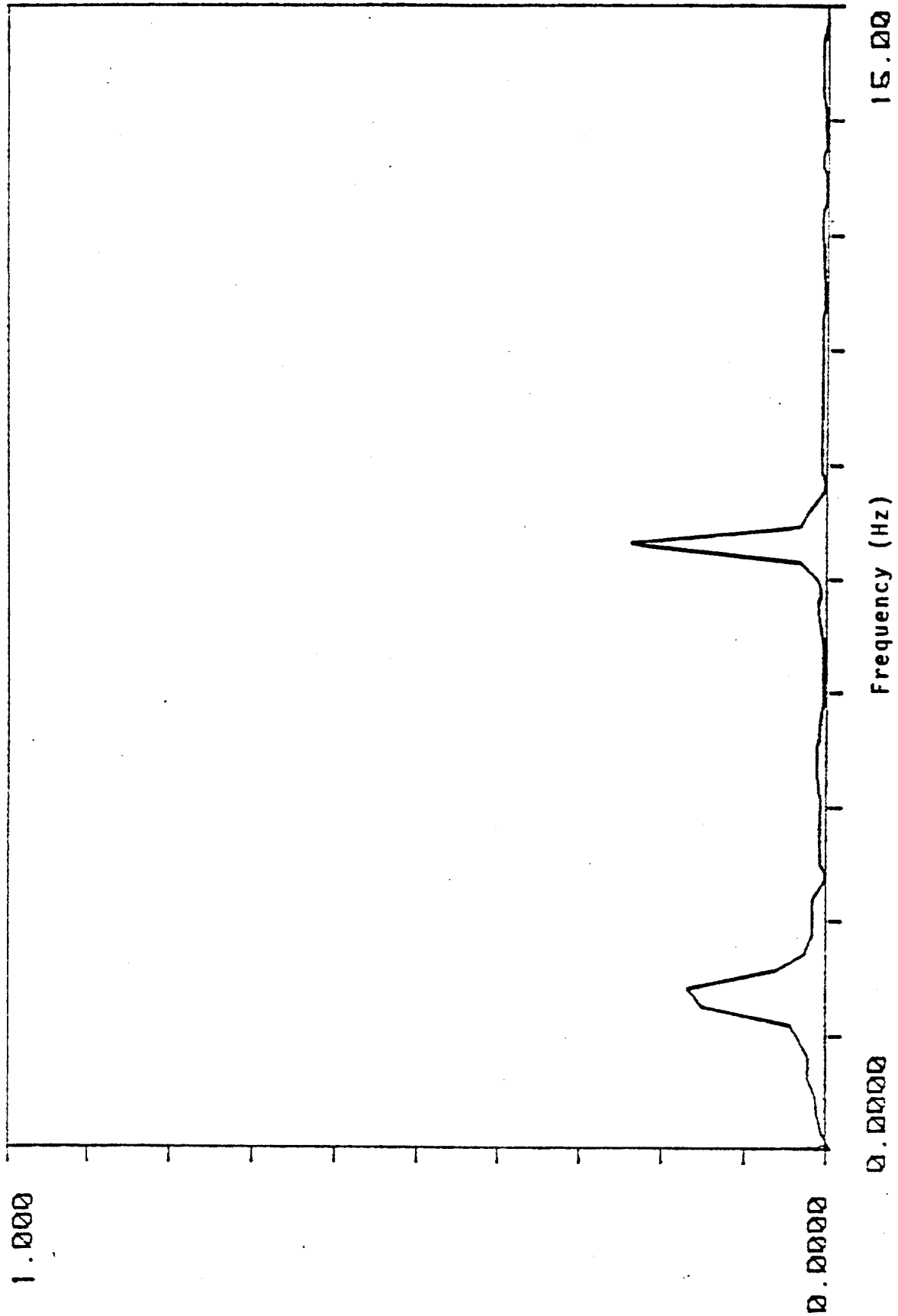


5-2 Power Spectrum of the Test Data y1(t)

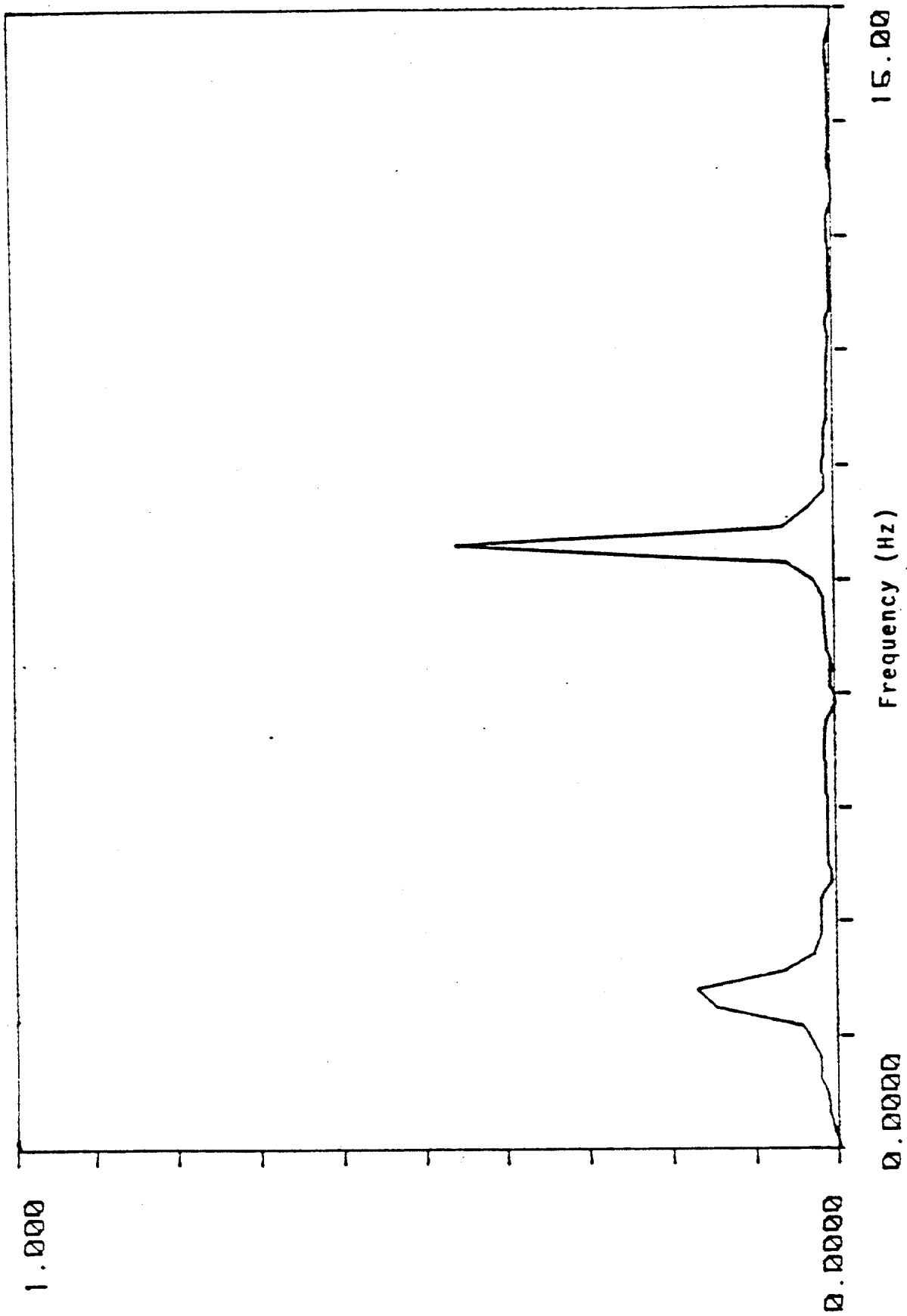




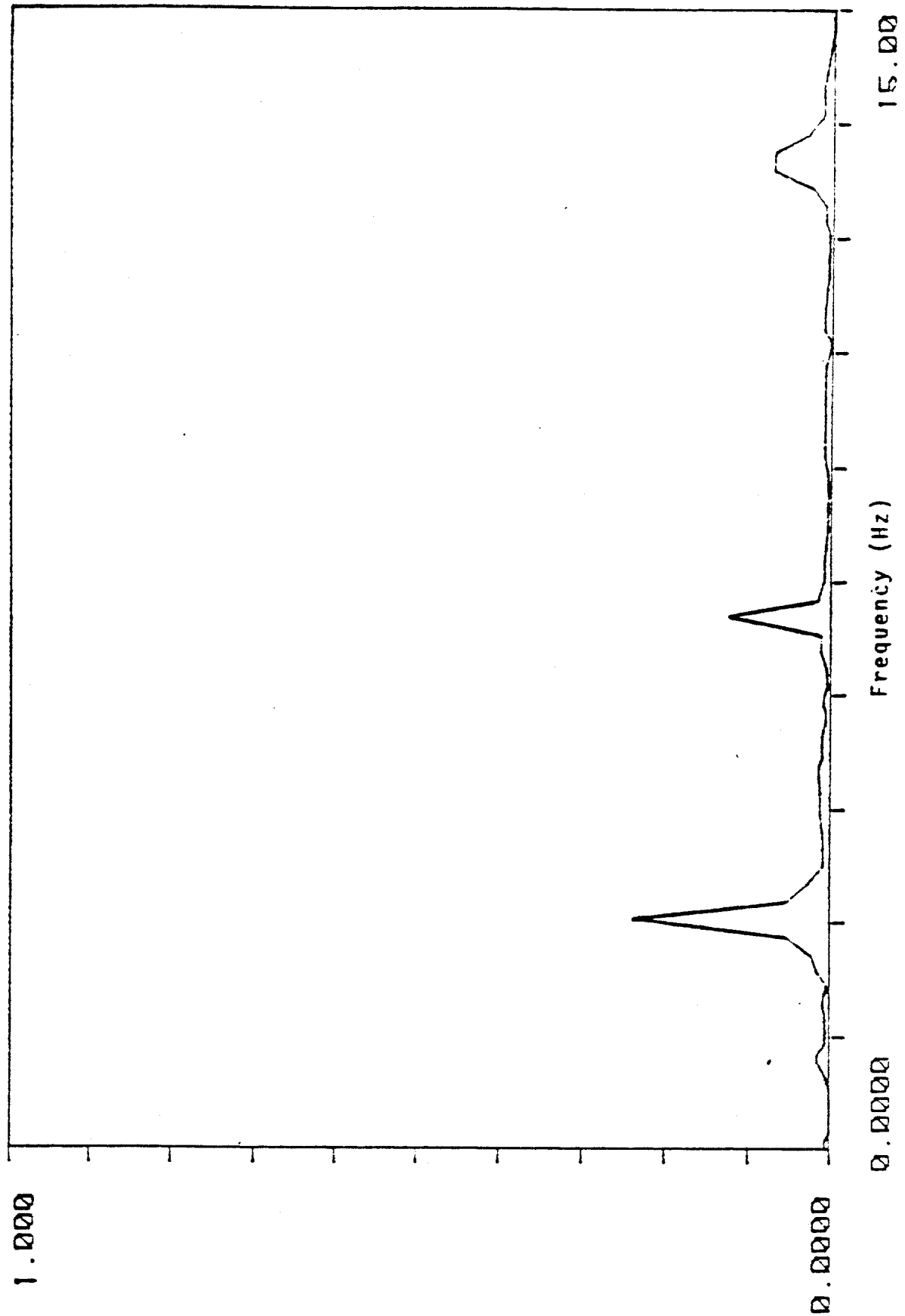
5-3 Power Spectrum of the Test Data  $y_2(t)$



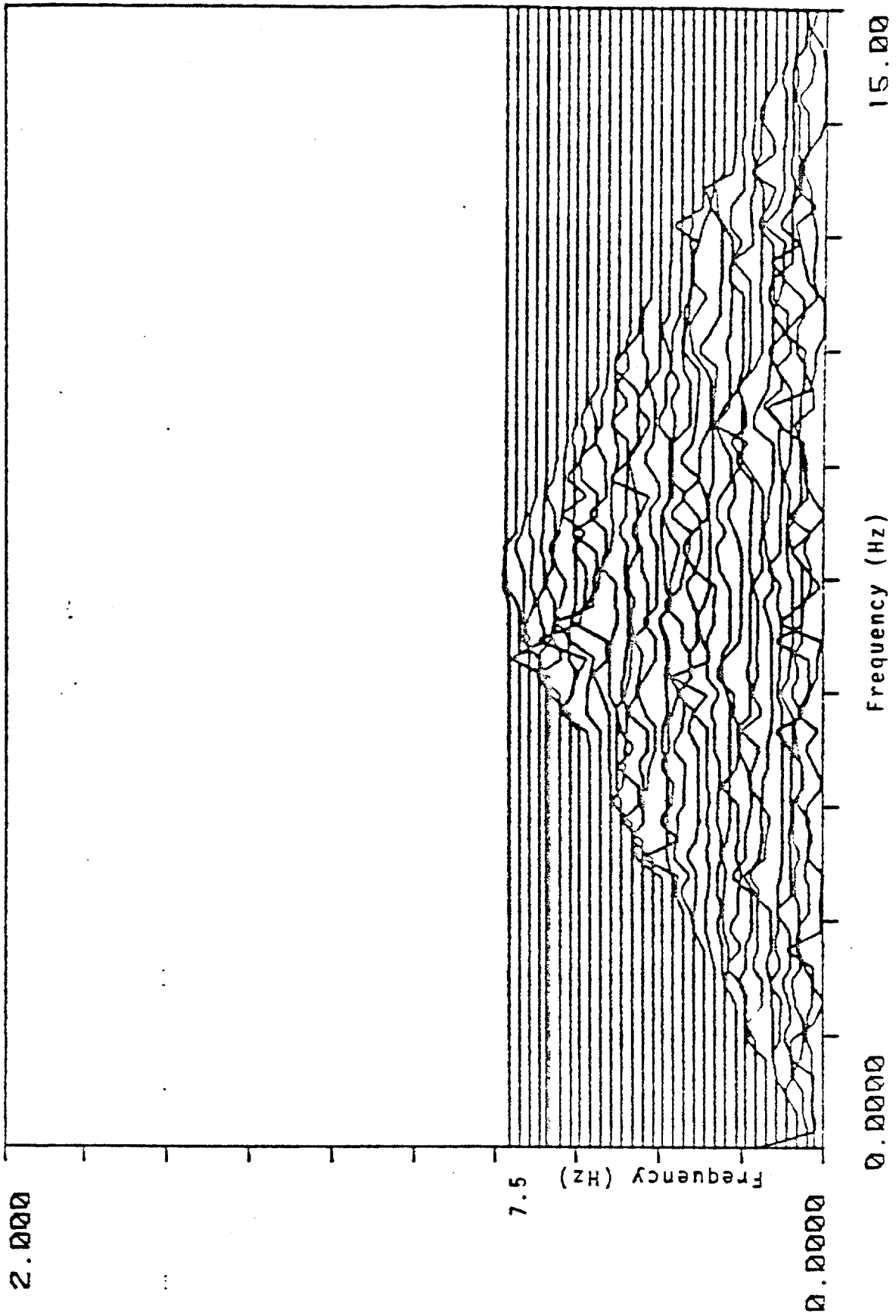
5-4 Power Spectrum of the Test Data y3(t)



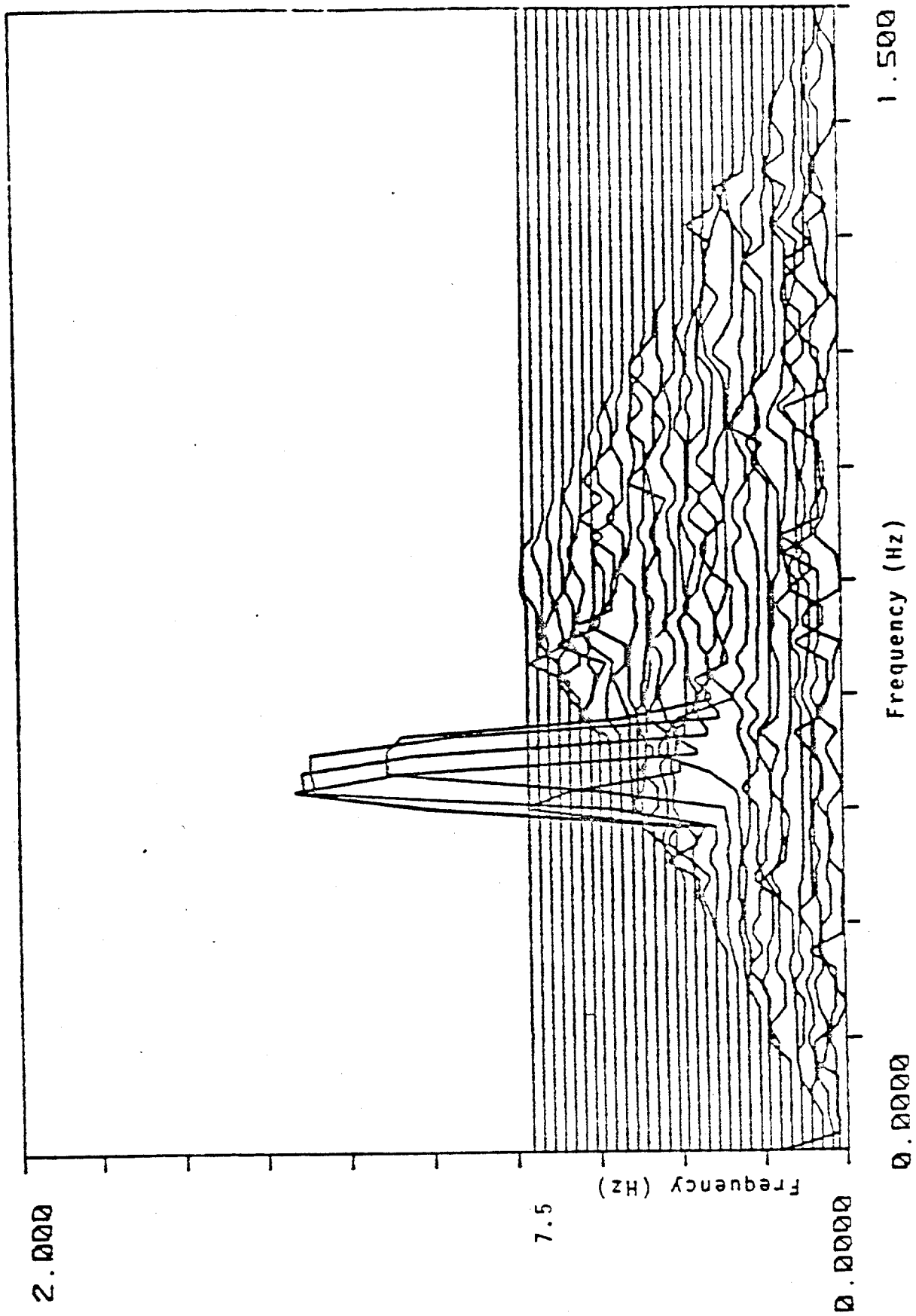
5-5 Power Spectrum of the Test Data y4(t)



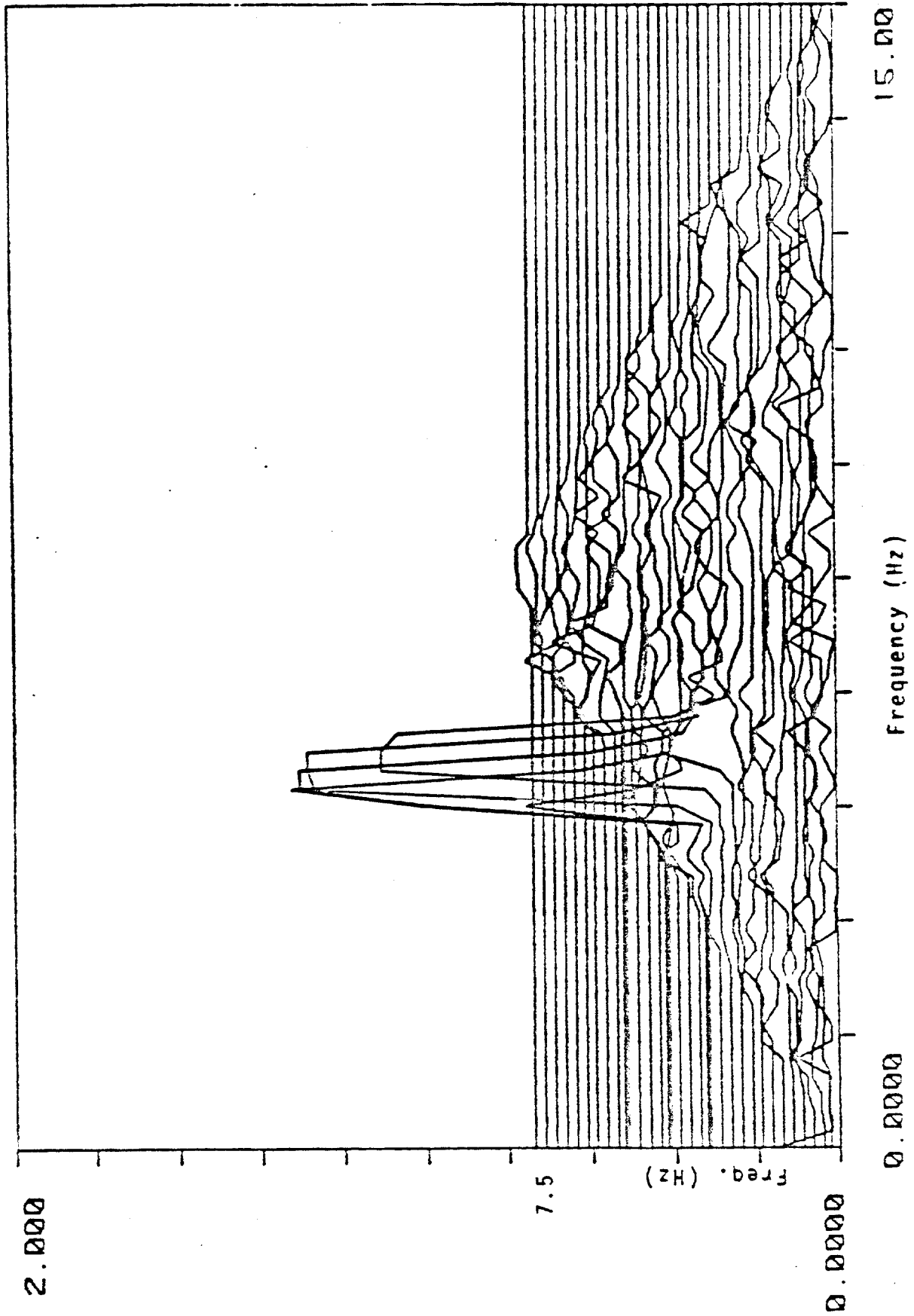
5-6 Power Spectrum of the Test Data y5(t)



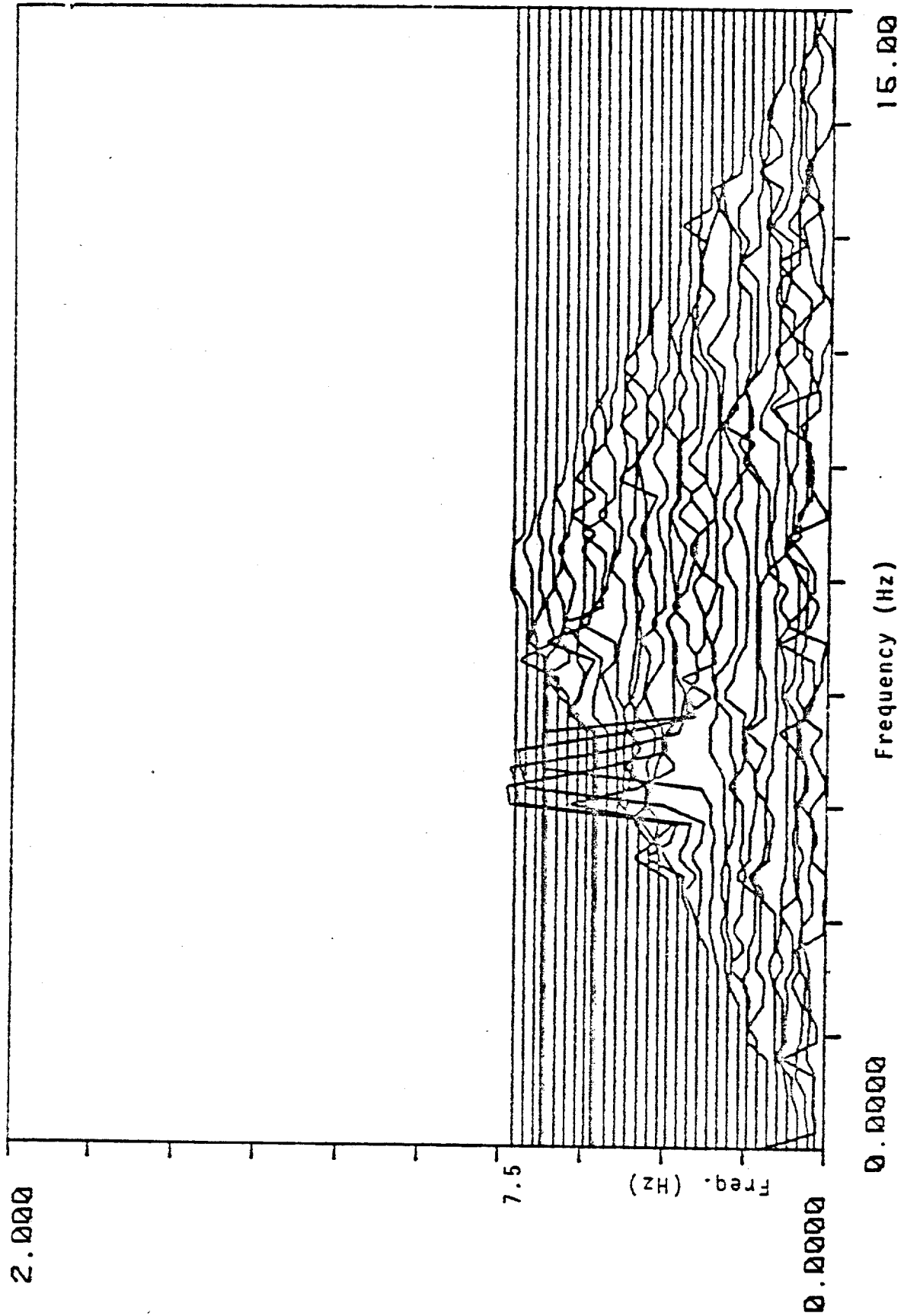
5-7 Coran-Bicoherence Between  $x(t)$  and  $y_1(t)$



5-8 Cross-Coherence Between  $x(t)$  and  $y_2(t)$

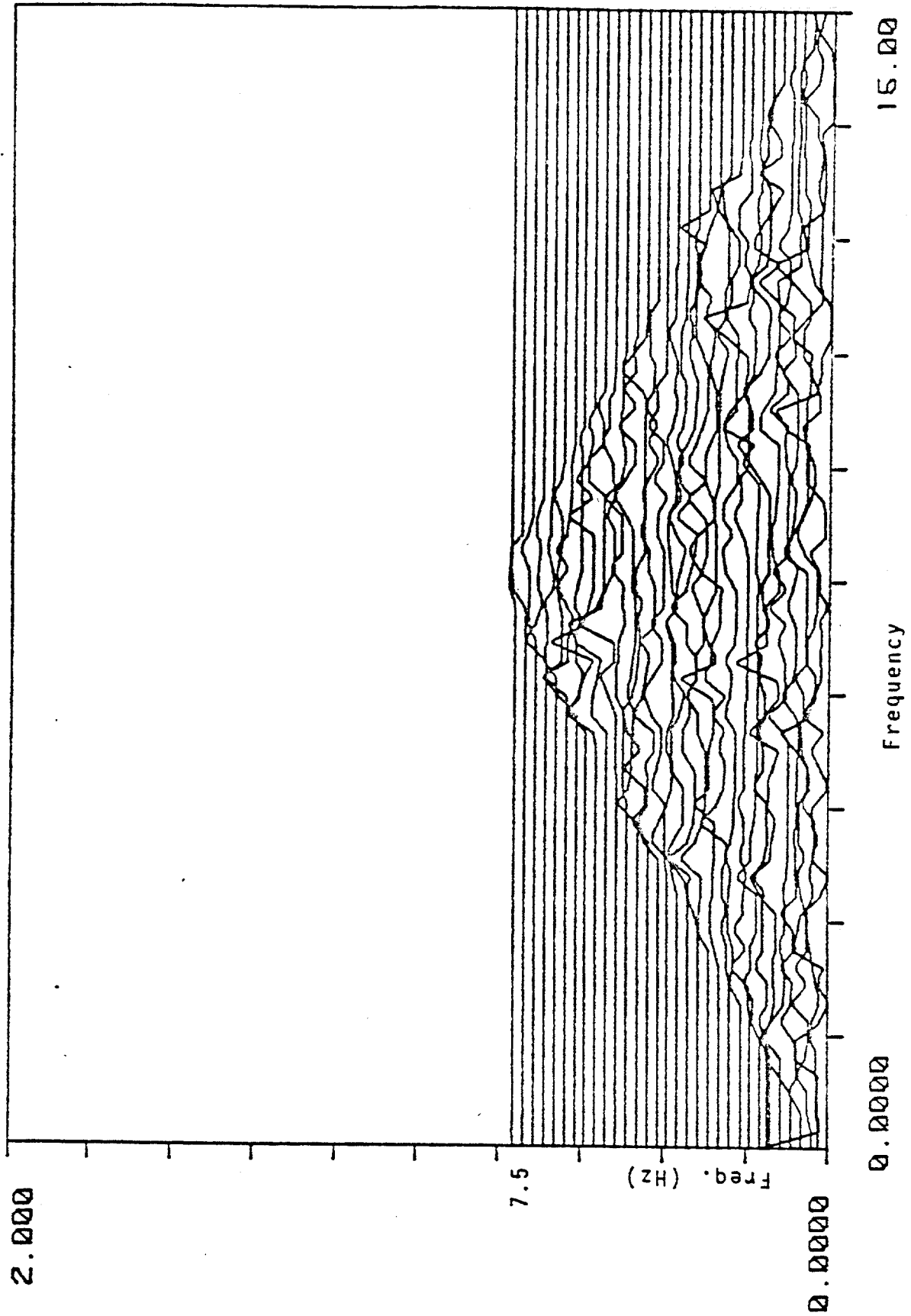


5-9 Cross-Coherence Between  $x(t)$  and  $y_3(t)$



5-10 Cross-Bicoherence Between  $x(t)$  and  $y_4(t)$



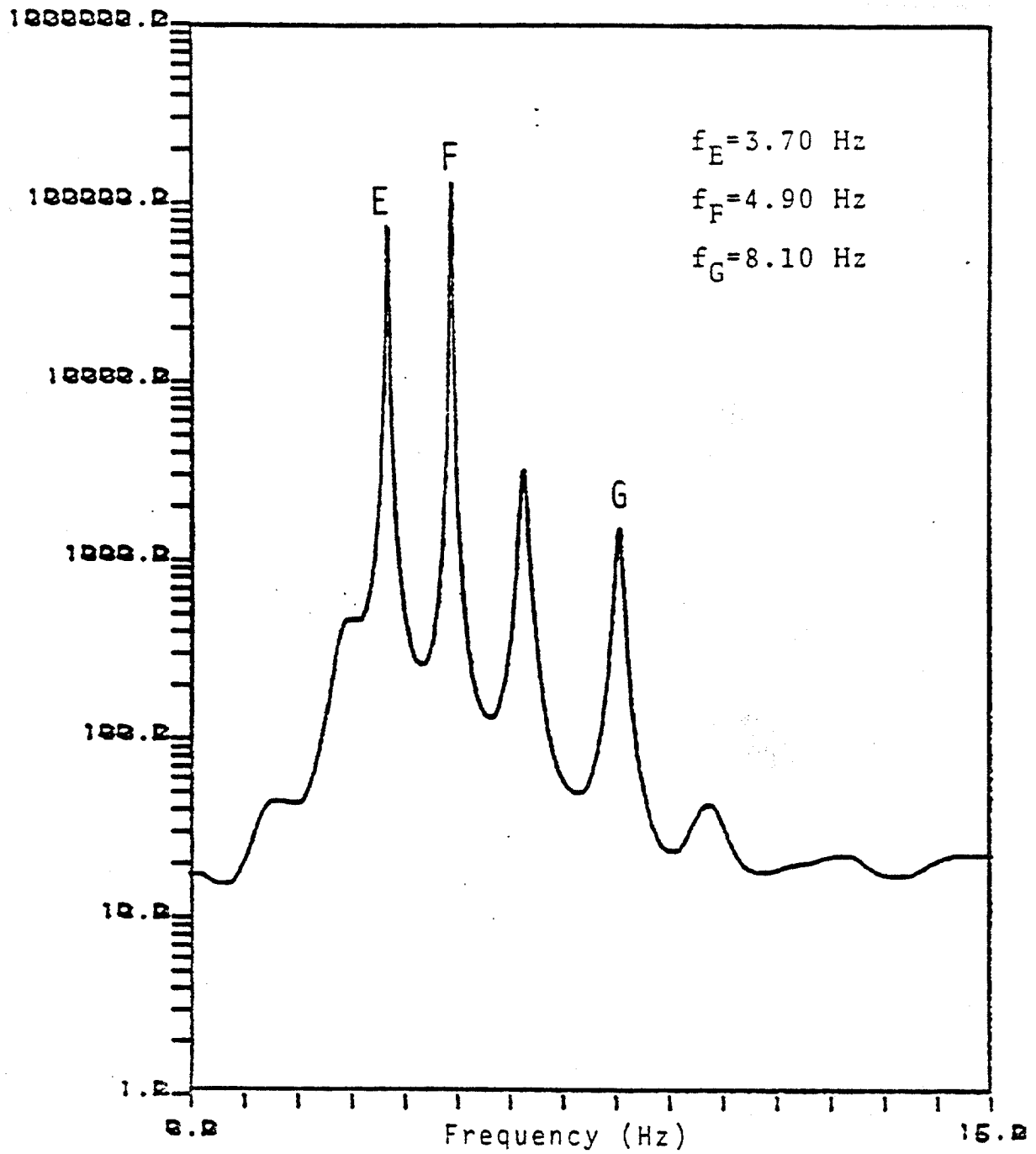


5-11 Cross-Bicoherence Between  $x(t)$  and  $y_5(t)$

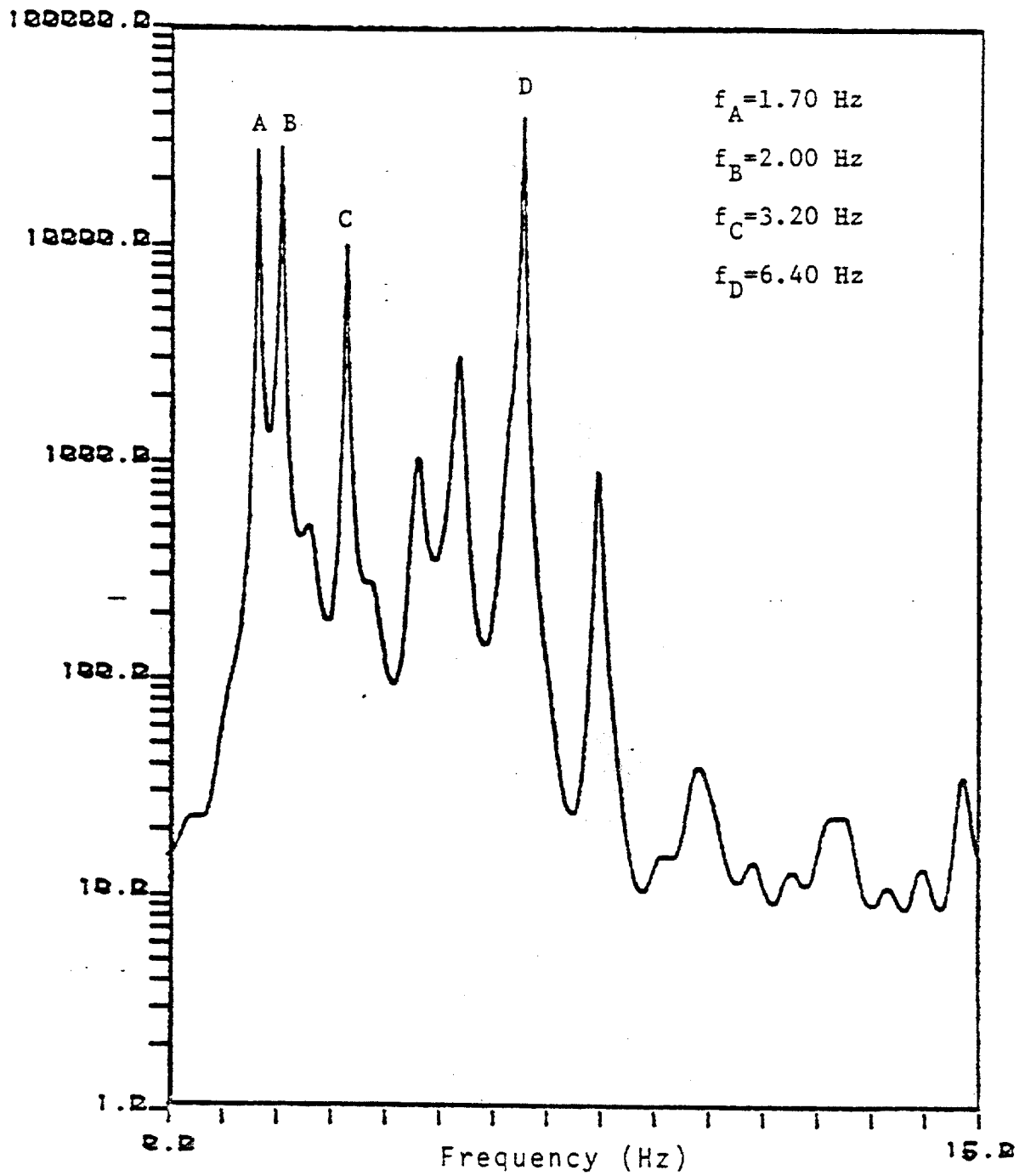
From these examples, it is seen that, due to the lack of phase information, the spectrum is not able to give a positive and quantitative answer to the quadratic correlation but bispectrum can. The bispectrum is a useful tool in the investigation of the quadratic correlation problem of vortex-induced vibration of cylinders in which experimental observation results the frequency summing phenomenon in both lockin and non-lockin cases.

### 5.3 Quadratic Correlation Between In-Line and Cross-Flow Response

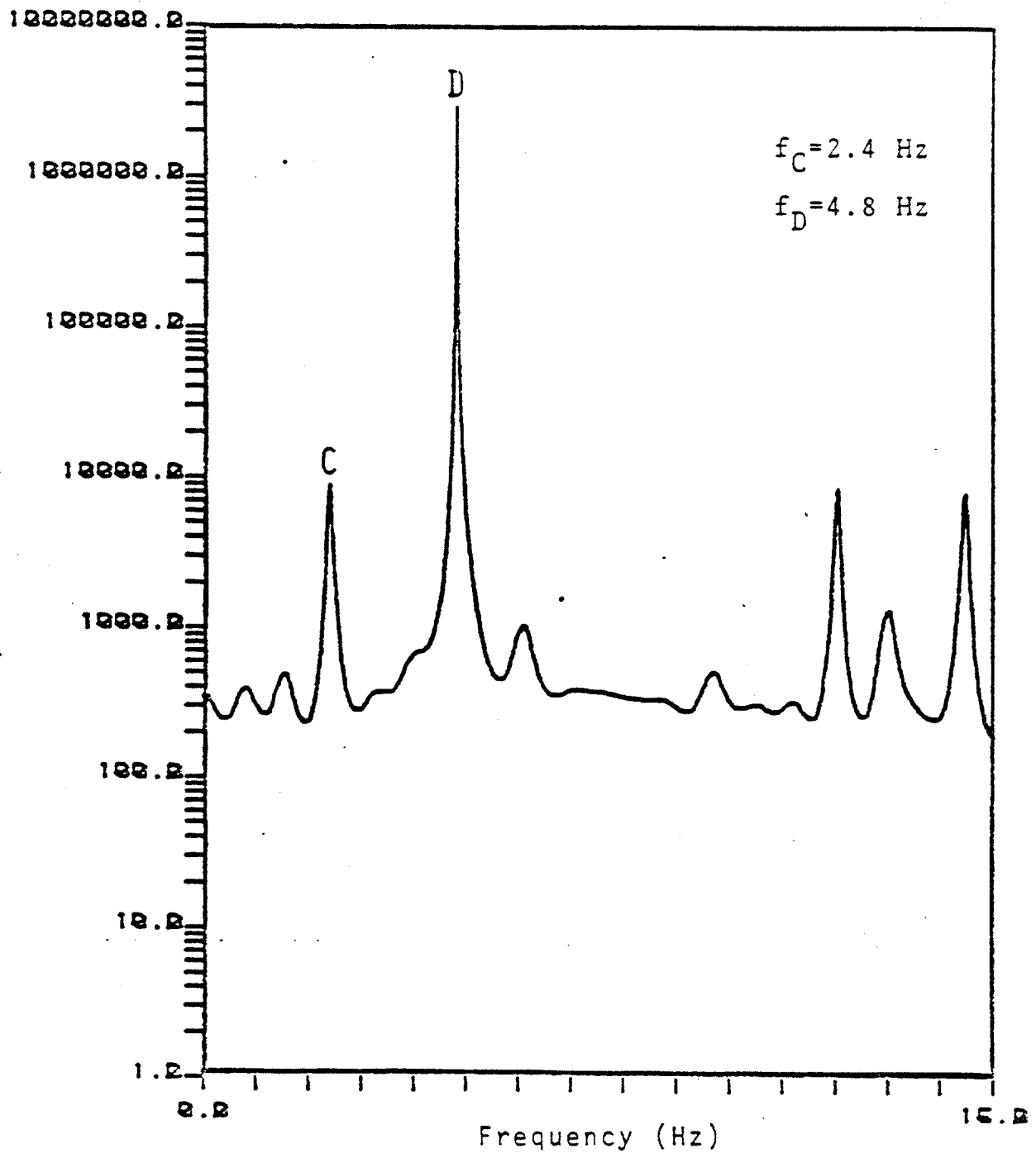
As mentioned before, the frequency summing or doubling phenomena were observed from the test data for both lockin and non-lockin cases. The problem to be answered in this section is: does any quadratic correlation exist between the non-lock-in response at frequencies 3.7 HZ, 4.9 HZ in the in-line response shown in figure 5-12 and waves at frequencies 1.7 HZ, 2.0 HZ, 3.2 HZ in the cross-flow response in figure 5-13. In this figure, the frequency at 3.7 HZ equals to the sum of frequencies at 1.7 HZ and 2.0 HZ. Also the frequency at 4.9 HZ equals to the sum of frequencies at 1.7 HZ and 3.2 HZ. Similary for a lock-in case, is there any quadratic correlation between the wave at 2.4 HZ in the cross-flow response shown in figure 5-14 and the wave at 4.8 HZ, double of 2.4 HZ, in the in-line



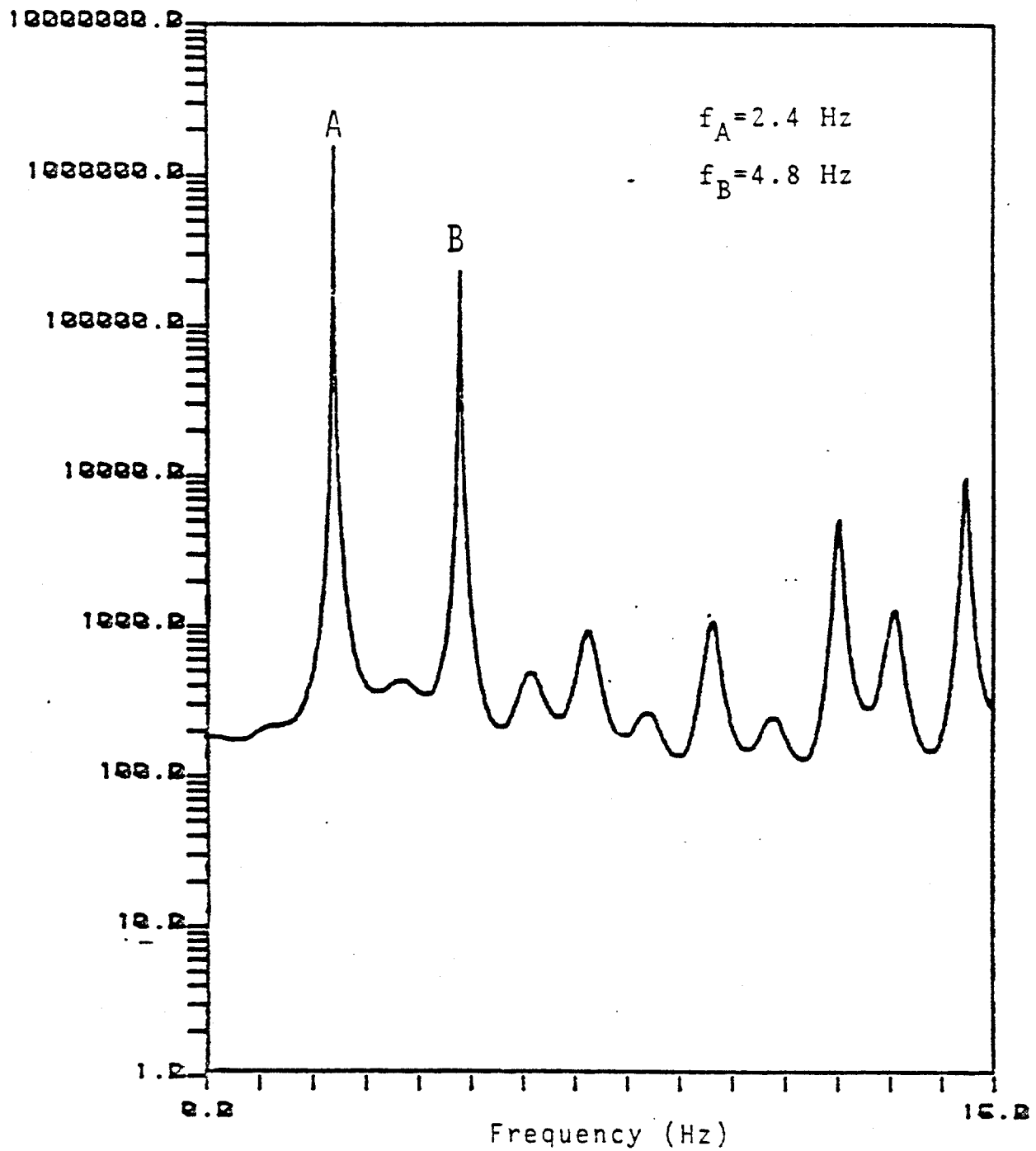
5-12 Power Spectrum of In-line Response at Non-lock-in



5-13 Power Spectrum of Cross-Flow Response at Non-lock-In



5-14 Power Spectrum of In-Line Response at Lock-in

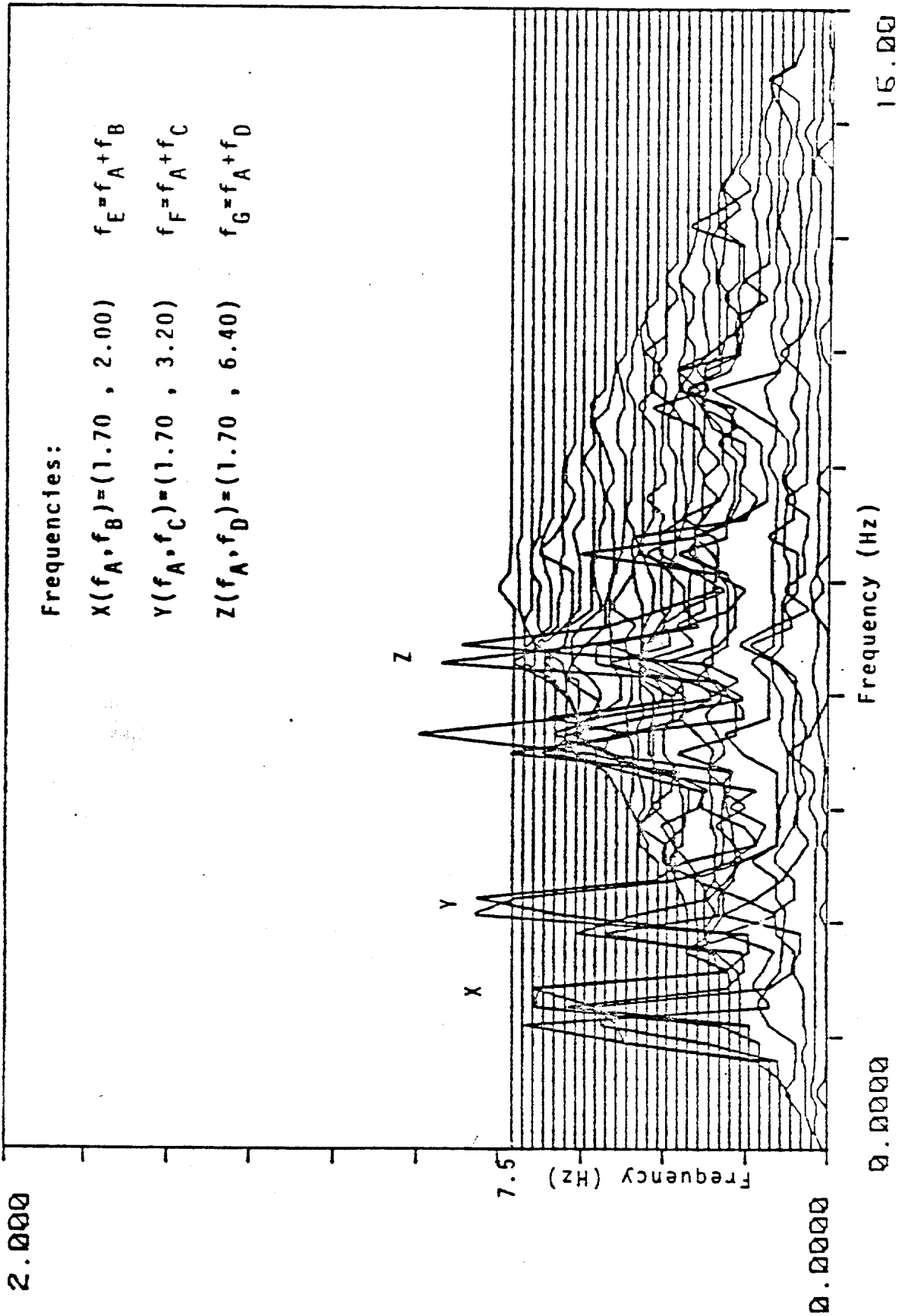


5-15 Power Spectrum of Cross-Flow Response at Lock-in

response in figure 5-15. Are all these waves at different frequencies independent? Because of the frequency summing property, the bispectral analysis technique is the appropriate tool to answer these questions.

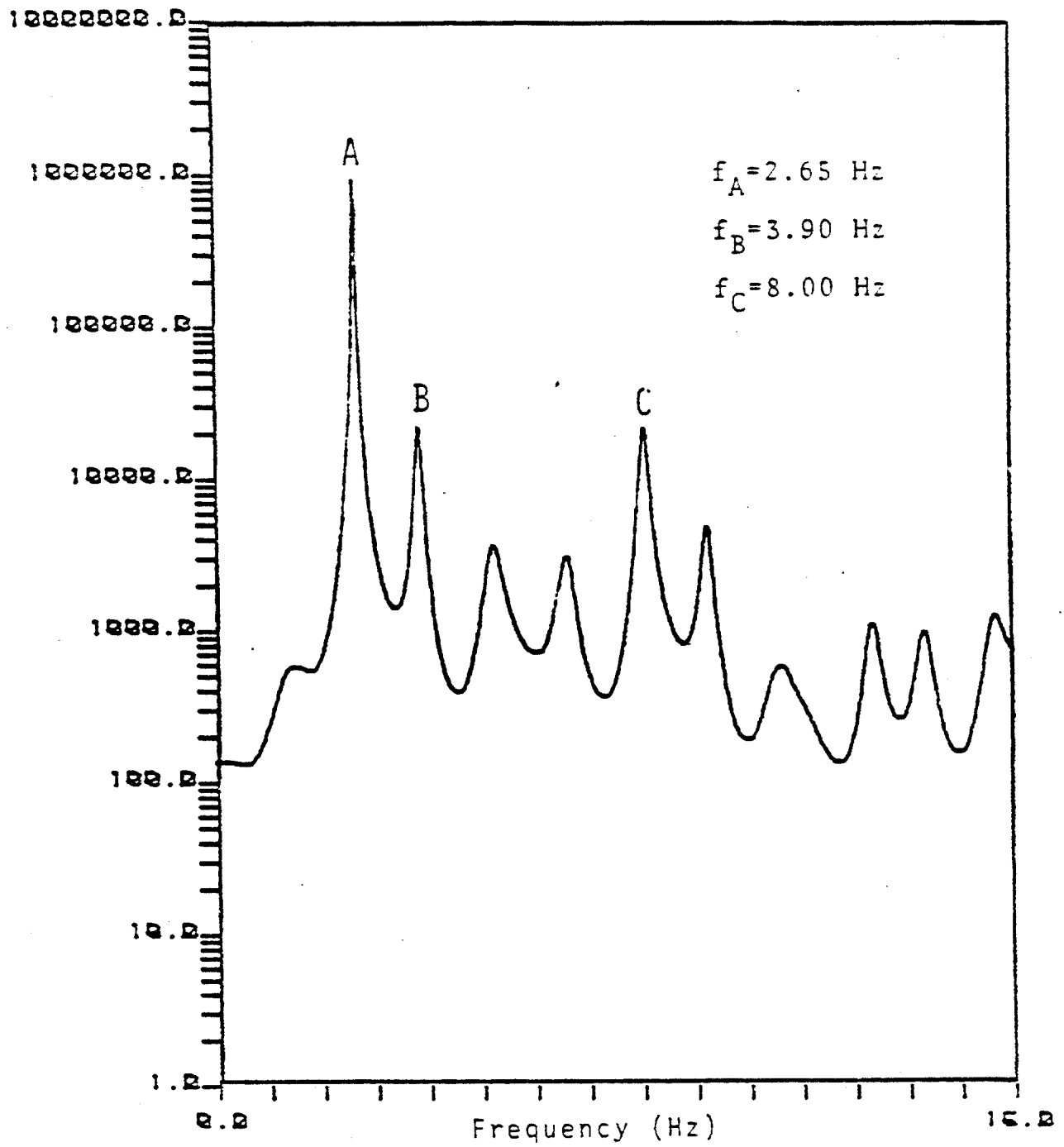
For the nonlock-in case, the cross-bicoherence spectrum  $b_{xy}(W_1, W_2)$  between cross-flow and in-line response, shown in figure 5-16, was obtained by averaging 100 segments of 128 data points each. The cross-flow and in-line spectra are shown in Figures 5-13 and 5-12 respectively. The peak shown at  $b_{xy}(1.7, 2.0)$  means that wave at 3.7 HZ in in-line response is due to quadratic coupling of waves at 1.7 HZ and 2.0 HZ in the cross-flow response. Similarly the peak at  $b_{xy}(1.7, 3.2)$  means that a wave at 4.9 HZ is due to quadratic coupling of waves at 1.7 HZ and 3.2 HZ in the cross-flow response. The rest of the peaks in  $b_{xy}(W_1, W_2)$  all have the same interpretation. Using these techniques, a strong quadratic correlation was detected between in-line and cross-flow responses for the non-lock-in case.

Another example for a near-lock-in case also showed quadratic correlation. The cross-bicoherence spectrum  $b_{xy}(W_1, W_2)$  is shown in figure 5-19 and the power spectra of cross-flow and in-line responses are shown in figure 5-17 and 5-18 respectively for the near-lock-in case. Peaks due to frequency summing were all the result of quadratic

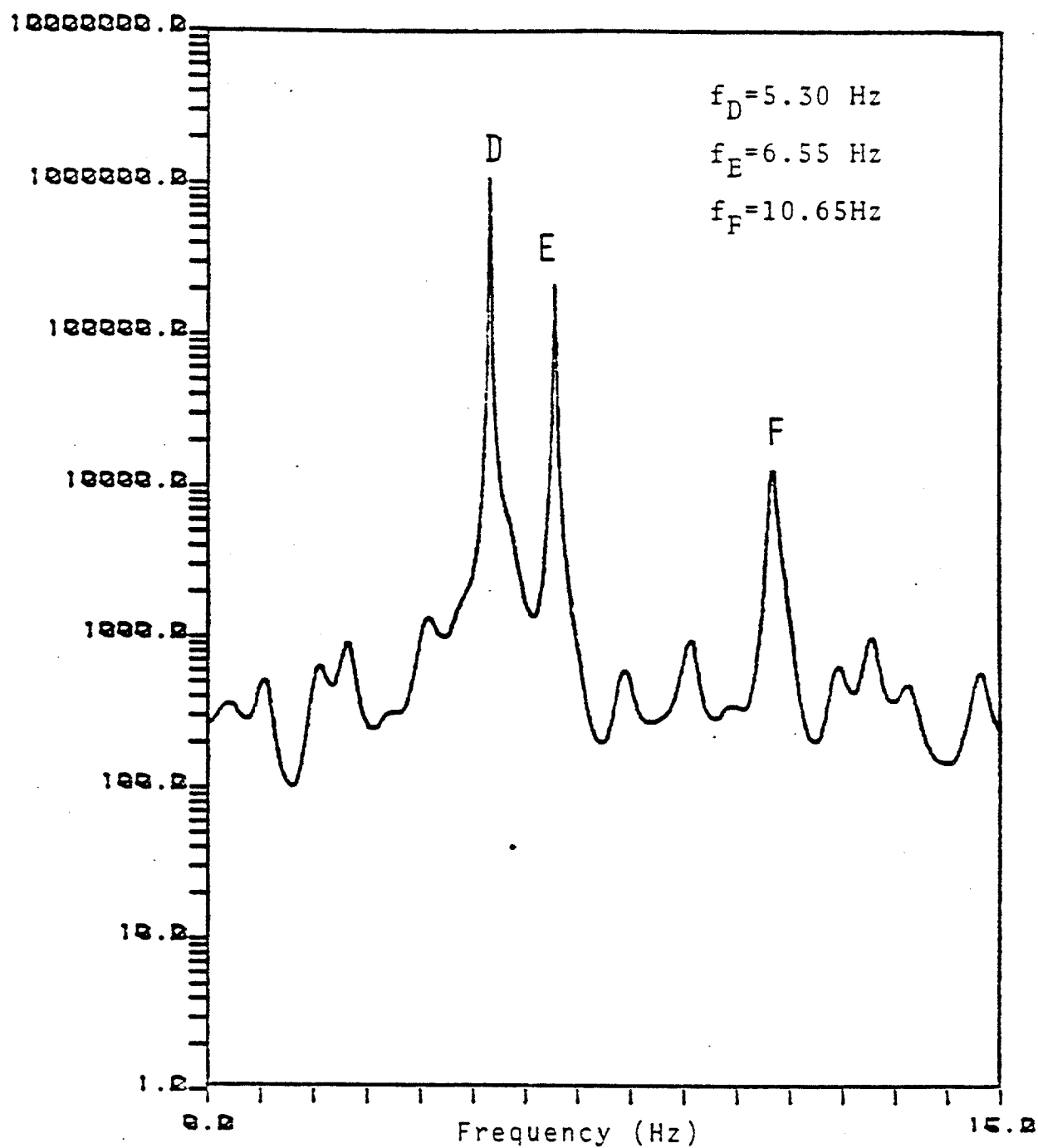


5-16 Cross-Bicoherence Between Cross-Flow and In-Line Responses in Figure 5-12 and 5-13 at Non-lock-in

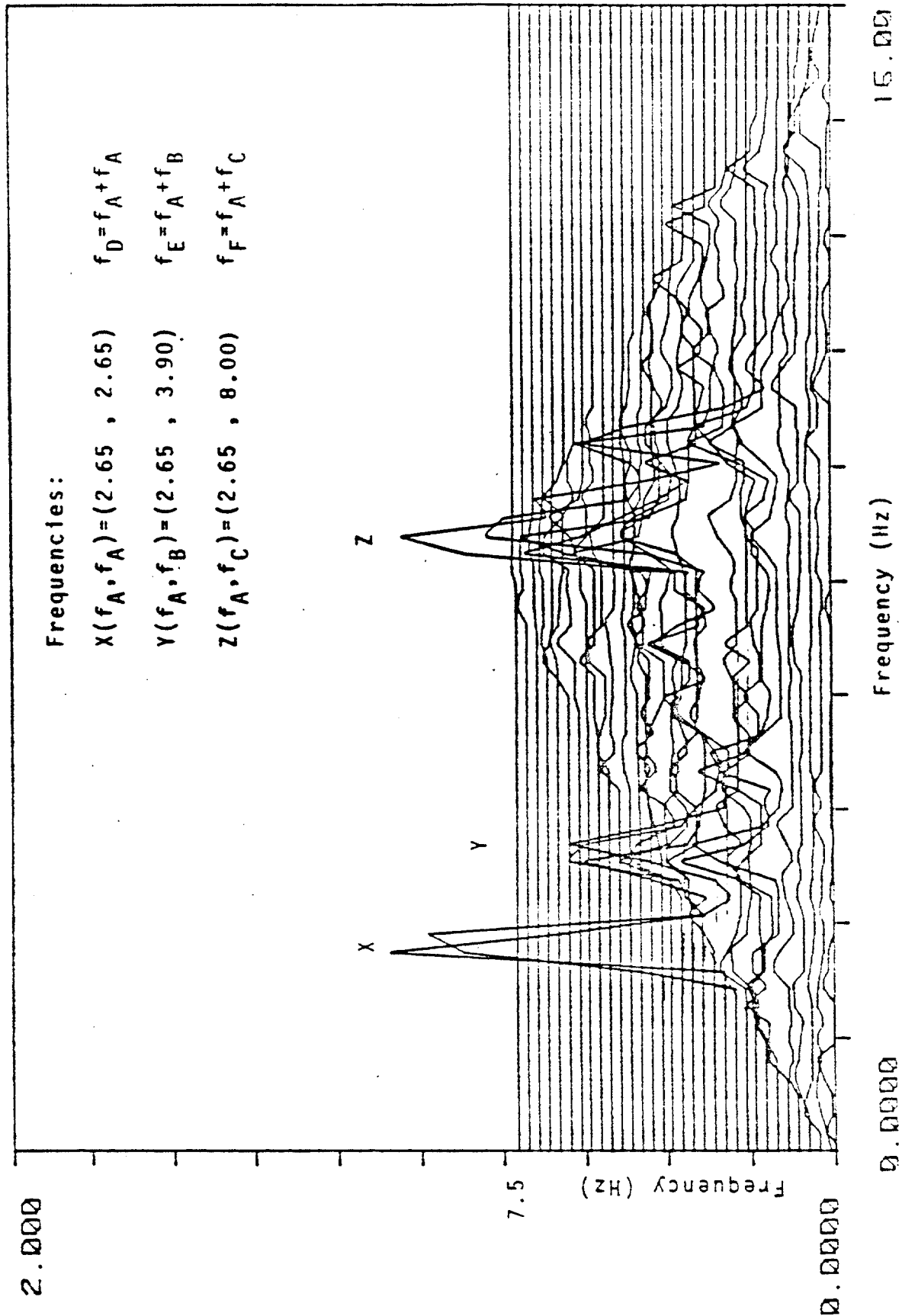




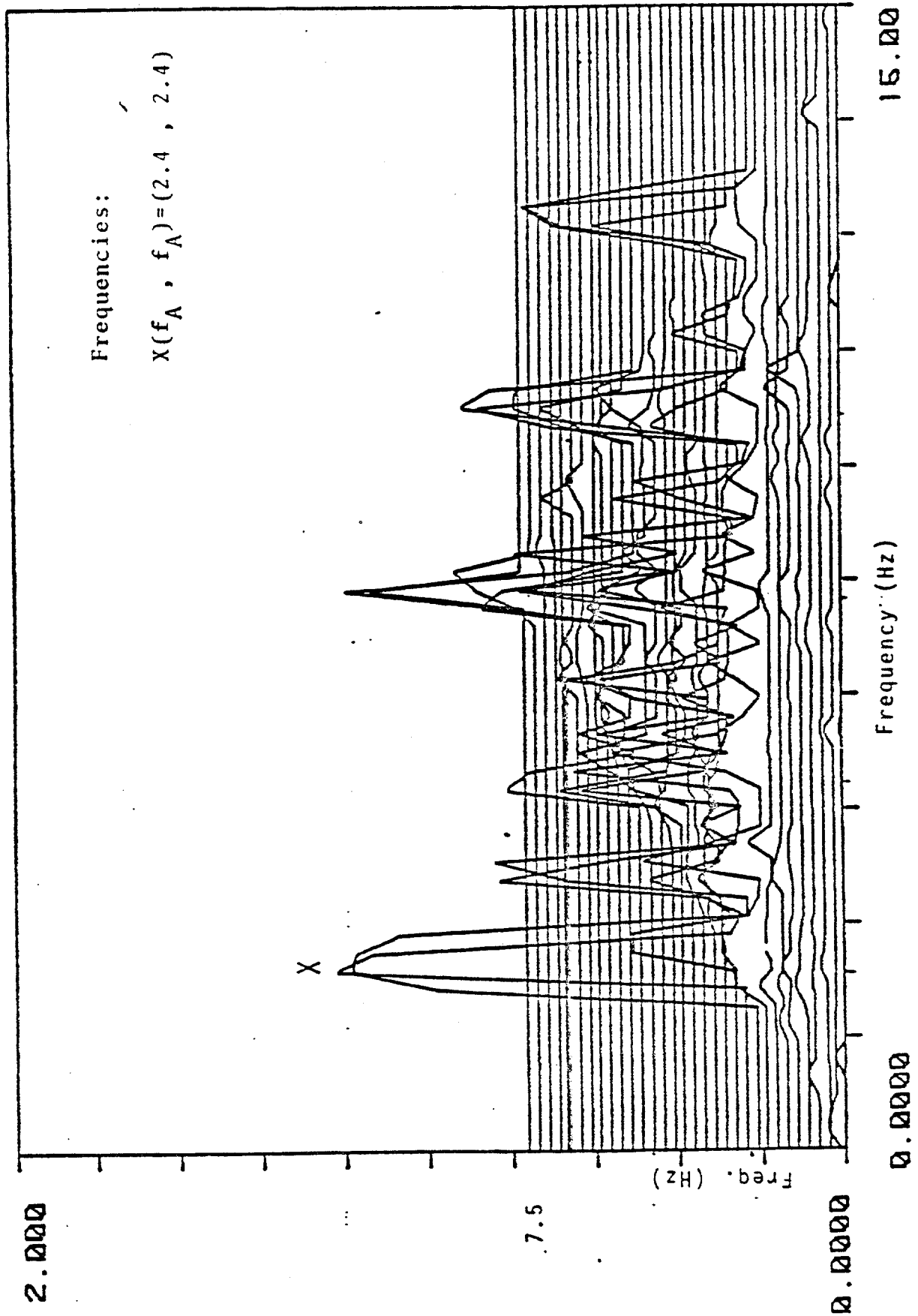
5-17 Power Spectrum of Cross-Flow Response at Near-lock-in



5-18 Power Spectrum of In-Line Response at Near-lock-in



5-19 Cross-Coherence between Cross-Flow and In-Line Responses in Figures 5-17 and 5-18 at Near-lock-In



5-20 Cross-Bicoherence Between Cross-Flow and In-Line Responses in Figures 5-14 and 5-15 at Lock-in

correlation between components, as proved by the peaks in the cross-bicoherence spectrum  $b_{xy}(W_1, W_2)$ .

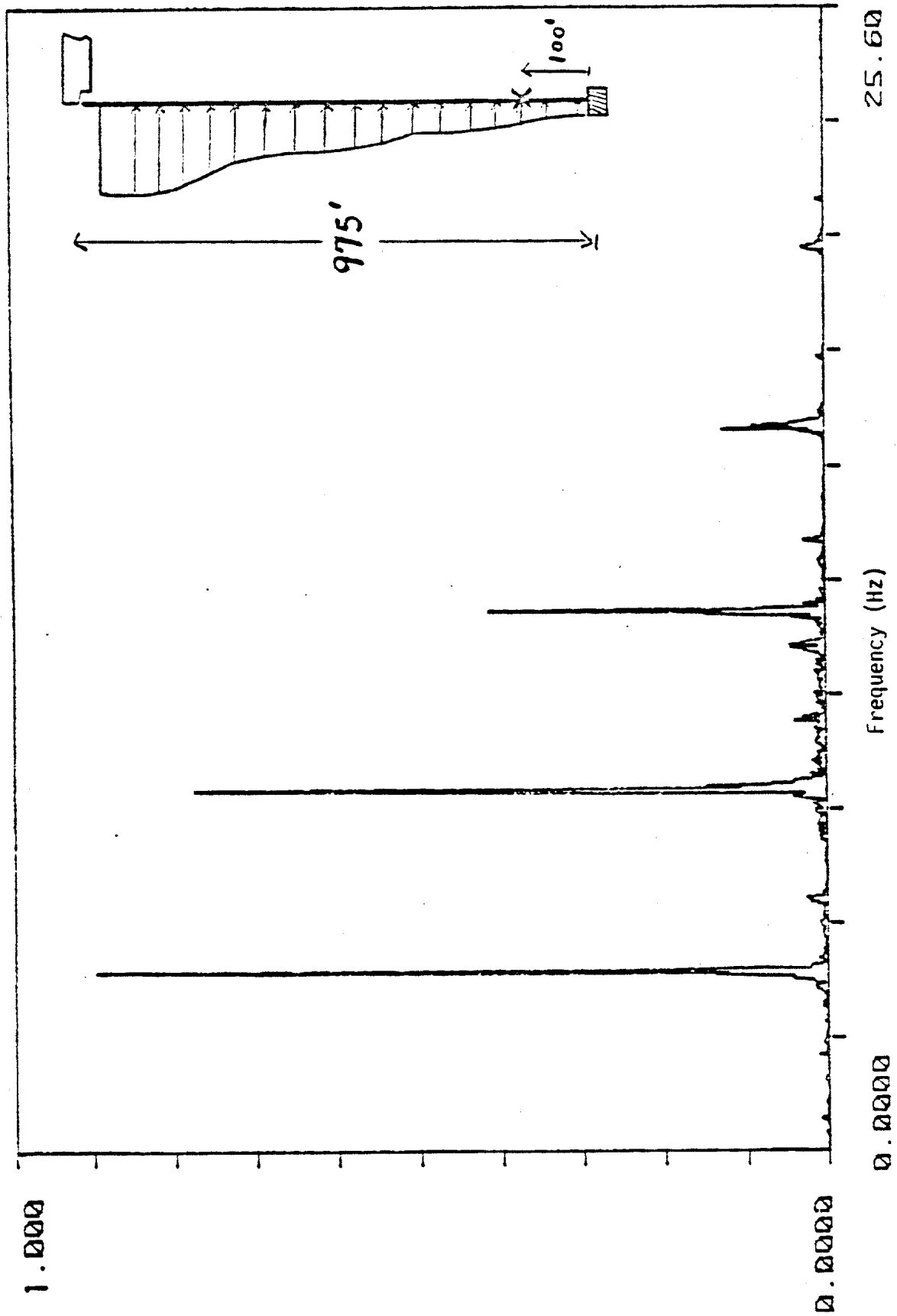
For the lock-in case, the cross-flow and in-line power spectra are shown in figure 5-14 and 5-15. The cross-bicoherence spectrum  $b_{xy}(W_1, W_2)$  in figure 5-20 shows a peak at  $b_{xy}(2.4, 2.4)$  which implies that the frequency doubling property at lock-in is also due to the quadratic correlation between these two direction responses.

The above results of bispectral analysis provided strong evidence of the existence of the quadratic correlation between cross-flow and in-line response for both lock-in and non-lock-in cases. This implies that the relation can be modelled by a second order nonlinear system. The quadratic system identification techniques will be discussed in the next chapter.

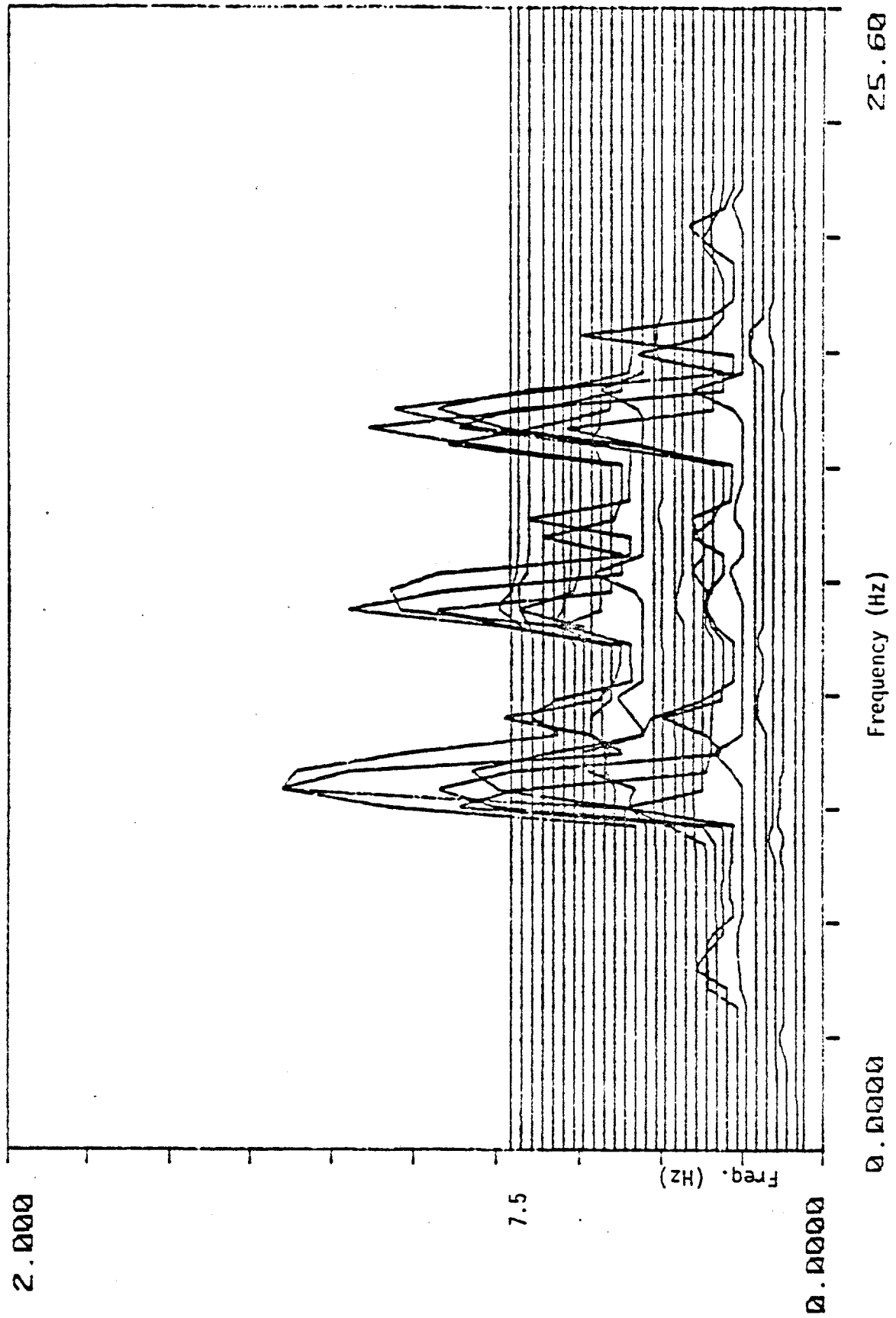
The results shown so far are from the Castine experimental data in which the incident current speed was uniform along the cylinder. Next, the bispectral analysis results of an Arctic experiment conducted by Vandiver and Kim in 1983 for the shear flow case are shown to check for quadratic correlation under the shear flow conditions.

The test cable, 975 feet in length, was suspended vertically from a research vessel with a heavy weight at the

bottom end. An accelerometer was located at 100 feet from the bottom end of the cable. The uni-directional measured response, was orientated at an unknown angle, contained both in-line and cross-flow responses in it. Figure 5-21 shows the power spectrum of the measured response in which the frequency summing property was observed. Again, the cross-bicoherence spectrum between cross-flow and in-line components as shown in figure 5-22 indicated the existence of quadratic correlation for the shear flow case.



5-21 Power Spectrum of the Measured Response of Arctic Experiment



5-22 Auto-Bicoherence of the Response in Figure 5-21



## CHAPTER 6

### QUADRATIC SYSTEM IDENTIFICATION AT LOCK-IN

From the bispectral analysis, we concluded that there exists a quadratic correlation between cross-flow and in-line response for both lock-in and non-lock-in cases. These results also explained why the in-line response frequencies are not corresponding to the natural frequencies of the cylinder. However, it is still not known if even higher order nonlinearities exist in the relationship. Due to the limitation of computer memory, it is difficult to carry out a higher than third order spectral analysis. In the following chapters, it is proposed to model the relationship between cross-flow and in-line responses with a second order nonlinear system which includes a linear term and quadratic term; also an error term is introduced to represent any error associated with the imperfection of the model which might be due to the existence of the higher order nonlinearities in the relationship. The linear and quadratic systems are then identified. The resulting error term ( or residual ) then enables us to evaluate the contribution to the relationship, resulting from higher order nonlinearities. Also from these identified linear and quadratic systems, the in-line response can be decomposed into linear and quadratic responses due to linear and quadratic correlation respectively with the cross-flow

response. In this chapter, a time domain multiple regression method is derived to identify the linear and quadratic systems for the lock-in case. The decomposed linear and quadratic in-line responses are presented.

### 6.1 Application of Multiple Regression Analysis

Let the input  $x(t)$ , the cross-flow response, and output  $y(t)$ , the in-line response, be related by a second order system,

$$y(t) = y_0 + \sum_{u=0}^{k-1} h(u)x(t-u) + \sum_{u=0}^{M-1} \sum_{v=0}^{M-1} g(u,v)x(t-u)x(t-v) + n(t) \quad (6.1.1)$$

where  $n(t)$  is the error term,  $h(u)$  is the linear impulse response function and  $g(u,v)$  is the second order impulse response kernel. Given the measured input and output data,  $x(t)$  and  $y(t)$   $t=1,2,\dots,(N+K-1)$ , the system functions  $h(u)$  and  $g(u,v)$  are to be determined in such a way that the estimated mean square error (MSE) is minimized. It was further assumed without loss of generality that the second order impulse response kernel is symmetrical in its arguments:

$$g(u,v) = g(v,u) \quad (6.1.2a)$$

and thus

$$G(W_1, W_2) = G(W_2, W_1) \quad (6.1.2b)$$

Consequently, the quadratic transfer function is symmetric about the line  $W_1=W_2$  in the bi-frequency plane. Equation (6.1.1) can then be rewritten in matrix form as:

$$\{y\}=\{y_0\}+[x]\{h\}+[z]\{G\}+\{n\} \quad (6.1.3)$$

where

unknowns  $h(u) \quad n=0,1,\dots,K-1$

unknowns  $g(u,v) \quad u=0,1,\dots,M-1 \quad v=0,1,\dots,M-1$

$NN=N+K-1$  ,  $MM=M(M+1)/2$

$z(t,w)=x(t-u)x(t-v)$  with  $w=v+M*u-u(u+1)/2$

$G(w)=\begin{cases} g(u,v) & \text{if } u=v \\ 2g(u,v) & \text{if } u \neq v \end{cases}$  with  $w=v+M*u-u(u+1)/2$

$\{h\}=\{h(0),h(1),\dots,h(K-1)\}^T$   $K \times 1$  vector

$\{y\}=\{y(K),y(K+1),\dots,y(NN)\}^T$   $N \times 1$  vector

$\{n\}=\{n(K),n(K+1),\dots,n(NN)\}^T$   $N \times 1$  vector

$\{y_0\}=\{y_0,y_0,\dots,y_0\}^T$   $N \times 1$  vector

$\{G\}=\{G(0),G(1),\dots,G(MM-1)\}^T$   $MM \times 1$  vector

$$[x]=\begin{bmatrix} x(K) & x(K-1) & x(K-2) & \dots & x(1) \\ x(K+1) & x(K+2) & x(K+3) & \dots & x(2) \\ \vdots & \vdots & \vdots & \ddots & \vdots \\ x(N+K-1) & x(N+K-2) & \dots & \dots & x(N) \end{bmatrix} \quad N \times K \text{ matrix}$$

$$[z]=\begin{bmatrix} z(K,0) & z(K,1) & \dots & z(K,MM-1) \\ z(K+1,0) & z(K+1,1) & \dots & z(K+1,MM-1) \\ \vdots & \vdots & \ddots & \vdots \\ z(K+N-1,0) & z(K+N-1,1) & \dots & z(K+N-1,MM-1) \end{bmatrix} \quad N \times MM \text{ matrix}$$

the MSE can be written as

$$\begin{aligned}
 \text{MSE} &= \{n\}^T \{n\} = (\{y\} - \{y_0\} - [x]\{h\} - [z]\{G\})^T (\{y\} - \{y_0\} - [x]\{h\} - [z]\{G\}) \\
 &= \{y\}^T \{y\} - 2\{h\}^T [x]^T \{y\} - 2\{G\}^T [z]^T \{y\} + 2\{h\}^T [x]^T [z]^T \{G\} + \{h\}^T [x]^T [x]\{h\} \\
 &\quad + \{G\}^T [z]^T [z]\{G\} - \{y_0\}^T (\{y\} - [x]\{h\} - [z]\{G\}) \\
 &\quad - (\{y\}^T - \{h\}^T [x]^T - \{G\}^T [z]^T) \{y_0\} + \{y_0\}^T \{y_0\}
 \end{aligned} \tag{6.1.4}$$

let  $\partial \text{MSE} / \partial y_0 = 0$ , we obtain

$$N \{y_0\} + \{I\}^T [x]\{h\} + \{I\}^T [z]\{G\} = \{I\}^T \{y\} \tag{6.1.5}$$

let  $\partial \text{MSE} / \partial h_i = 0$ , we obtain

$$([x]^T [z])\{G\} + ([x]^T [x])\{h\} + y_0 [x]^T \{I\} = [x]^T \{y\} \tag{6.1.6}$$

let  $\partial \text{MSE} / \partial G_i = 0$ , we obtain

$$([z]^T [x])\{h\} + ([z]^T [z])\{G\} + y_0 [z]^T \{I\} = [z]^T \{y\} \tag{6.1.7}$$

These three equations can be combined and rewritten as

$$\begin{bmatrix} [M1] & [C] & \{Q1\}^T \\ [C]^T & [M2] & \{Q2\}^T \\ \{Q1\} & \{Q2\} & N \end{bmatrix} \begin{bmatrix} \{h\} \\ \{G\} \\ y_0 \end{bmatrix} = \begin{bmatrix} \{R1\} \\ \{R2\} \\ R_0 \end{bmatrix} \tag{6.1.8}$$

where

$$R_0 = \{I\}^T \{y\} = \text{constant}$$

$$\{R1\} = \{x\}\{y\} = K \times 1 \text{ vector}$$

$$\{R2\} = \{z\}\{y\} = MM \times 1 \text{ vector}$$

$$\{Q1\} = \{I\}^T \{x\} = 1 \times K \text{ vector}$$

$$\{Q2\} = \{I\}^T \{z\} = 1 \times MM \text{ vector}$$

$$[M1] = \{x\}\{x\} = K \times K \text{ matrix}$$

$$[M2] = \{z\}\{z\} = MM \times MM \text{ matrix}$$

$$[C] = \{x\}\{z\} = K \times MM \text{ matrix}$$

For a specified order K and M, the system function  $h(u)$  and  $g(u,v)$  can be obtained by solving the set of linear equations (6.1.8) with  $x(t)$  and  $y(t)$  being the cross-flow and in-line responses respectively. From these identified system functions  $h(u)$  and  $g(u,v)$ , the error  $n(t)$  can then be calculated by equation (6.1.1) with input  $x(t)$  being the cross-flow response. Finally we obtain the simulated in-line response  $y_s(t)$ , and error  $n(t)$ . Consequently, we are now able to decompose the in-line response into the linear response  $y_1(t)$ , and quadratic response  $y_2(t)$  as follows,

$$n(t) = y(t) - y_s(t)$$

$$y_s(t) = y_0 + y_1(t) + y_2(t)$$

$$y_1(t) = \sum_{u=0}^{K-1} h(u)x(t-u)$$

(6.1.9)

$$y_2(t) = \sum_{u=0}^{M-1} \sum_{v=0}^{M-1} g(u,v)x(t-u)x(t-v) + y_0$$

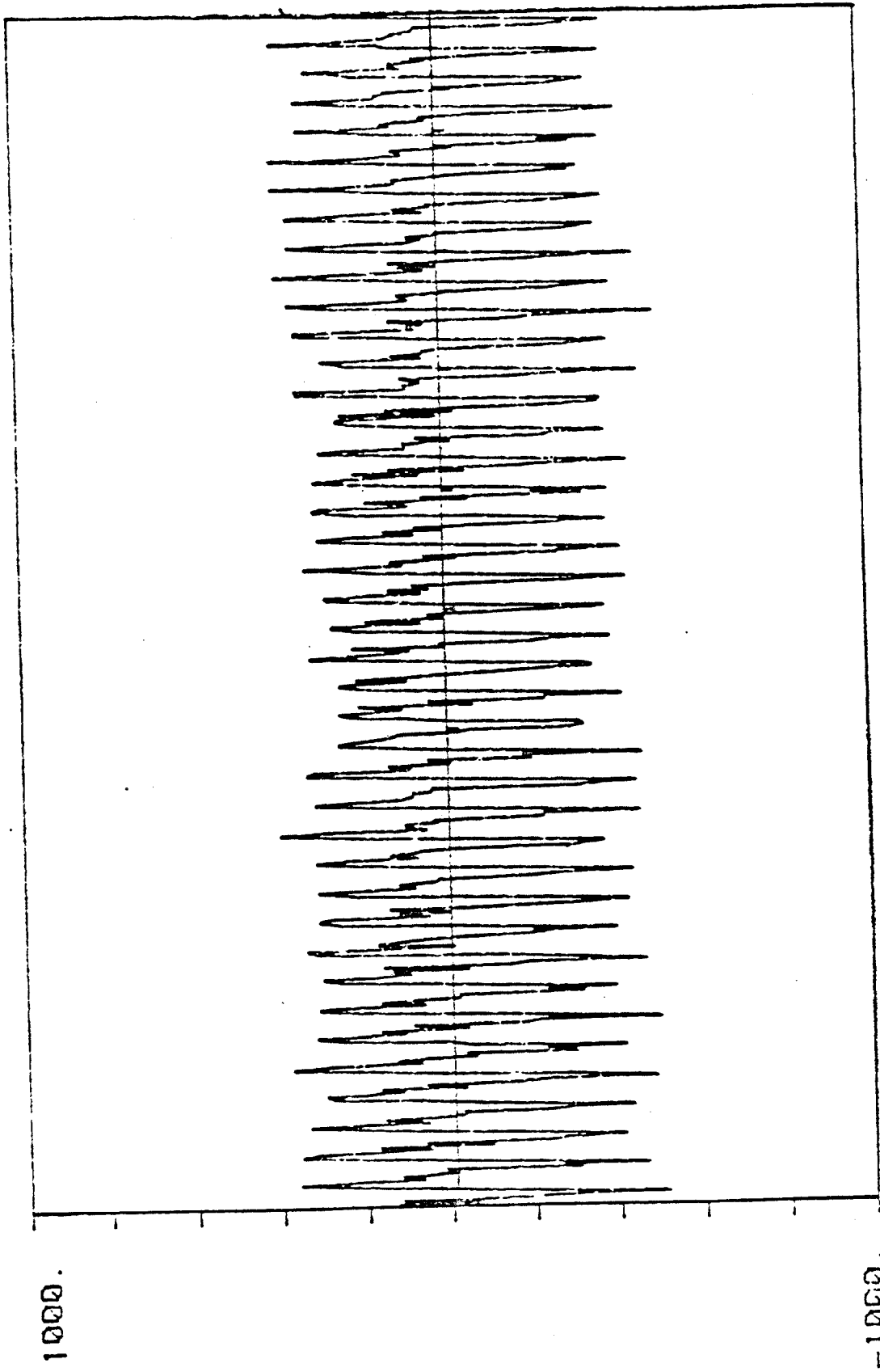
## 6.2 Linear and Quadratic In-line Responses

In this section, typical lock-in response data were analyzed by using the time domain multiple regression method described in the last section. Figures 6-1 and 6-2 show the input  $x(t)$  ( cross- flow ) and output  $y(t)$  ( in-line ) for the lock-in case. Figure 6-3 shows the scatter diagram of  $x(t)$  vs.  $y(t)$  which has a figure eight pattern. These two given time series were applied to equation (6.1.1) to calculate the system function  $h(t)$  and  $g(u,v)$  from which the error  $n(t)$  was then obtained. By increasing the order  $K$  and  $M$ , a convergent MSE was reached. Figure 6-4 shows the error time series  $n(t)$  for  $K=30$  and  $M=9$ . The error  $n(t)$  is a wide-band noise as shown by its spectrum in Figure 6-5 and the ratio between the MSE and the variance of in-line response is 2.6%. This small amount of error implied that the higher order nonlinearities ( higher than second order ) are negligible in the relationship for the lock-in case and the second order nonlinear system is a reasonable model to relate the cross-flow and in-line response.

From equation (6.1.9b), the simulated in-line response  $y_s(t)$  was obtained as shown in figure 6-6 which is in good agreement with the real in-line response  $y(t)$ . This agreement is easier to visualize by comparing the scatter diagram of cross-flow response  $x(t)$  vs. simulated in-line

response  $y_s(t)$  shown in figure 6-7 to the real one in Figure 6-3. The linear and quadratic in-line response  $y_1(t)$  and  $y_2(t)$  calculated from equations (6.1.9c—9d) are shown in figure 6-8 and 6-9. The scatter diagram of  $x(t)$  vs.  $y_1(t)$  and  $x(t)$  vs.  $y_2(t)$  in figure 6-10 and 6-11 show that the linear in-line response and quadratic in-line response contribute quite different patterns to the total in-line response.

When the multiple regression method was applied to the non-lock-in case, the rate of convergence was much slower than that of lock-in case and became inefficient due to the required larger order of  $K$  and  $M$ . The reason for the slower convergence is that at lock-in, the response time series are quite deterministic. As a result, only a little past information is required to predict the present response, while the responses at non-lock-in are much more random than the lock-in responses which leads to the requirement of a higher order of  $K$  and  $M$  in equation (6.1.1). The quadratic system identification for the non-lock-in case will be discussed in the next chapter.



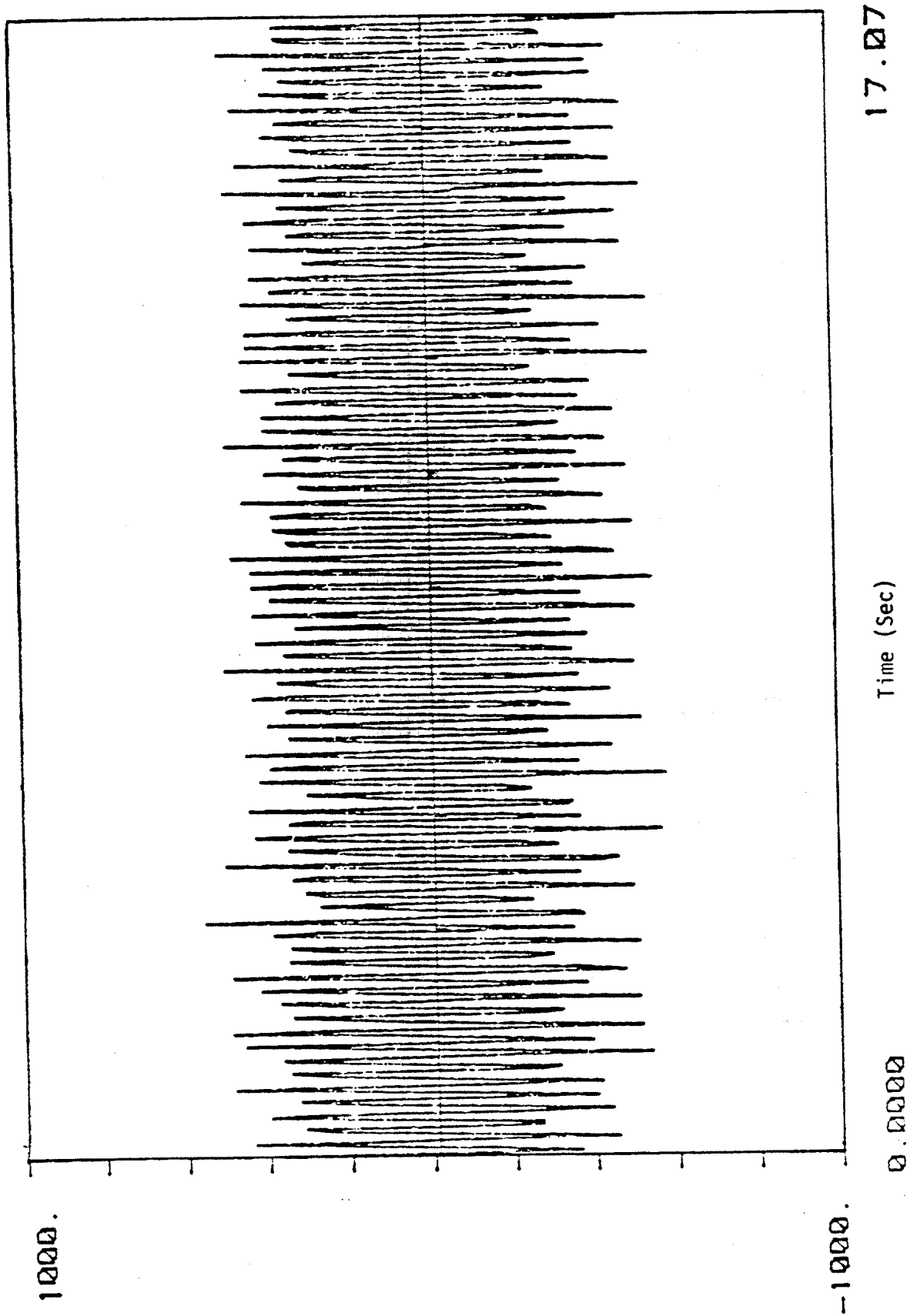
17.07

Time (Sec)

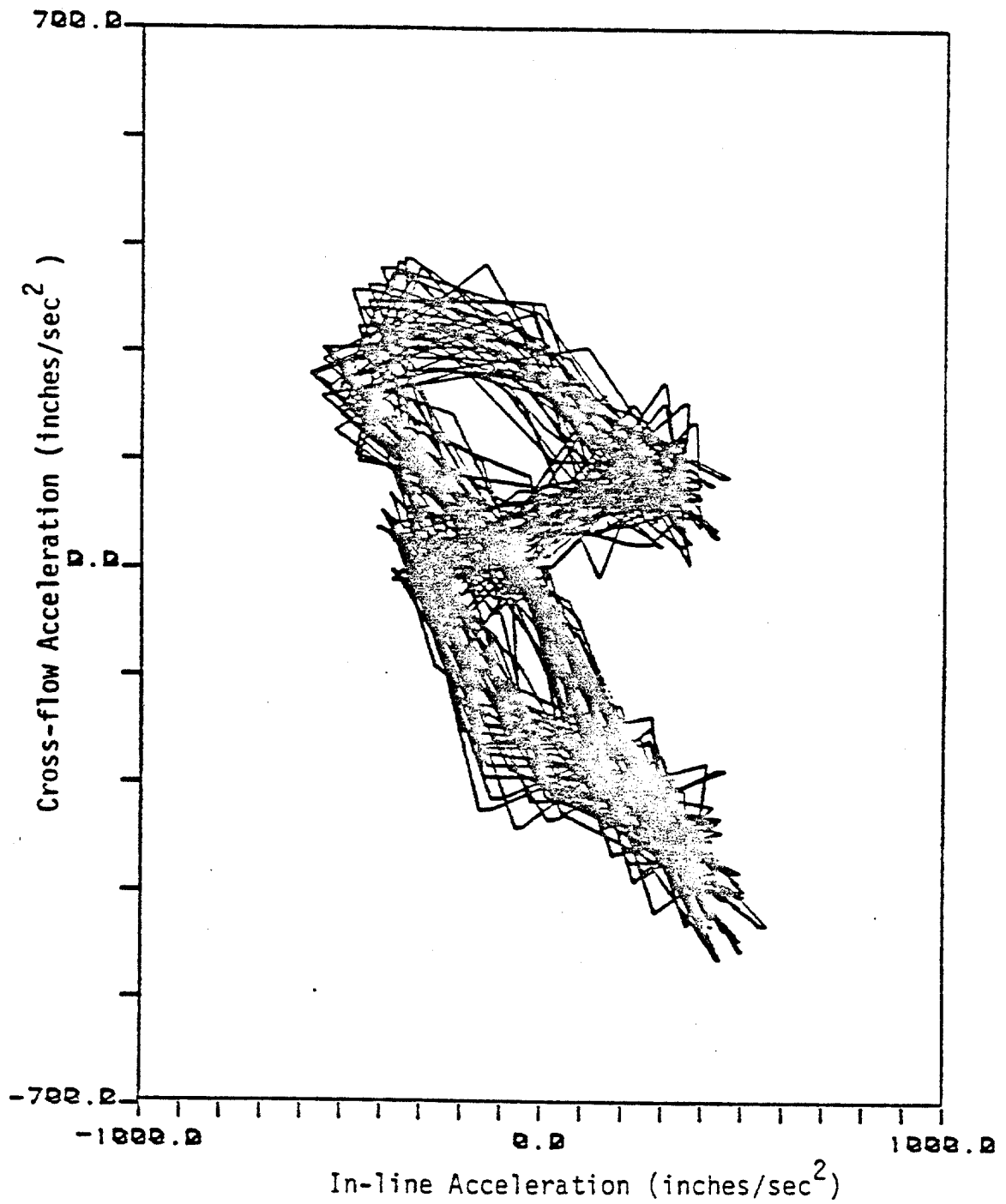
0.0000

6-1 Cross-Flow Acceleration at Lock-in

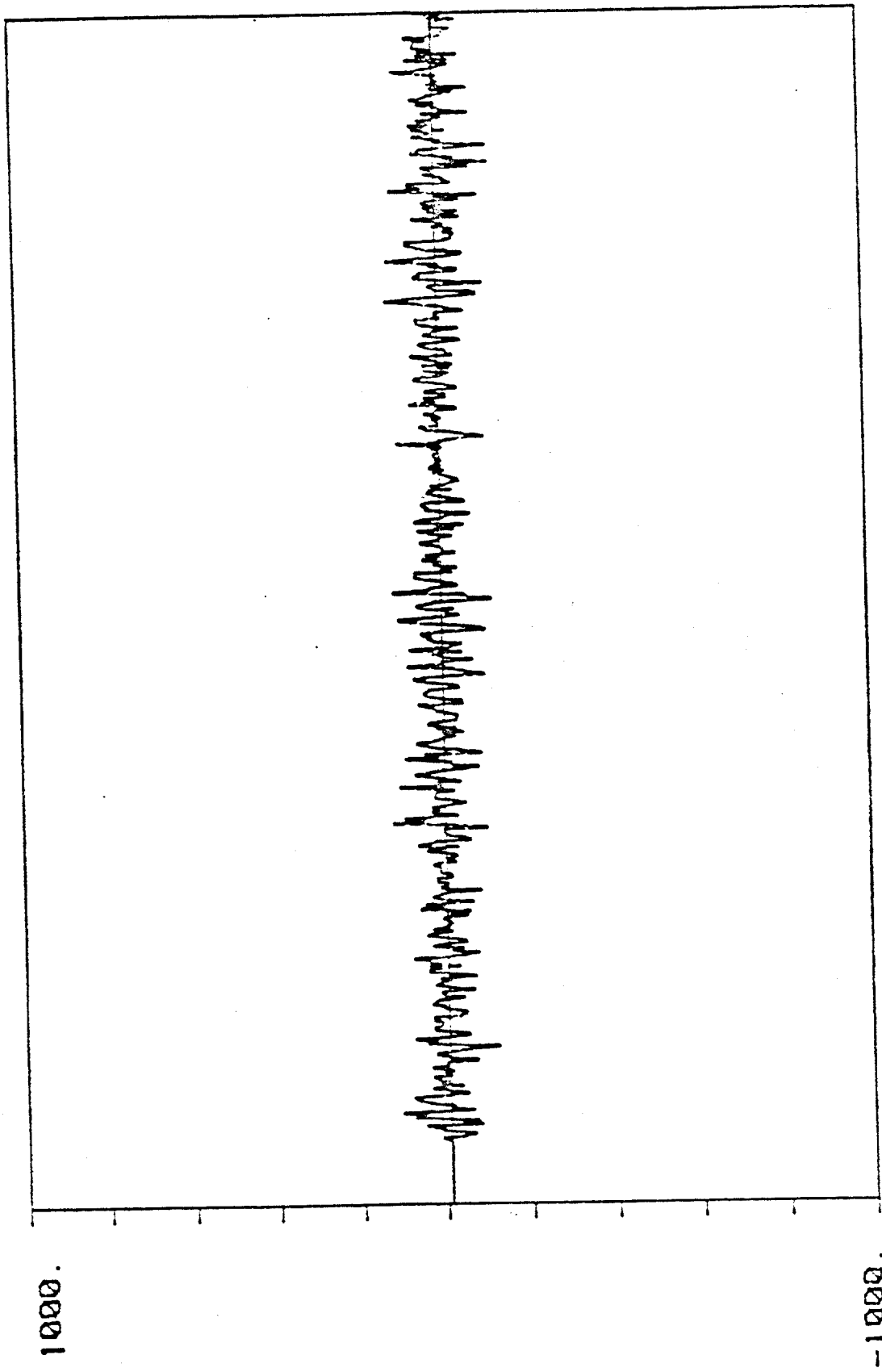




6-2 In-Line Acceleration at Lock-in

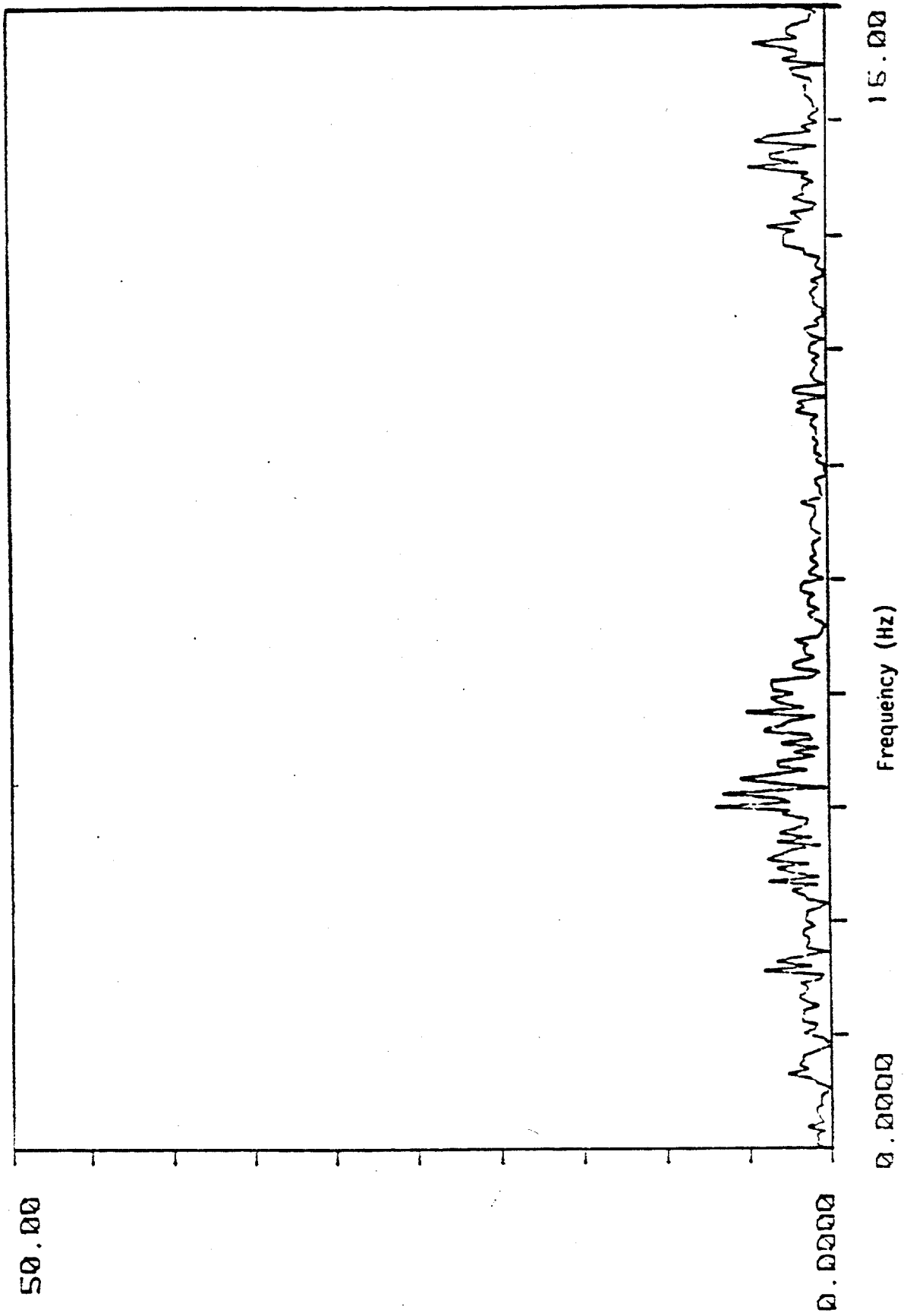


6-3 Two-Dimensional Motion Time History of Cross-Flow vs. In-Line Acceleration in Figures 6-1 and 6-2 at Lock-in

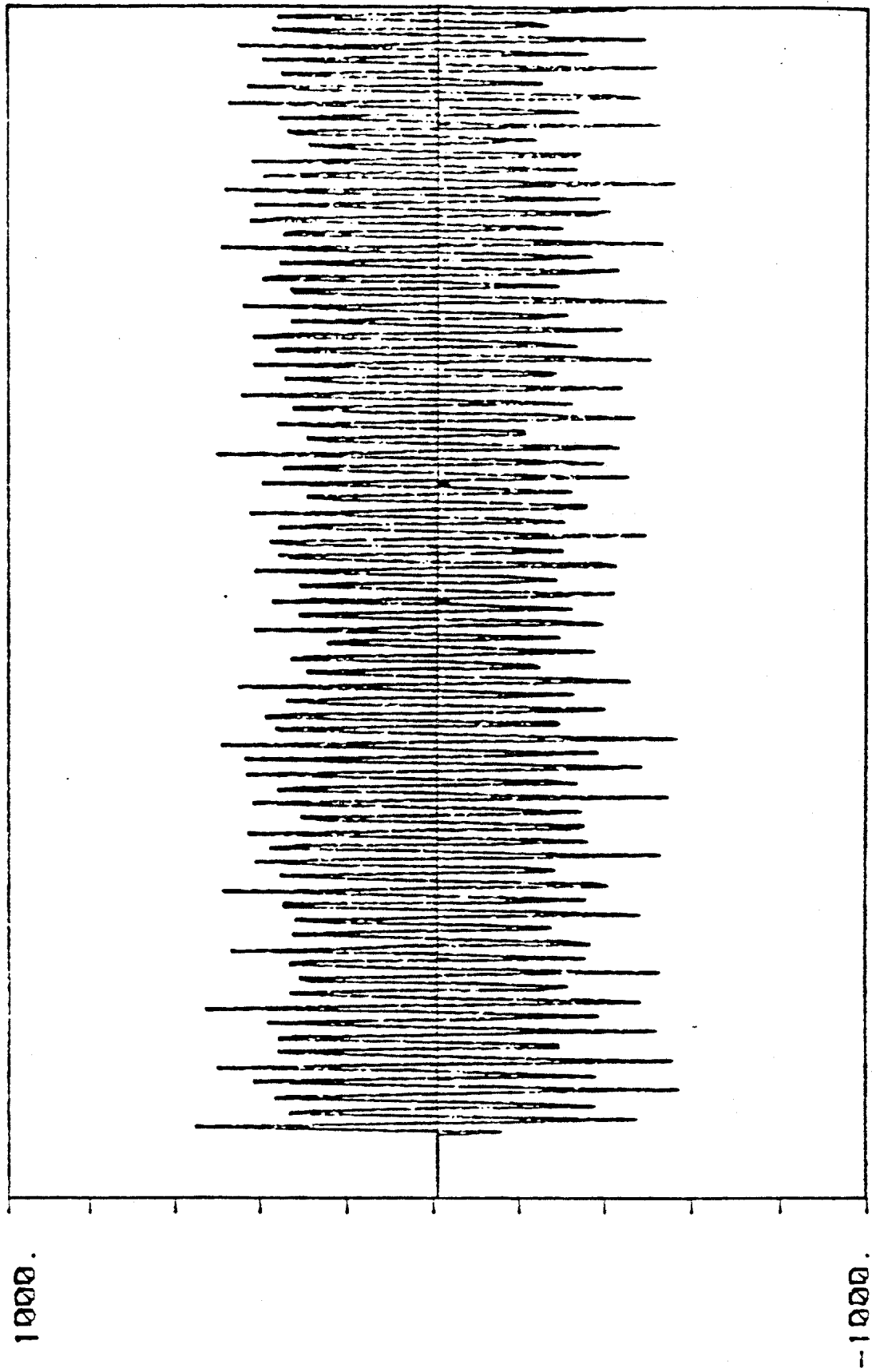


Time (Sec)

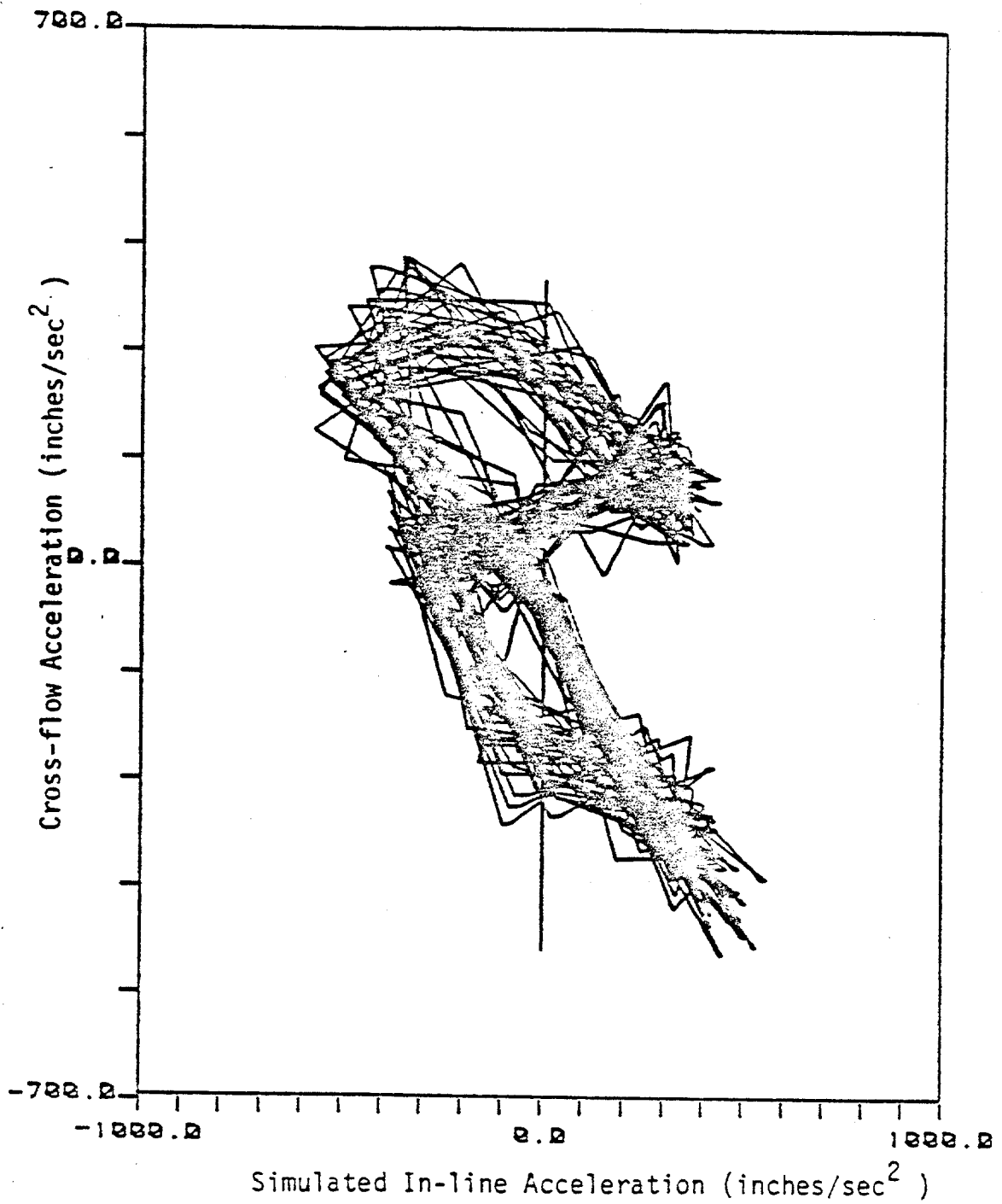
6-4 Residual Time History



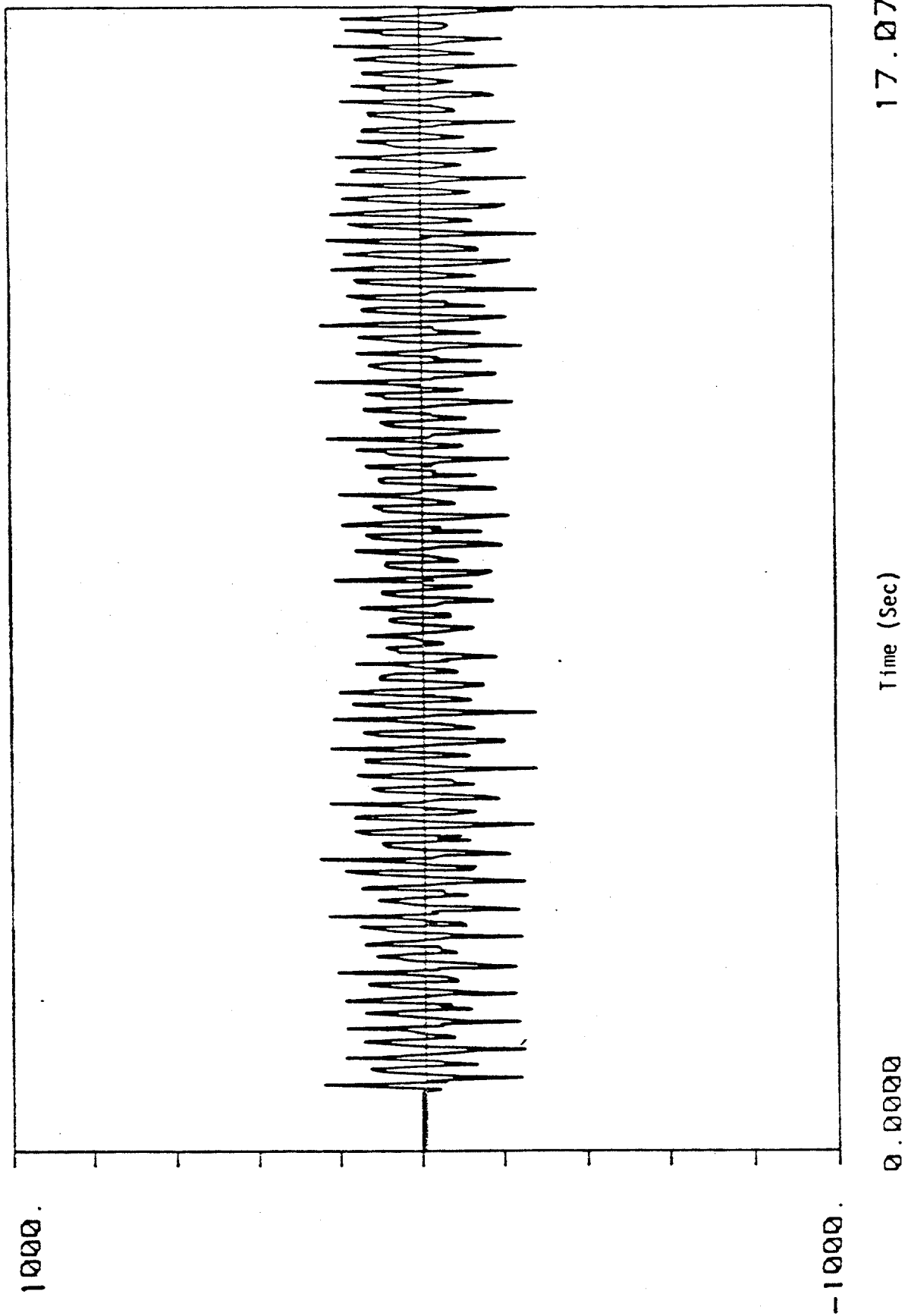
6-5 Power Spectrum of the Residual in Figure 6-4



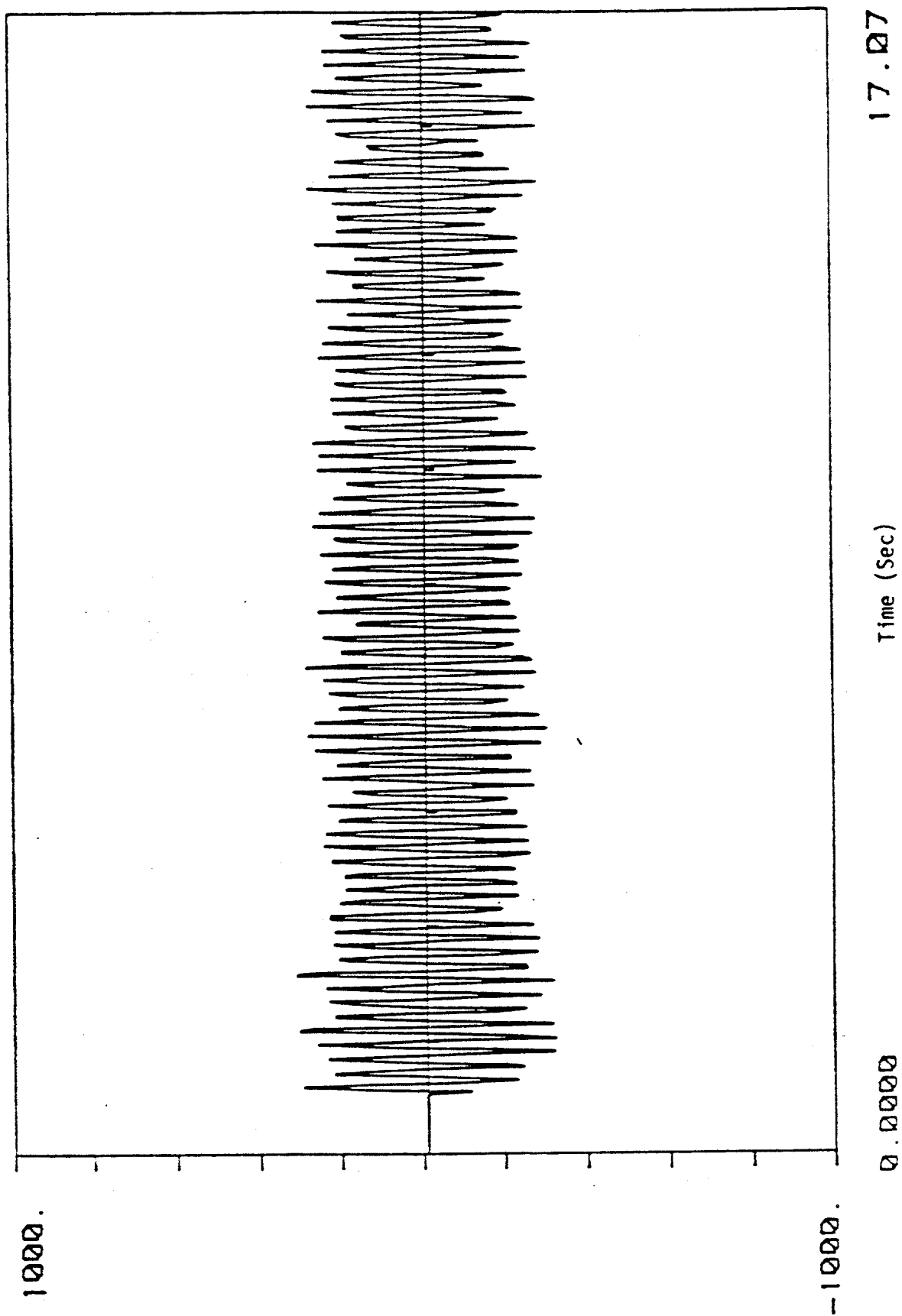
6-6 Simulated In-Line Acceleration (Comparing to Figure 6-2)



6-7 Two-Dimensional Motion Time History of Cross-Flow  
vs. Simulated In-Line Acceleration. (Comparing to Figure 6-3)

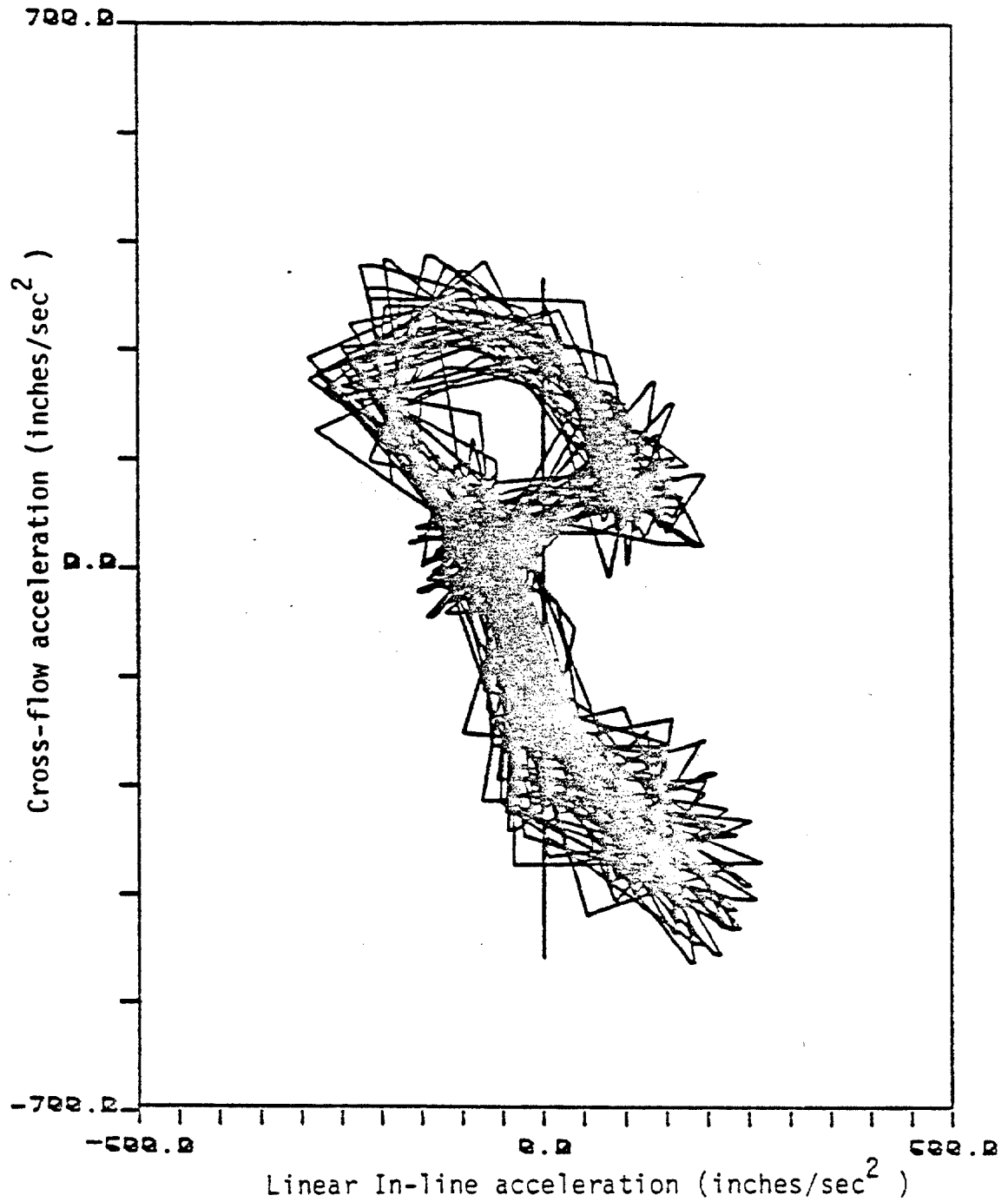


6-8 In-Line Acceleration Component Due to Linear Correlation

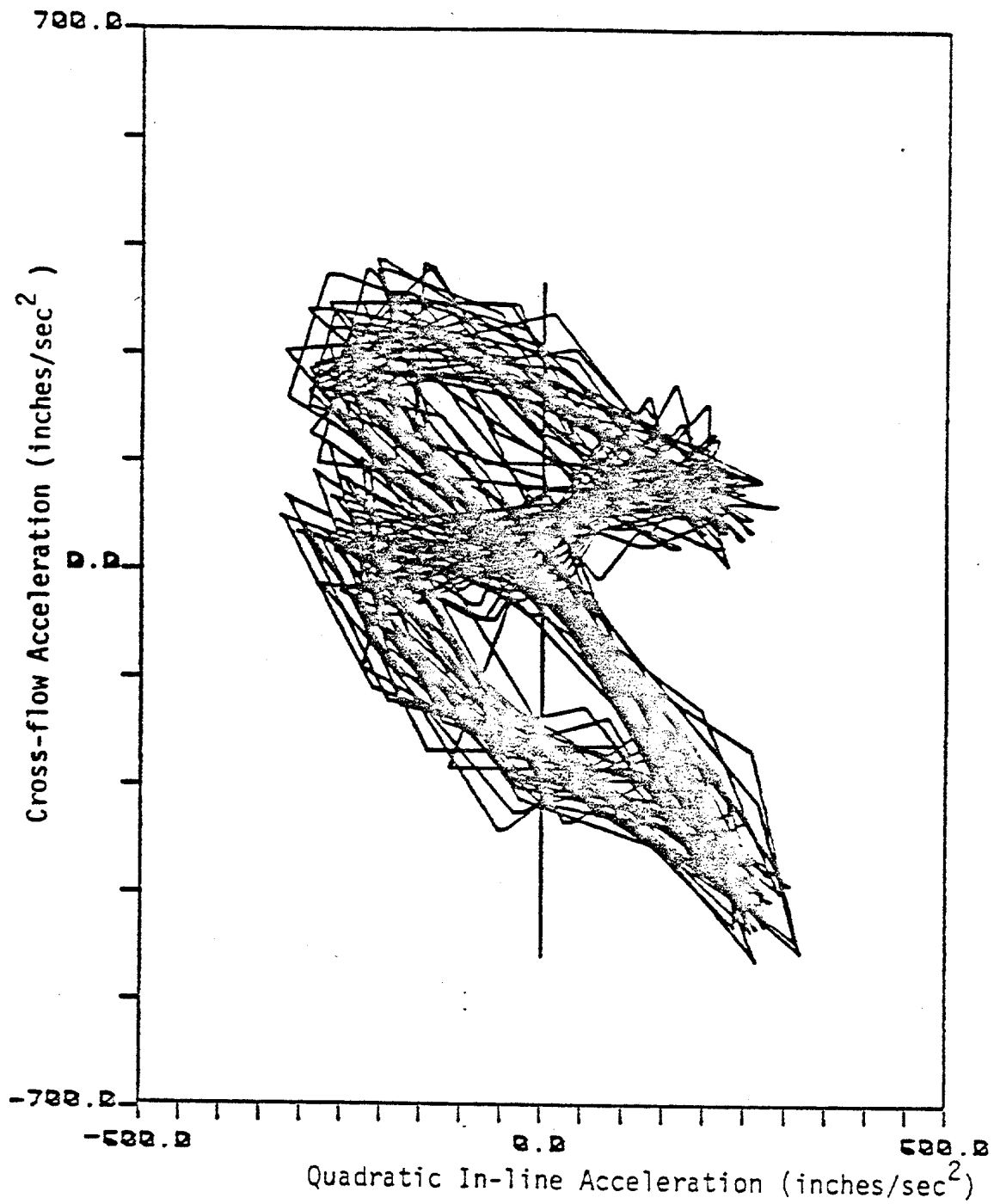


6-9 In-line Acceleration Component Due to Quadratic Correlation





6-10 Two-Dimensional Motion Time History of Cross-Flow  
vs. Linear In-Line Acceleration ( Fig. 6-1 vs. 6-8 )



6-11 Two-Dimensional Motion Time History of Cross-Flow  
vs. Quadratic In-Line Acceleration ( Fig. 6-1 vs. 6-9 )

## CHAPTER 7

### QUADRATIC SYSTEM IDENTIFICATION AT NON-LOCK-IN

In this chapter a frequency domain least squares method for the quadratic system identification will be discussed first for the non-lock-in case, then a quadratic model involving a square law system proposed by Bendat and Piersol [2] is used to identify the system. The remaining residual after the quadratic system is identified is examined to check the existence of higher order nonlinearities in the relationship. A linear coherence spectrum between the in-line response and the square of cross-flow response is presented which provides additional evidence of the existence of quadratic correlation between in-line and cross-flow response.

#### 7.1 Least Squares Quadratic System Identification

A frequency domain quadratic system identification method with the input a stationary Gaussian random process has been used by several other researchers. The method will then be applied to the non-lock-in response data to obtain the quadratic transfer function.

The input and output of a quadratic system is expressed as:

$$y(t) = \sum_u h(u)x(t-u) + \sum_u \sum_v g(u,v)x(t-u)x(t-v) + n(t) \quad (7.1.1)$$

where  $n(t)$  denotes any error associated with the imperfection of the model or noise in the system. Here, a linear term was still included even though the in-line and cross-flow response are almost linearly independent as discussed in section 3.6 for non-lock-in case. The system transfer functions  $H(W)$  and  $G(W_1, W_2)$ , are determined such that the mean square error, MSE, of  $n(t)$  is minimized. The MSE can be expressed as,

$$MSE = E[n^2(t)] = E\{[y(t) - \sum_u h(u)x(t-u) - \sum_u \sum_v g(u,v)x(t-u)x(t-v)]^2\} \quad (7.1.2)$$

Let  $[x(t), X(W)]$ ,  $[y(t), Y(W)]$ ,  $[h(u), H(W)]$ ,  $[g(u,v), G(W_1, W_2)]$  be Fourier transform pairs. We find that

$$\begin{aligned} MSE &= E\left\{\left[\sum_{j=-K}^K (Y(W_j) - H(W_j)X(W_j) - \sum_{p+q=j} G(W_p, W_q)X(W_p)X(W_q)) \exp(iW_j t)\right]^2\right\} \\ &= \sum_{j=-K}^K E\{[Y(W_j) - H(W_j)X(W_j) - \sum_{p+q=j} G(W_p, W_q)X(W_p)X(W_q)]^2\} \\ &= \sum_{j=-K}^K E\{[Y(W_j)]^2 + [H(W_j)X(W_j)]^2 - 2H(W_j)X(W_j)Y(W_j) \\ &\quad - \sum_{p+q=j} 2G(W_p, W_q)Y(W_j)X(W_p)X(W_q) + \sum_{p+q=j} H(W_j)G(W_p, W_q)X(W_j)X(W_p)X(W_q) \\ &\quad - \sum_{p+q=j} G(W_p, W_q)Y(W_j)X(W_p)X(W_q) + \sum_{p+q=j} H(W_j)G(W_p, W_q)X(W_j)X(W_p)X(W_q) \\ &\quad + \sum_{p+q=j} \sum_{r+s=j} G(W_p, W_q)G(W_r, W_s)X(W_p)X(W_q)X(W_r)X(W_s)\} \end{aligned} \quad (7.1.3)$$

Let  $\partial MSE / \partial H(W_j) = 0$ , and  $\partial MSE / \partial G(W_m, W_n) = 0$  with  $W_m + W_n = W_j$  for

all  $W_j$ . We obtain

$$H(W_j)E[X(W_j)]^2 = E[X(W_j)Y(W_j)] + \sum_{p+q=j} G(W_p, W_q)E[X(W_j)X(W_p)X(W_q)] \quad (7.1.4)$$

$$E[Y(W_j)X(W_m)X(W_n)] = H(W_j)E[X(W_j)X(W_m)X(W_n)] + \sum_{p+q=j} G(W_p, W_q)E[X(W_p)X(W_q)X(W_m)X(W_n)] \quad (7.1.5)$$

From the following definitions,

$$\begin{aligned} S_{xx}(W_j) &= E[X(W_j)X(-W_j)] \\ S_{xy}(W_j) &= E[X(W_j)Y(-W_j)] \\ B_{xxx}(W_p, W_q) &= E[X(W_p)X(W_q)X(-W_p-W_q)] \\ B_{xxy}(W_m, W_n) &= E[X(W_m)X(W_n)Y(-W_m-W_n)] \end{aligned} \quad (7.1.6)$$

Equations (7.1.4) and (7.1.5) can be rewritten as:

$$H(W_j)S_{xx}(W_j) = S_{yx}(W_j) + \sum_{p+q=j} G(W_p, W_q)B_{xxx}(W_p, W_q) \quad (7.1.7)$$

$$B_{xxy}(W_m, W_n) = H(W_j)B_{xxx}(W_m, W_n) + \sum_{p+q=j} G(W_p, W_q)E[X(W_p)X(W_q)X(W_m)X(W_n)] \quad (7.1.8)$$

From these two equations, we see that the determination of the transfer functions  $H(W)$  and  $G(W_1, W_2)$  required the estimation of the fourth order spectrum, which is difficult, due to computer storage limitations. However, if the input  $x(t)$  is a Gaussian random process, this problem can be

simplified considerably. If  $x(t)$  is a Gaussian random process, the bispectrum  $B_{xxx}(W_m, W_n)$  is zero, and we can write the fourth order cumulant spectrum as:

$$\begin{aligned}
 E[X(W_p)X(W_q)X(W_m)X(W_n)] &= E[X(W_p)X(W_q)]E[X(W_m)X(W_n)] \\
 &+ E[X(W_p)X(W_m)]E[X(W_q)X(W_n)] + E[X(W_p)X(W_n)]E[X(W_q)X(W_m)] \\
 &= \delta(W_p+W_q)\delta(W_n+W_m)S_{xx}(W_p)S_{xx}(W_m) + \delta(W_p-W_m)\delta(W_q-W_n)S_{xx}(W_m)S_{xx}(W_n) \\
 &+ \delta(W_p-W_n)\delta(W_q-W_m)S_{xx}(W_m)S_{xx}(W_n)
 \end{aligned} \tag{7.1.9a}$$

The last term in equation (7.1.8) for nonzero  $W_j$  becomes

$$\sum_{p+q=j} \sum G(W_p, W_q) E[X(W_p)X(W_q)X(W_m)X(W_n)] = 2G(W_m, W_n)S_{xx}(W_m)S_{xx}(W_n) \tag{7.1.9b}$$

Finally we obtain

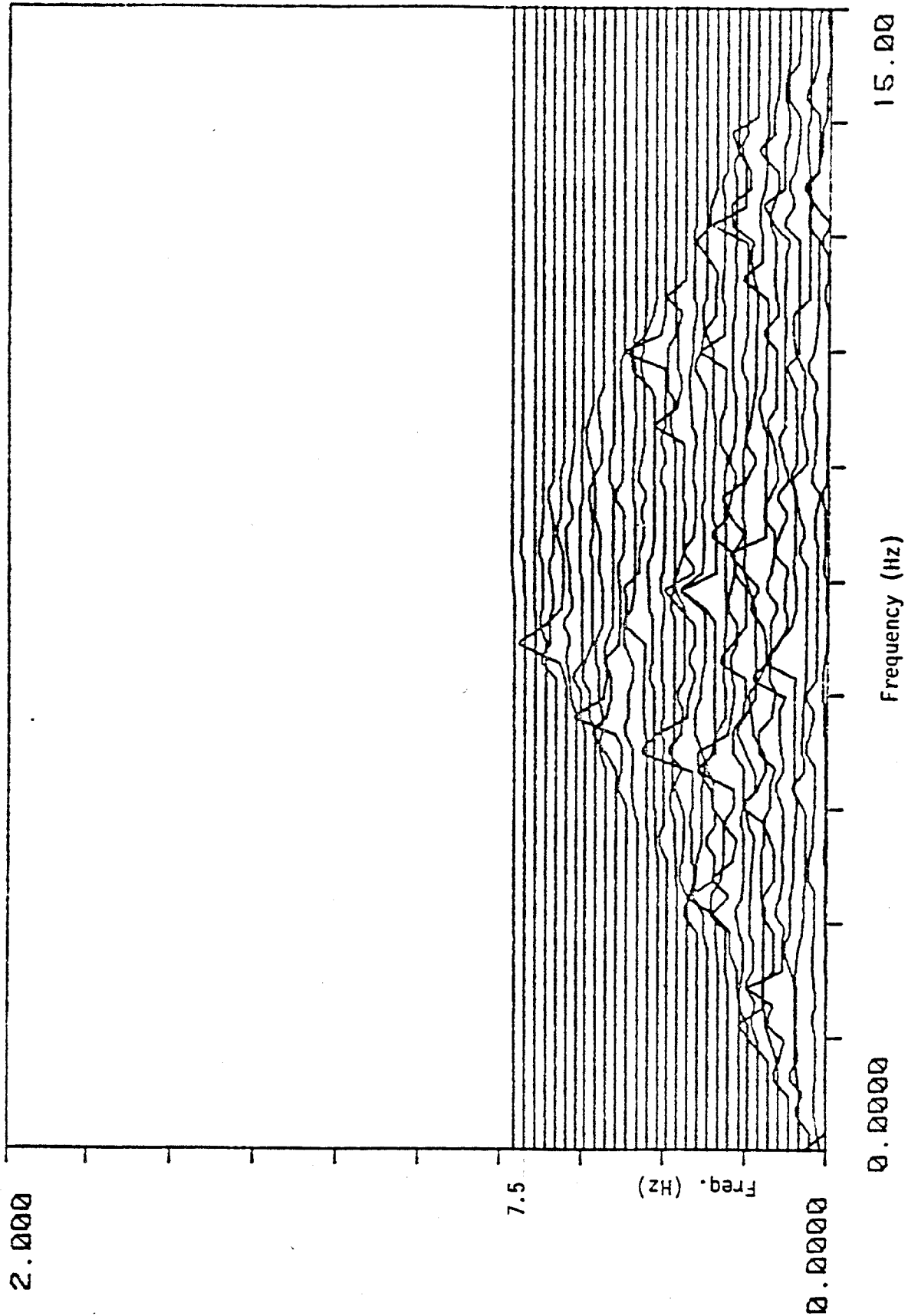
$$H(W) = S_{xy}(W) / S_{xx}(W) \tag{7.1.10}$$

$$G(W_1, W_2) = \frac{B_{xxy}(W_1, W_2)}{2 S_{xx}(W_1)S_{xx}(W_2)} \tag{7.1.11}$$

These two equations can be used to determine the linear and quadratic transfer functions, and only require the estimation of the spectra  $S_{xx}(W)$ ,  $S_{xy}(W)$ , and cross-bispectrum  $B_{xxy}(W_1, W_2)$  for a Gaussian input. It was shown in section 3.6.2 that the non-lock-in cross-flow response can be approximated by a Gaussian random process as

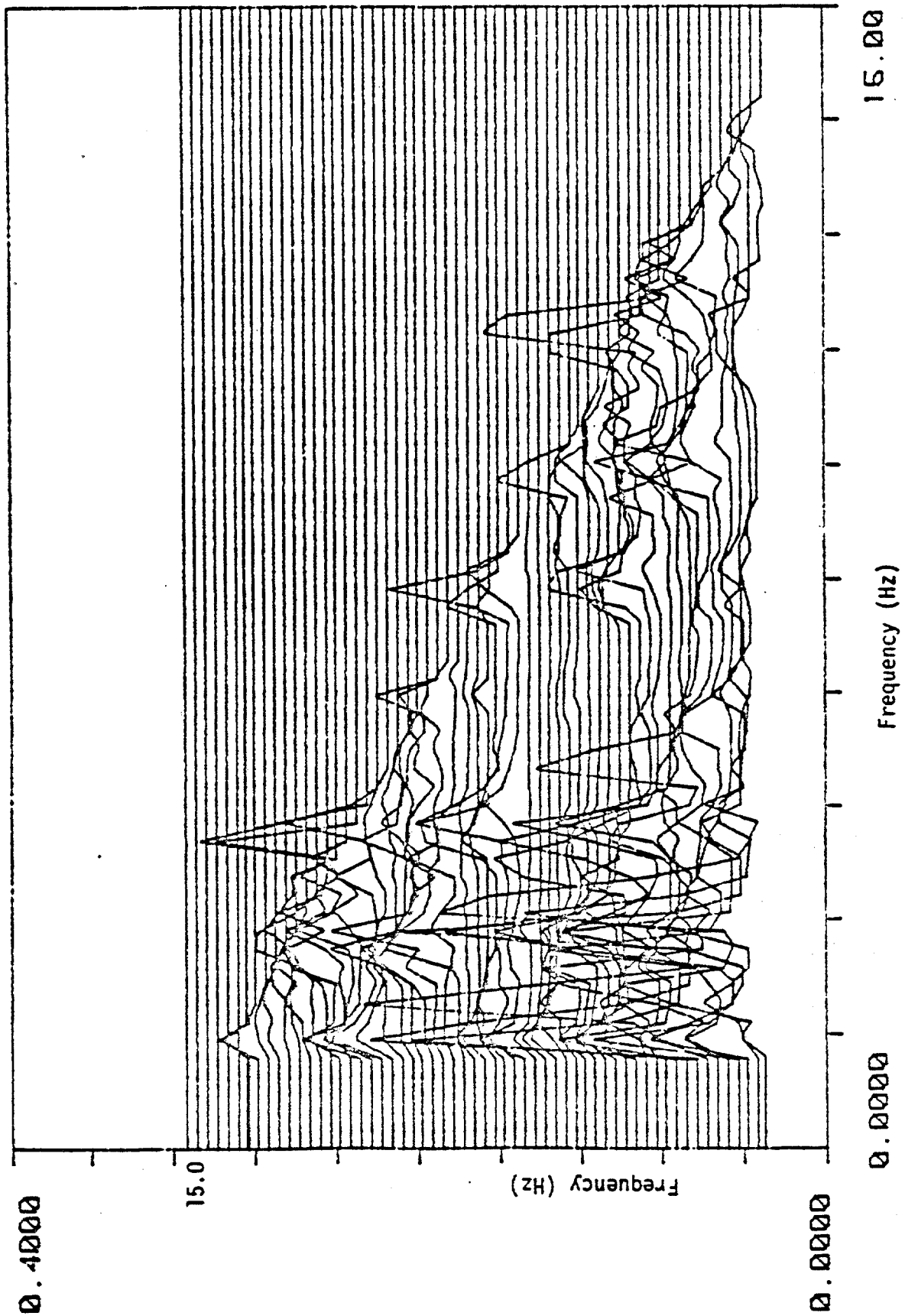
deduced from the Chi-square goodness-of-fit test of the response histogram. Figure 7-1 shows the auto-bicoherence spectrum for non-lock-in cross-flow response. This near-zero auto-bicoherence further proved the Gaussian assumption because the Cumulant average higher than second order is zero for a Gaussian process as discussed in section 5.1.

Figure 7-2 shows the magnitude of the quadratic transfer function  $G(W_1, W_2)$  at non-lock-in based on equation (7.1.11) with the input cross-flow response a Gaussian process as discussed in section 3.6. The spectra of in-line and cross-flow responses are shown in figure 5-11 and 5-12. Note that in this figure of  $G(W_1, W_2)$ , all the peaks tend to be concentrated along the 45 degree lines in the bi-frequency plane. While  $G(W_1, W_2)$  is the two-dimensional Fourier transform of the second order impulse response kernel  $g(u, v)$ , for a general quadratic system, it should not possess this particular property. This observation implies that there is some certain property in this quadratic system which might enable us to further simplify the system in the non-lock-in case. A special quadratic system possessing this particular property of  $G(W_1, W_2)$  has been formulated to identify such a system transfer function by Bendat and Piersol and will be discussed in the next



7-1 Auto-Bicoherence of Cross-Flow Acceleration in Figure 5-13  
at Non-lock-in





7-2 Quadratic Transfer Function between Cross-Flow and In-Line Acceleration in Figures 5-13 and 5-12 at Non-lock-in

section.

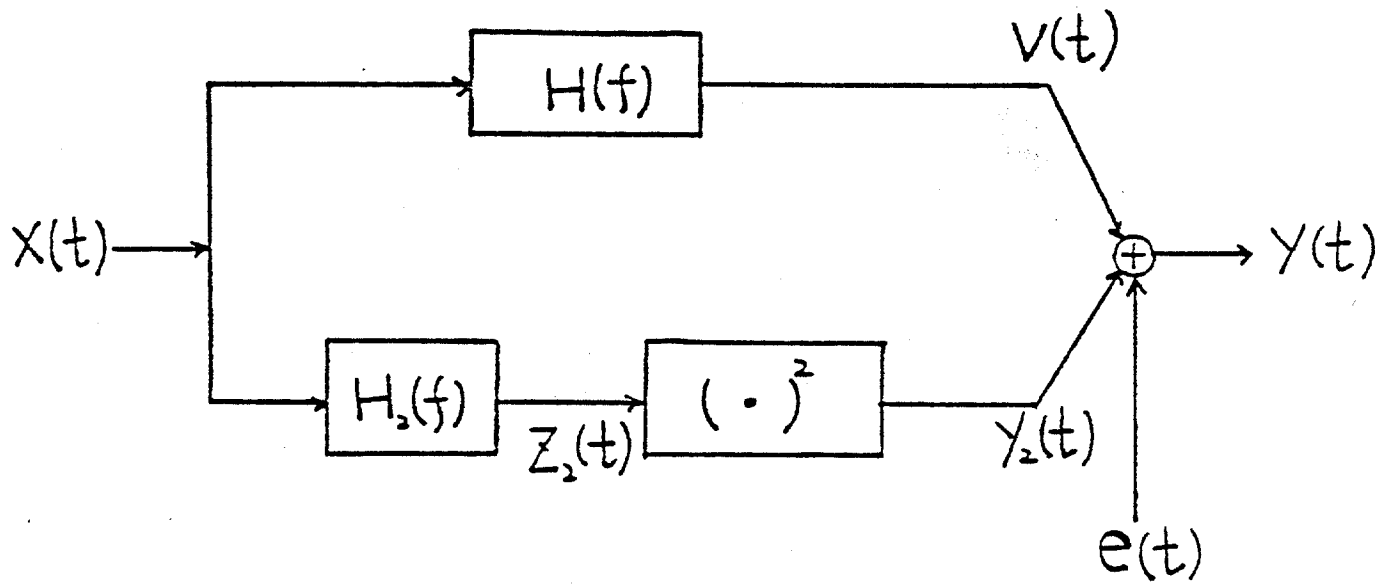
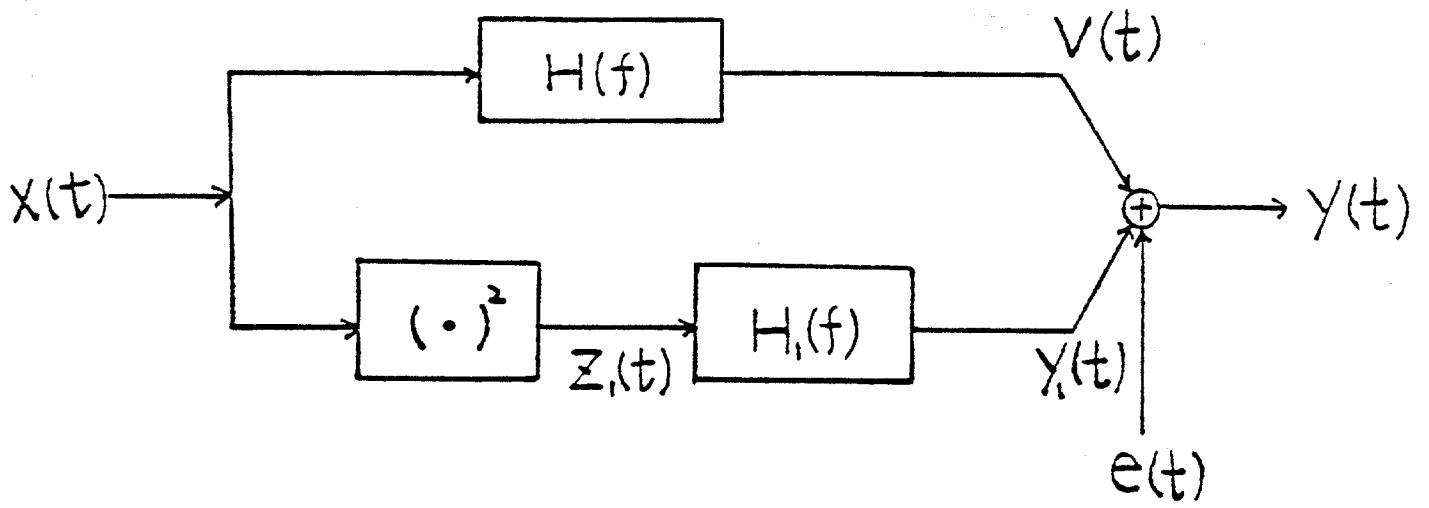
## 7.2 Quadratic System Involving Square-Law Operators

Two models of a quadratic system involving a zero memory square-law system as pictured in Figure 7-3, have been analyzed by Bendat and Piersol and are briefly discussed here. The zero memory square law system is either followed or preceded by a constant parameter linear system. These two models are called Case 1 and Case 2 and their properties were examined first in order to check if either of them can be used to simplify the quadratic system for the non-lock-in case.

The combination of the square-law system and linear system gives the relations between  $x(t)$  and  $y_1(t)$ ,  $y_2(t)$  for both cases as,

$$\begin{aligned}
 y_1(t) &= h_1(t) * [x(t)]^2 \\
 &= \int h_1(u) [x(t-u)]^2 du \\
 &= \iint h_1(u) \delta(u-v) x(t-u) x(t-v) du dv \\
 &= \iint g_1(u, v) x(t-u) x(t-v) du dv
 \end{aligned}
 \tag{7.2.1}$$

$$\begin{aligned}
 y_2(t) &= [h_2(t) * x(t)]^2 \\
 &= \left[ \int h_2(u) x(t-u) du \right]^2 \\
 &= \iint h_2(u) h_2(v) x(t-u) x(t-v) du dv \\
 &= \iint g_2(u, v) x(t-u) x(t-v) du dv
 \end{aligned}
 \tag{7.2.2}$$



where \* denotes the linear convolution and  $\delta(u)$  is the delta function. The second order impulse response kernels for these two cases are

$$g_1(u, v) = h_1(u) \delta(u - v) \quad (7.2.3)$$

$$g_2(u, v) = h_2(u) h_2(v) \quad (7.2.4)$$

The Fourier transforms of these two equations give the quadratic transfer functions  $G_1(W_1, W_2)$  and  $G_2(W_1, W_2)$  as,

$$G_1(W_1, W_2) = H_1(W_1 + W_2) \quad (7.2.5)$$

$$G_2(W_1, W_2) = H_2(W_1) H_2(W_2) \quad (7.2.6)$$

The system function  $H_1(W)$  and  $H_2(W)$  can be obtained by writing equation (7.2.5) and (7.2.6) as

$$G_1(W/2, W/2) = H_1(W/2 + W/2) = H_1(W) \quad (7.2.7)$$

$$G_2(W, W) = H_2^2(W) \quad (7.2.8)$$

By using equation (7.1.11) of the least square quadratic system identification result with Gaussian input, finally we obtain

$$H_1(W) = G_1(W/2, W/2) = \frac{B_{xy1}(W/2, W/2)}{2S_{xx}^2(W/2)} = \frac{B_{xy1}(W/2)}{2S_{xx}^2(W/2)} \quad (7.2.9)$$

$$H_2(W) = \text{SQRT}[G_2(W, W)] = \left\{ \left[ \frac{B_{xy2}(W, W)}{2S_{xx}^2(W)} \right] \right\} = \left[ \frac{B_{xy2}(W)}{2S_{xx}^2(W)} \right] \quad (7.2.10)$$

In which  $B_{xy}(W)$  is the special bispectral density function defined by

$$B_{xy}(W) = B_{xxy}(W, W) = E[X(W)X(W)Y(2W)] \quad (7.2.11)$$

Equations (7.2.9) and (7.2.10) were derived from the least square error point of view and they are identical to the results formulated by Bendat.

The linear transfer function  $H(W)$  derived by Bendat is also identical to the results of section 7.1 which is

$$H(W) = S_{xy}(W) / S_{xx}(W) \quad (7.2.12)$$

Checking the properties of the quadratic transfer functions in equations (7.2.5) and (7.2.6) permits one to determine whether or not the Case 1 model or the Case 2 model is more appropriate to fit to the non-lock-in data. According to equation (7.2.5) for Case 1, any peak associated with the function  $H_1(W)$  will show up along a 45-degree line in the bi-frequency plane of  $G_1(W_1, W_2)$  which is similar to the result stated in section 7.1, while Case 2 does not possess this property. It is then proposed to try the Case 1 model on the non-lock-in responses data. The goodness of the Case 1 model can then be checked from the residual  $n(t)$ .

The data presented in section 7.1 for non-lock-in case were analyzed again by using the Case 1 model and the resulting system functions  $H(W)$  and  $H_1(W)$  according to equations (7.2.12) and (7.2.9) are shown in figure 7-4 and 7-5. From these identified system functions  $H(W)$  and  $H_1(W)$ , the spectrums of residual  $n(t)$ , the linear and quadratic responses  $v(t)$  and  $y_1(t)$ , as well as the simulated in-line response  $y_s(t)$  were obtained according to,

$$S_{vv}(W) = S_{xx}(W) |H(W)|^2 \quad (7.2.13)$$

$$S_{y_1y_1}(W) = S_{z_1z_1}(W) |H_1(W)|^2 \quad (7.2.14)$$

$$S_{sys}(W) = S_{vv}(W) + S_{y_1y_1}(W) \quad (7.2.15)$$

$$S_{nn}(W) = S_{yy}(W) - S_{sys}(W) \quad (7.2.16)$$

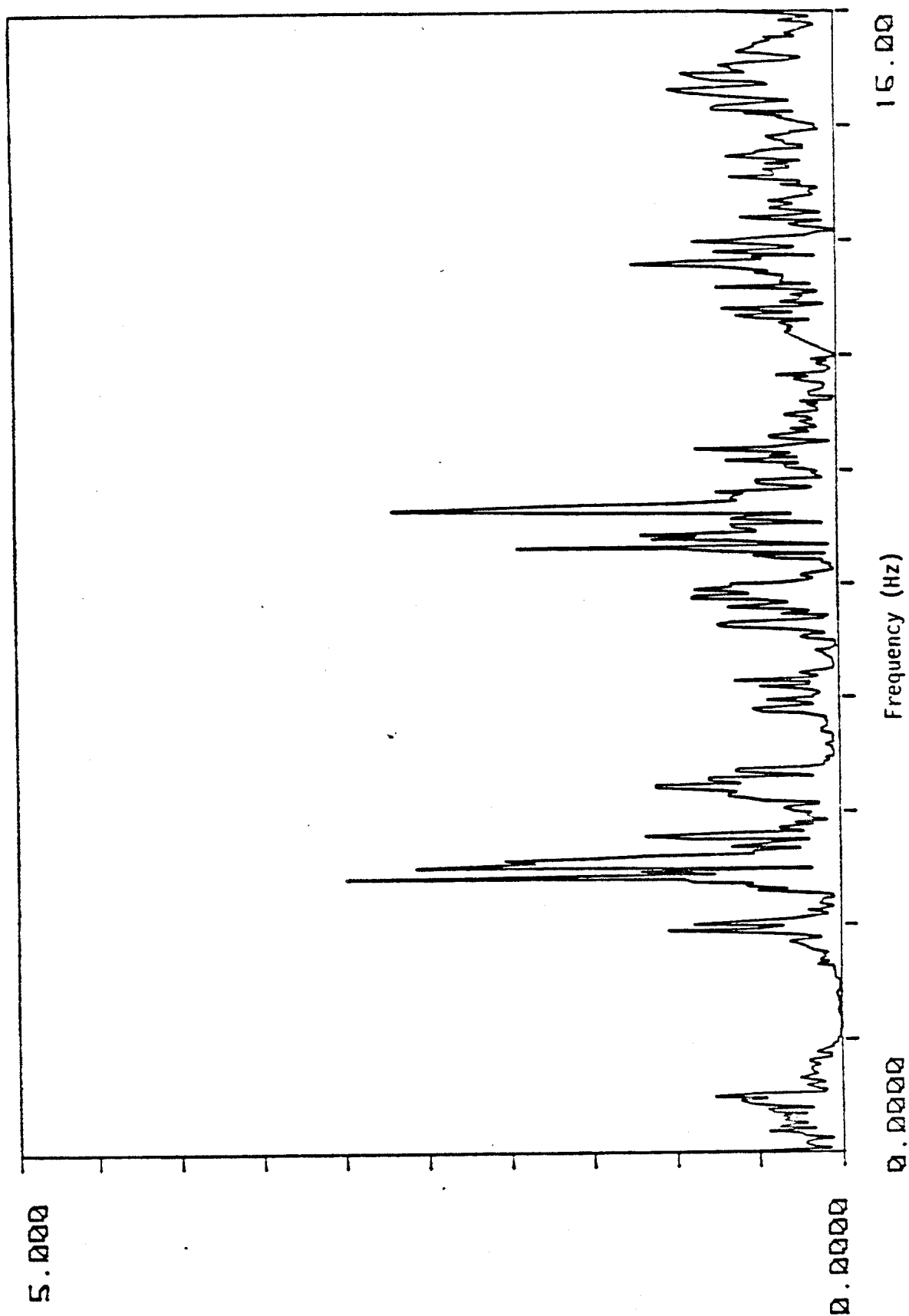
A small residual spectrum  $S_{nn}(W)$  compared to the in-line response spectrum was obtained as shown in Figure 7-6 which showed the goodness of fit of the Case 1 model to the data. This also meant that the existence of higher order nonlinearities was negligible in the relationship at the case. The spectrum of simulated in-line response  $S_{sys}(W)$  as shown in Figure 7-7 was in good agreement with in-line response spectrum  $S_{yy}(W)$  shown in Figure 5-11. The spectrum  $S_{sys}(W)$  is almost entirely contributed by the quadratic in-line response because the obtained linear in-line response spectrum  $S_{vv}(W)$  was very small and was not

shown here. This result is quite different from that of the lock-in case. It should be emphasized here that theoretically, the fractions of power associated with in-line response due to linear and quadratic correlations could be estimated by examining the linear and quadratic coherence spectrums [16] and [17]. However, due to the slight change of tidal current speed over the data recording period, the cylinder responses were not perfectly stationary which affected the accuracy of the cross-bicoherence spectrum estimations. As a result, the cross-bicoherence spectra provided only qualitative, rather than quantitative answers to the nonlinear problem in this research work.

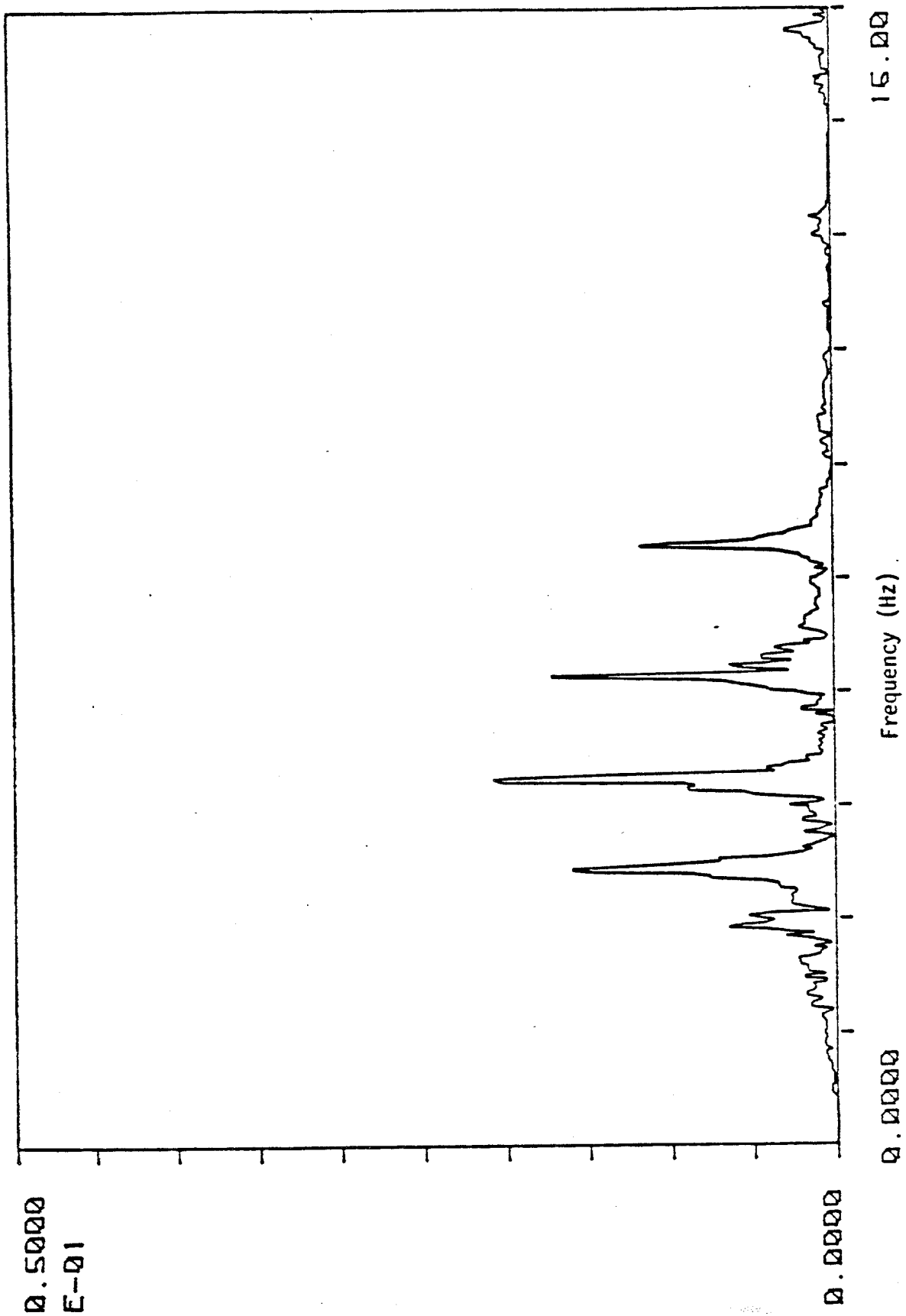
Finally, it is interesting to examine the characteristic of the square of cross-flow response, that is the output  $z_1(t)$  from the square-law system in the Case 1 model. Figure 7-8 shows the spectrum of  $z_1(t)$ ,  $S_{z_1 z_1}(W)$ , in which the two dominant peaks were located in the frequencies exactly equal to that of the in-line response spectrum  $S_{yy}(W)$  shown in Figure 5-11. Figure 7-9 is another example of the spectrum of the square of cross-flow response for the near-lock-in case. Comparing to figure 5-18, the two dominant peaks also located at the same frequencies. Figure 7-10 shows the linear coherence spectrum between  $z_1(t)$  and  $y(t)$  which demonstrated that these two fluctuating

quantities were highly linearly coherent as shown by the high peaks in the two dominant frequencies. Once more, this result provided the evidence of the existence of quadratic correlation between cross-flow and in-line responses.

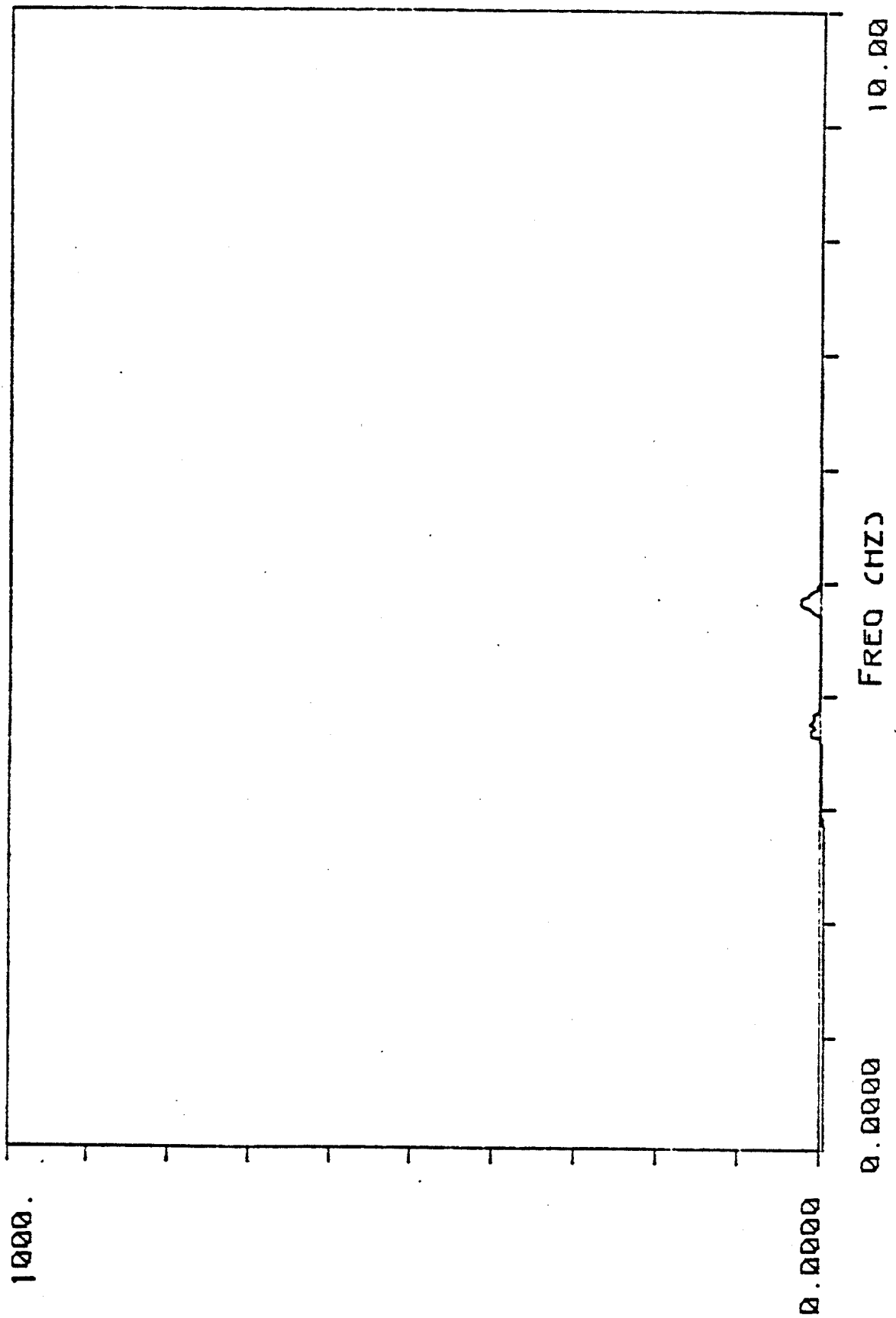




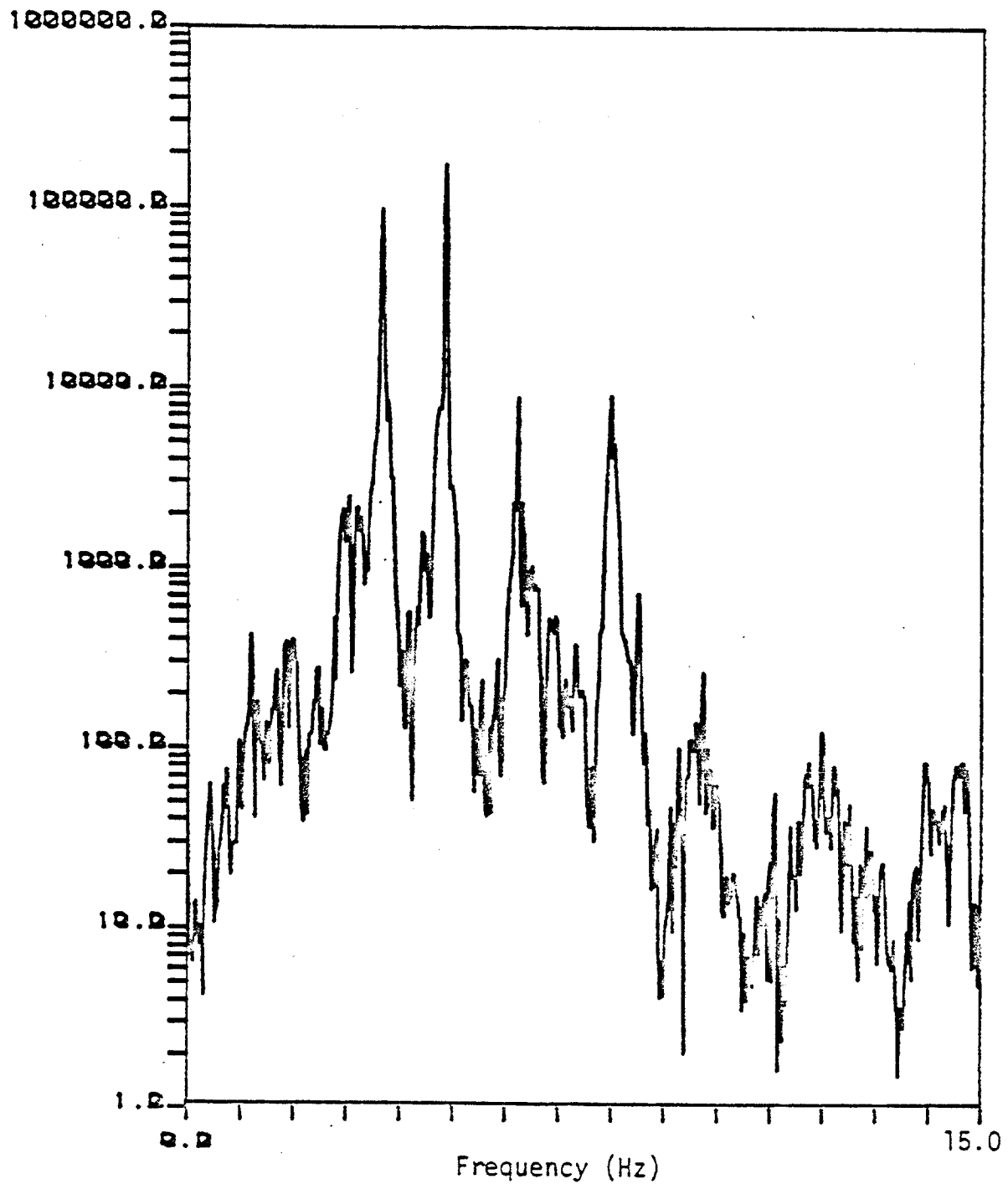
7-4 Linear Transfer Function HO(f) in Case 1 at Non-lock-in



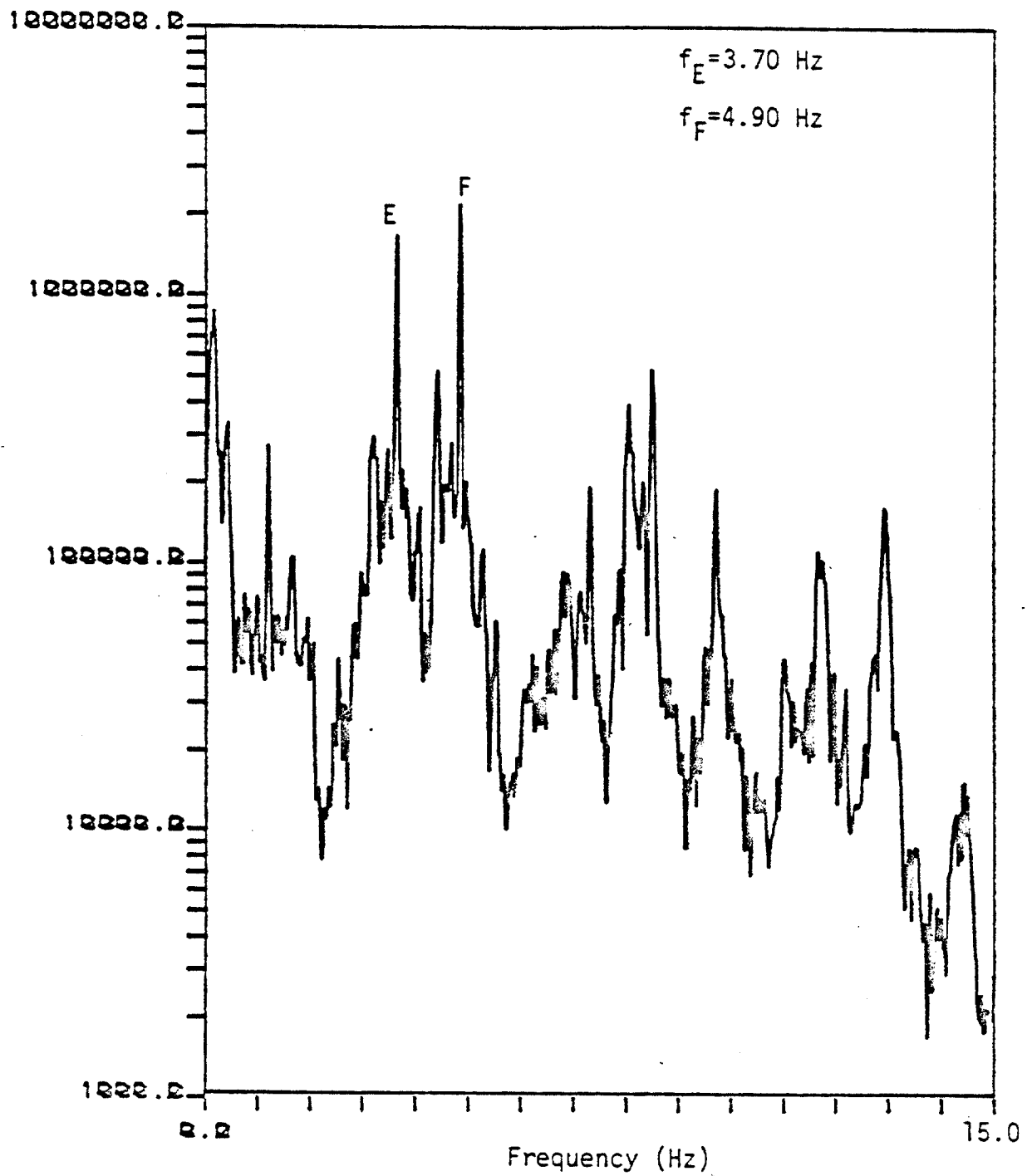
7-5 Linear Transfer Function  $H_1(f)$  in Case 1 at Non-lock-in



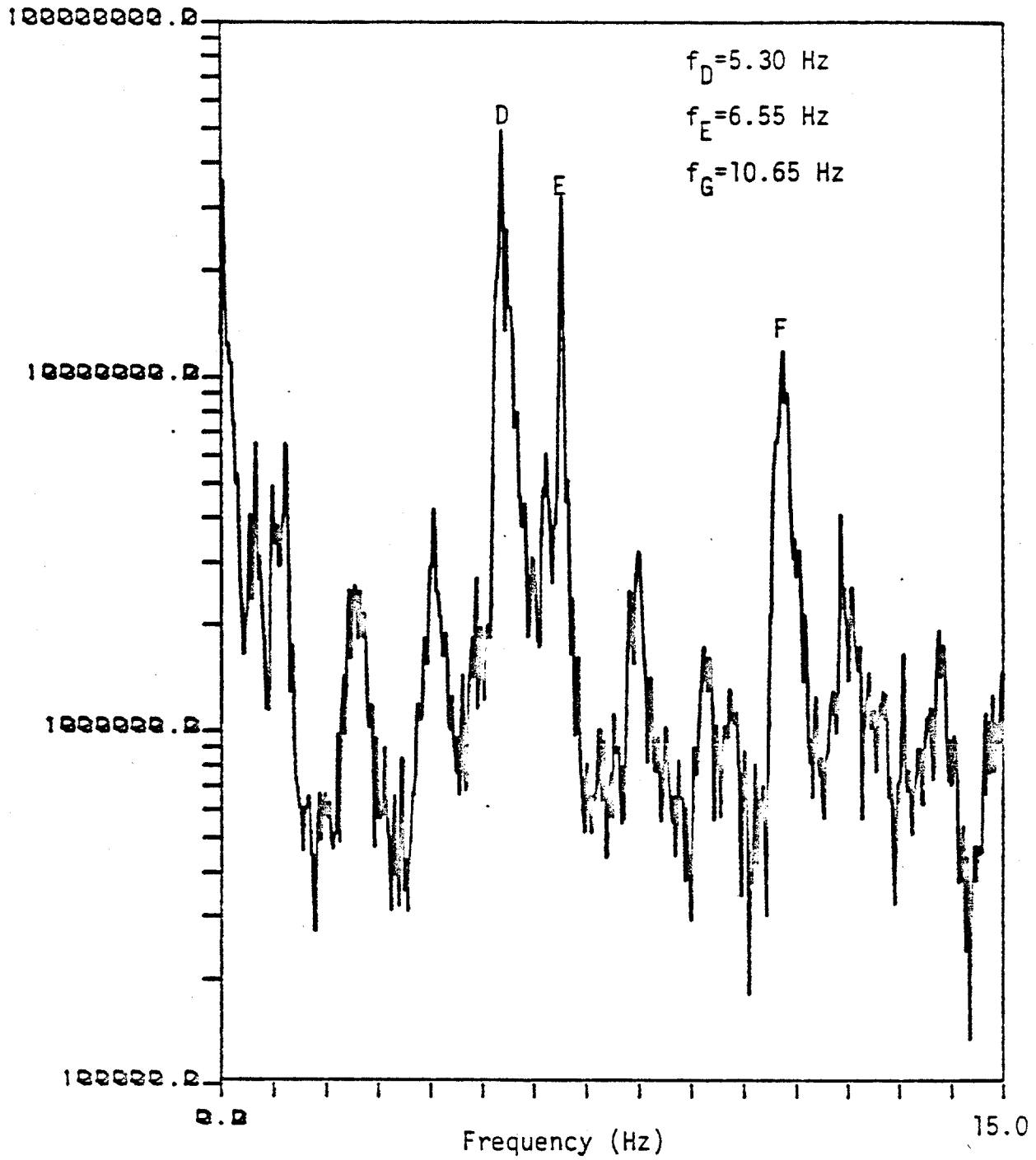
7-6 Power Spectrum of Residual



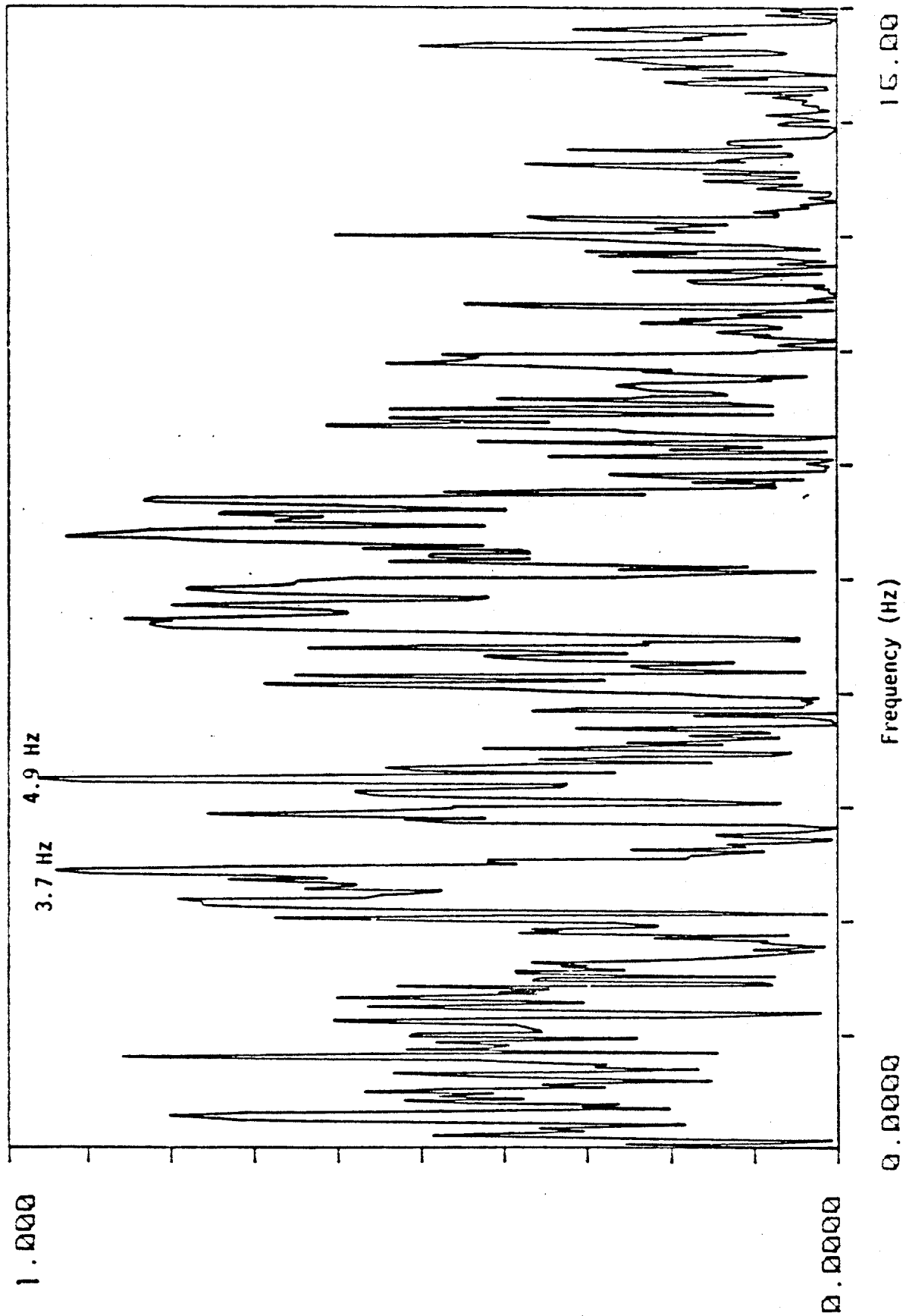
7-7 Simulated In-Line Acceleration Spectrum at Non-lock-in  
(Comparing to Figure 5-12)



7-8 Power Spectrum of the Square of Cross-Flow Acceleration at Non-lock-in (Comparing to Figure 5-12)



7-9 Power Spectrum of the Square of Cross-Flow Acceleration at Near-lock-in (Comparing to Figure 5-18)



7-10 Linear Cross-Coherence Between In-Line and Square of

Cross-Flow Acceleration in Figures 5-12 and 7-8 at Non-lock-in

## CHAPTER 8

### CONCLUSIONS

A field experiment has been conducted to investigate the vibration characteristics of both in-line and cross-flow responses of a long flexible cylinder subjected to vortex-induced excitation. Tests were successfully conducted under more realistic conditions than laboratory ones with cylinder length to diameter ratios of approximately 750 and Reynolds numbers up to 22000. Both lock-in and non-lock-in cases were analyzed with particular emphasis on the investigation of the relationship between in-line and cross-flow responses. For the first time convincing evidence was obtained on the existence of a quadratic relationship. Several time series analysis methods were carefully described including double integration, modal analysis, bispectral analysis and quadratic system identification. The results of this study suggest the following conclusions:

1. In-line and cross-flow responses are not independent for either lock-in or non-lock-in cases. From the modal analysis, the total vibration energies in these two directions were highly related to each other. Higher order spectral analysis was then performed in order to investigate the possibility of a nonlinear relationship.



The results of bispectral analysis indicated that responses in these two perpendicular directions were quadratically correlated to each other.

2. In-line response modes were not always excited at their natural frequencies. Instead, the response frequencies in the in-line direction were equal to double or the sum of that in the cross-flow direction. With the finding of the quadratic correlation, such frequency doubling and summing phenomena as well as the in-line non-natural response frequencies then could be explained.
3. Nonlinear correlations higher than second order were negligible in the nonlinear relationship for both lock-in and non-lock-in cases. A second order system was used to model this relationship with a residual or error term representing any imperfection (eg. noise or higher order nonlinearities) associated with this model. Very small residual terms were obtained from the quadratic system identification.
4. For the non-lock-in case, the in-line and cross-flow responses are linearly independent. This was shown by the linear coherence spectrum and by the decomposed linear contributing term in the modeled second order

system.

5. Wake oscillator models have been proposed by others to model the vibration in both in-line and cross-flow directions [9]. The conclusions from this thesis suggest that the wake oscillator models in the two directions should be coupled to each other by imposing the condition that in-line and cross-flow responses are correlated quadratically.

REFERENCES

1. Benaroya H. "Statistical Flow-Oscillator Modelling of Vortex-Shedding" Journal of Sound and Vibration 86(2), 1983
2. Bendat, J.S. and Piersol, A.G., "Spectral Analysis of Nonlinear Systems involving Square-Law Operators" Journal of Sound and Vibration 81(2), 1982
3. Bendat, J.S. and Piersol, A.G., Random Data: Analysis and Measurement Procedures, John Wiley and Sons, New York, 1971
4. Blevins, R.D., Formulas for Natural Frequency and Mode Shape, Van Nostrand Reinhold Company, New York, 1979
5. Blevins, R.D., Flow-Induced Vibration. Van Nostrand Reinhold Company New York, 1977
6. Brillinger D. R., Time Series. New York: Holt 1975
7. Brillinger D. R. and M. Rosenblatt, "Asymptotic Theory of Estimate of K-th Order Spectra," in Spectral Analysis of Series, B. Harris, Ed. New York: Wiley, 1967
8. Clough, Ray W. and Penzien, Joseph, Dynamics of Structure, McGraw-Hill, New York, 1975
9. Hartlen R.T. and Currie I.G. "Lift Oscillator Model of Vortex-Induced Vibration" Journal of the Engineering Mechanics Division, Proceedings of ASCE, Vol 96, EM5, 1970
10. Gray, A.H., and Markel J.D. "A Computer Program for Designing Digital Elliptic Filters", IEEE Trans. on Acoustics, Speech, and Signal Processing, December 1976
11. Griffin O.M. and Skop R.A., "The Vortex-Excited Resonant Vibrations of Circular Cylinders" Journal of Sound and Vibration (1973) 31(2)
12. Griffin O.M. and Ramberg S.E. "Some Recent Studies of Vortex Shedding With Application to Marine Tubulars and Risers" Journal of Energy Resources Technology, Vol. 104, March 1982

13. Iwan W.D. and Blevin R.D. "A Model for Vortex Induced Oscillation of Structures" Journal of Applied Mechanics, Vol. 41, September 1974
14. Jenkins G. M. and Watts D. G., Spectral Analysis and Its Application. San Francisco, CA: Holden-Day, 1968
15. Jong Jen-Yi and Vandiver J.K., "Response Analysis of the Flow-Induced Vibration of Flexible Cylinders Tested at Castine, Maine in July and August of 1981." MIT Ocean Engineering Department Report, 1983
16. Kim Y. C. and Power E. J. "Digital Bispectral Analysis and Its Application to Nonlinear Wave Interactions" IEEE Transactions on Plasma Science. Vol. PS7 NO.2, June 1979
17. Kim Y. C., Wang W. F., Powers E. J., and Roth J. R. "Extension of the Coherence Function to Quadratic Models" Proceedings of the IEEE, Vol. 67, No. 3, March 1979
18. King, R., "A Reveiw of Vortex Shedding Research and Its Application" Ocean Engineering, New England Section, Sept. 26, 1975.
19. McClellan, J.H., T.W. Parks and L.R. Rabiner (1973) "A Computer Program for Designing Optimum FIR Linear Phase Digital Filters" IEEE Transactions on Audio abd Electro-acoustics, Vol. AU-21, No. 6, December.
20. McGlothlin J.C. "Drag Coefficients of Long Flexible Cylinders Subject to Vortex Induced Oscillation", Thesis Presented to the Massachusetts Institute of Technology, Cambridge, Mass. 1981
21. Meirovitch, Leonard, Analytic Method in Vibrations, MacMillan Co., New York, 1967
22. Oppenheim, A.V. and Schafre R.R. Digital Signal Processing, Prentice-Hall, Inc., Englewood Cliffs, N.J. 1975
23. Rabiner, L.R. and Gold B. Theory and Application of Digital Signal Processing, Prentice-Hall, Inc. Englewood Cliffs, N.J. 1975
24. Sarpakaya, T., "Vortex Induced Oscillations. A Selective Review." ASME Journal of Applied Mechanics, Vol. 46, June 1979, pp. 241

25. Schuessler, H.W. and Ibler, W. "Digital Filters for Integration", European Conference on Circuit Theory and Design, Institute of Electrical Engineers, Conference Publication No. 116, 1974.
26. Skop, R.A., Griffin, O.M. and Ramberg, S.E., "Strumming Predictions for the SEACON II Experimental Mooring," Proc. Offshore Tech. Conf., Houston, TX, OTC 2884, 1977
27. Vandiver J.K. and Griffin O.M. "Measurement of the Vortex Excited Strumming Vibrations of Marine Cable", Proc. of Ocean Structural Dynamics, 1982
28. Vandiver J.K. "Natural Frequency, Mode Shape, and Damping Ratios for Cylinders Tested at Castine, Maine in the Summer of 1981", Unpublished M.I.T. Ocean Engineering Report.
29. Vandiver J.K. and Mazel, C.H., "A Field Study of Vortex-Excited Vibrations of Marine Cable", Offshore Tech. Conf., Houston, Texas, OTC 2491, 1976.
30. Vandiver J.K. "Drag Coefficients of Long Flexible Cylinders" Offshore Technology Conference., Houston, TX, OTC 4490, 1983

